Novel approach to filtering techniques in magnetic field measurements

Kasper Vestergaard Nielsen

Electronic Systems, ES-, August 8, 2024

AALBORG
UNIVERSITET

Electronic Systems
Fredrik Bajers Vej 7B
9220 Aalborg Øst

Title:

Novel approach to filtering techniques in magnetic field measurements.

Project:

Master Thesis

Project Period:

Febuary 2024 - August 2024

Author:

Kasper Vestergaard Nielsen

AAU supervisor:

Henrik Schiøler

CERN supervisor:

Carlo Petrone

CERN section leader:

Stephan Russenschuck

Pages: 103
Date of Completion: August 8, 2024

Abstract:

This report addresses the challenges in accurate solenoid measurements with filtering techniques in the framework of electron cooling. The overview of the general principles of electron cooling outlines the need for accurate flat magnetic fields. To measure the magnets a new design to the translating fluxmeter developed at CERN is presented and analysed.
The analysis finds that while the performance of the large fluxmeter coils is good, the smallest coils can tend to have a drift noise.
A customised filter for the specific fluxmeter is presented using a combination of Kalman and low-pass filtering. The proposed solution is tested on a simulation to estimate the filter performance and choose a filter design. To compare the filter performance against state-of-the-art solutions the filter is tested on a previously used dataset.
The specific project is addressed using the current measurement setup and an applied filter to increase the performance of the smallest fluxmeter coils.
The experiments show that while the application of a filter is possible and can improve some signals, the relation between measurements needs to be well defined before it makes sense to use Kalman filtering on different coils on the same fluxmeter. The study finds that the development of better field models is needed to further increase the usability of Kalman filtering in fluxmeter measurements.

Preface

This report is written by Kasper Vestergaard, as a master thesis in a collaboration with CERN and the education program; Electronic Systems engineering at Aalborg University (AAU). The project is written during the period Febuary to August 2024.

This report is addressed to the academic reader within technical science and electronic engineering. It is expected that the reader has an understanding of linear algebra, calculus, statistics and electromagnetic theory.

The report encompasses the activities alongside with results and theory from the work done as an associate member of staff in the technology - Magnets, Superconductors and Chryostats department at CERN. A big thanks to everyone in the TM section for help, support and guidance throughout the entire project period.

Reading guide:
All source quotations which appear in the main report, are numbered after appearance. The numbers refers to the source list. Figures, tables, listings and equations are numbered after the chapter and order. For example, equation 4.1, refers to the first equation in Chapter 4. Numbers in the text are written in text if less than 10. All numbers in figures and equations are written as symbols or numbers. All vectors are noted with an overhead arrow, $\vec{a}$. All newly introduced variables are written beneath the first equation in which they are introduced and keep their symbolic value throughout the report unless reintroduced with a new value.

Author:

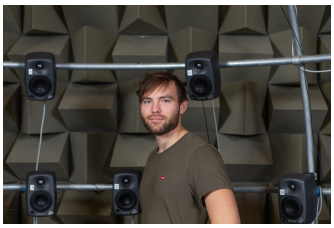

Kasper Vestergaard Nielsen
kvni19@student.aau.dk
kasper.vestergaard.nielsen@cern.ch

Table of Contents

Introduction 1

This project concerns the development and testing of a solenoid magnet measuring system. The general context of the project is the construction of a new electron cooler for the antiproton decelerator at CERN. This chapter contains a small introduction to the project as a whole and concerns CERN and the role of electron cooling in CERN's experimental setup.

1.1 CERN Introduction

CERN is an international organisation founded in 1954 after the second world war to keep European scientists engaged in European research. The general proposal was to build two different particle accelerators whereof the first was finished in 1957.[1] Throughout the years, CERN has become an epicenter for physics research in Europe and has expanded the complex of advanced machines with a considerable amount. At CERN, scientists and engineers from around the world collaborate on a multitude of experiments. These experiments range from studying the properties of known particles to searching for new particles that could provide insights into the nature of dark matter or explain the imbalance between matter and antimatter in the universe. The data generated by these experiments is vast and complex, requiring sophisticated analysis techniques and a powerful computing infrastructure. The different experiments often rely on very precise and high-performance magnets that has great influence on the results of the physics research in general.
The increasingly complex measurements of these magnets are in general entrusted to the TE-MSC-TM section at CERN. Research is made on a daily basis to be able to monitor the effects of the advanced magnets and accommodate new requirements.

1.2 TE-MSC-TM

The TE-MSC-TM section oversees the development of techniques to measure the magnetic fields and effects in the various projects.
In this project, a solenoid magnet and a total assembly must be corrected with very high precision to accommodate the requirements of the antiproton decelerator electron cooler. The general deadline for installing the electron cooler is for a three-year long shutdown starting in 2026. The measurement campaign is set to be initiated in 2025, lasting almost a full year.
Many critical issues in this measurement campaign need to be solved for the project to progress and succeed. Many of these challenges will be addressed in subsequent chapters. Some of the challenges arise from the magnet types itself and some from the electron cooling process.

The general role of electron cooling is to reduce unwanted momentum in particle beams. The importance of the process is briefly described in the next section.

1.3 Antiproton decelerator and cooling

The antiproton decelerator is a device at CERN that is used to decelerate antiprotons in the CERN accelerator complex.
The antiprotons are created by colliding the accelerated particles from the proton synchrotron accelerator ring with an iridium target. The produced antiprotons exit the target with too much energy to conduct experiments on many of the properties of interest. The high momentum creates the need for the particles to cool.
The cooling is done in two steps known as stochastic cooling and electron cooling. [2], [3]
From the collision at the iridium target, antiprotons are collected at an energy level of 3.5 GeV. Stochastic cooling is used in two sequences at 3.5 GeV and 2.0 GeV, whereafter electron cooling is used to achieve the energy levels 0.3 GeV and 0.1 GeV.[2]
One performance measure of electron cooling is the cooling time at certain energy levels till the energy levels of the antiprotons and electrons equalise.
The current electron cooler in the antimatter factory had major breakdowns in 2018. It is currently set to be replaced which also creates an opportunity to upgrade the cooler performance and get closer to the specifications desired for the antiproton decelerator when initially designed.[4] Appendix A shows an overview of the specifications. These specifications were expected to be met at construction when the cooler from the LEAR ring was repurposed, but the cooling time did not meet the requirements.
The following project concerns the magnetic measurements of the drift solenoid. The performance of that particular magnet is crucial when designing the new electron cooler for the antiproton decelerator.
The project will introduce the desired results through a description of the electron cooling setup and propose different approaches to hopefully improve the electron cooling effect improving measurement quality of the magnetic field.

Project description 2

This chapter describes the project framework by adding brief background knowledge of electron cooling and the requirements needed to be met.

2.1 Electron coolers

The process of electron cooling is a way to reduce particle beam unwanted longitudinal and transversal momentum using a foil of electrons guided around the beam. The process of electron cooling works best at low energies which is why the cooler in the Antiproton decelerator is used for the lowest energy levels in the cycle.[3]
The process of electron cooling is done with the electron cooler setup that is used in multiple experiments at CERN and other particle accelerators around the world.[5]
The electrons are boiled off of a cathode and guided from the cathode to the beam path where the transverse energy will be converted to a rotation around the beam path in what is referred to as the good-field-region of the drift solenoid. As illustrated simply in Figure 2.1 the general goal is to make the electrons as cold as possible in relation to the antiprotons so the electrons can absorb the longitudinal and transverse energy. The region in the drift solenoid where the path of the antiproton or ion beam intersects with the path of the electron foil is defined as the good-field-region. The good-field-region needs to follow along the beam path as precisely as possible to convert the electrons' transversal motion to circular motion around the beam path.

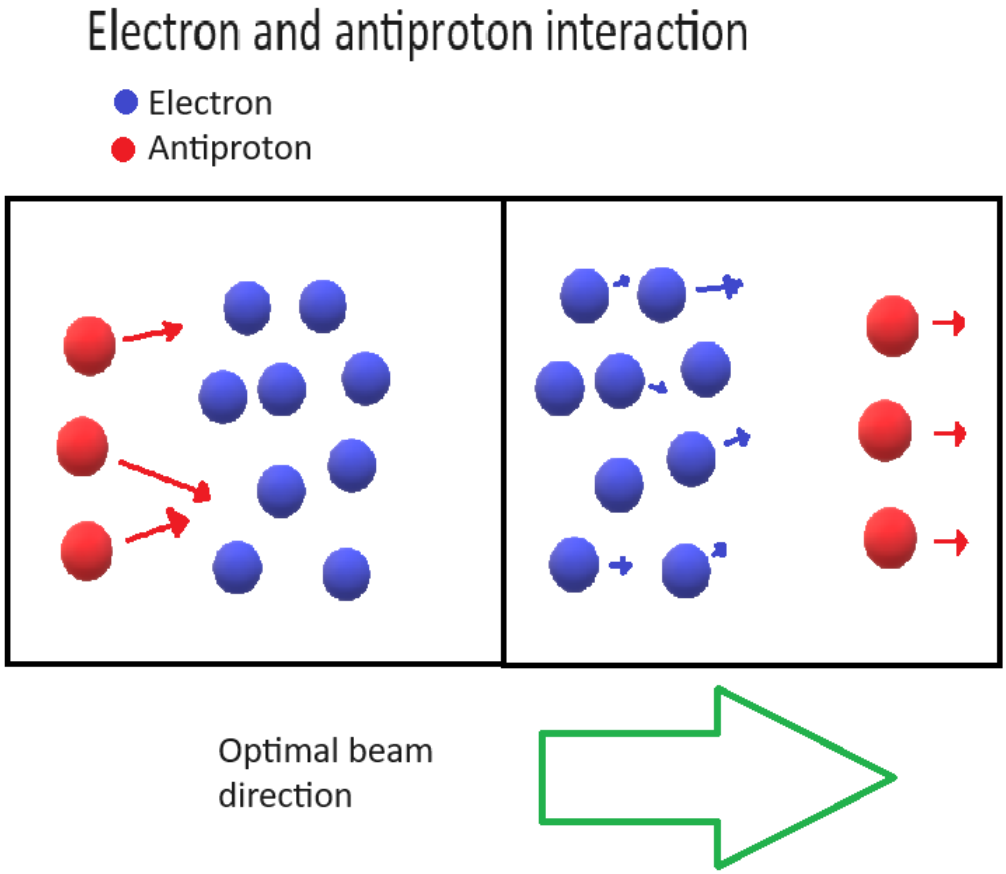

Figure 2.1. An illustration of antiprotons and electrons on the same beam line where the antiprotons move relative to the electrons with a longitudinal and transversal momentum which is reduced upon passing through the electron foil.

The different elements in an electron cooler can be seen in Figure 2.2 where the layout of a general assembly is illustrated. The functional task of the different components seen in Figure 2.2 will be outlined and described shortly. The specifications regarding the particular electron cooler in the antiproton decelerator can be seen in Appendix A.

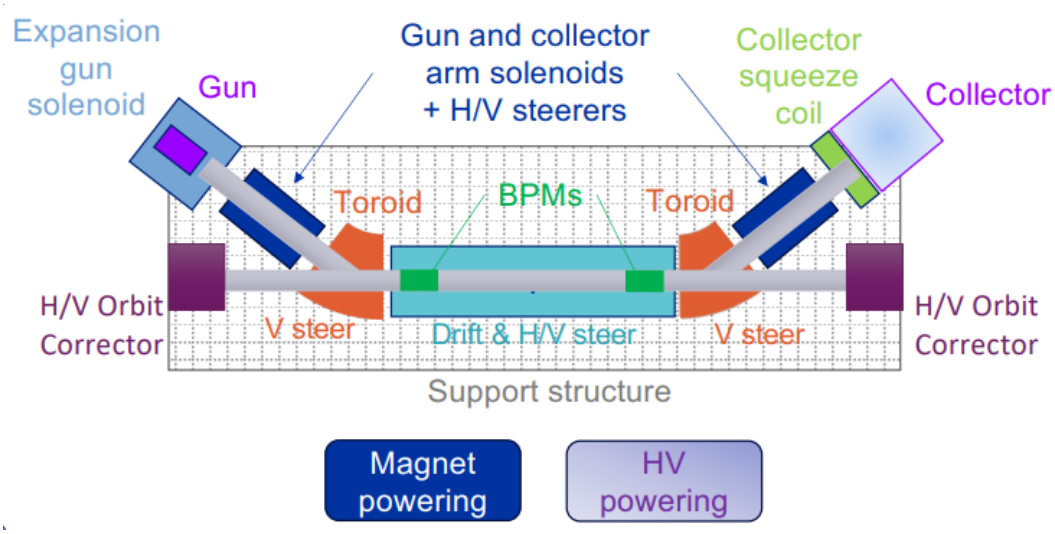

Figure 2.2. The electron cooler setup with the different necessary components for cooling the antiproton beam.[6]

Gun

The electron gun is the cathode of which the electrons are boiled. The temperature of the cathode is of interest to the electron cooling designers since a hotter cathode will result in hotter electrons. The colder the electrons are at emission the better the cooling effect. The temperature is important since a drop in electron temperature will result in a more effective absorption of energy at the intersection with the antiproton beam line.

Expansion gun solenoid

The general function of the expansion gun solenoid is to create a strong solenoid field that squeeze the path of the electron until it reaches the arm solenoid. When the electrons reach the arm solenoid the path of the electron expands which cools the electron an amount proportional to the change in field strength.

Arm solenoids

The general task of the arm solenoids is to keep the electrons confined around a desired beam path and guide it to and from the Toroid magnets on both sides of the drift solenoid.

Toroid magnets and orbit correctors

The task of the toroid magnets is to guide the electron beam along the antiproton beam path at first while the opposite toroid magnet guides the electrons away. The toroid magnets exert a dipole field at their local aperture which will also to some degree misalign the antiproton beam. To keep the beam in the correct orbit the orbit corrector magnet preemptively changes the path of the antiprotons before entering and after exiting the drift solenoid.

Drift solenoid

The drift solenoid is the solenoid that confines the electrons around the antiproton beam path. The drift solenoid field flatness is of great importance for the performance of the electron cooler. The importance of the flatness arise from the ability to bind the electrons along the beam path due to the Lorenz force[7].

Collector and collector squeeze coil

The collector and the collector squeeze coil are a system that squeezes the electron beam and dump the electrons.

Figure 2.2 shows an electron cooler setup where the cathode is in the electron gun and the toroid magnets pull the path of the particles into a circular arc with a dipole field. An illustration of an arc-like electron path combined with the optimal path in the drift solenoid can be seen in Figure 2.3 where the red path symbolises the solenoid and dipole field created by the drift solenoid and the toroid magnets.

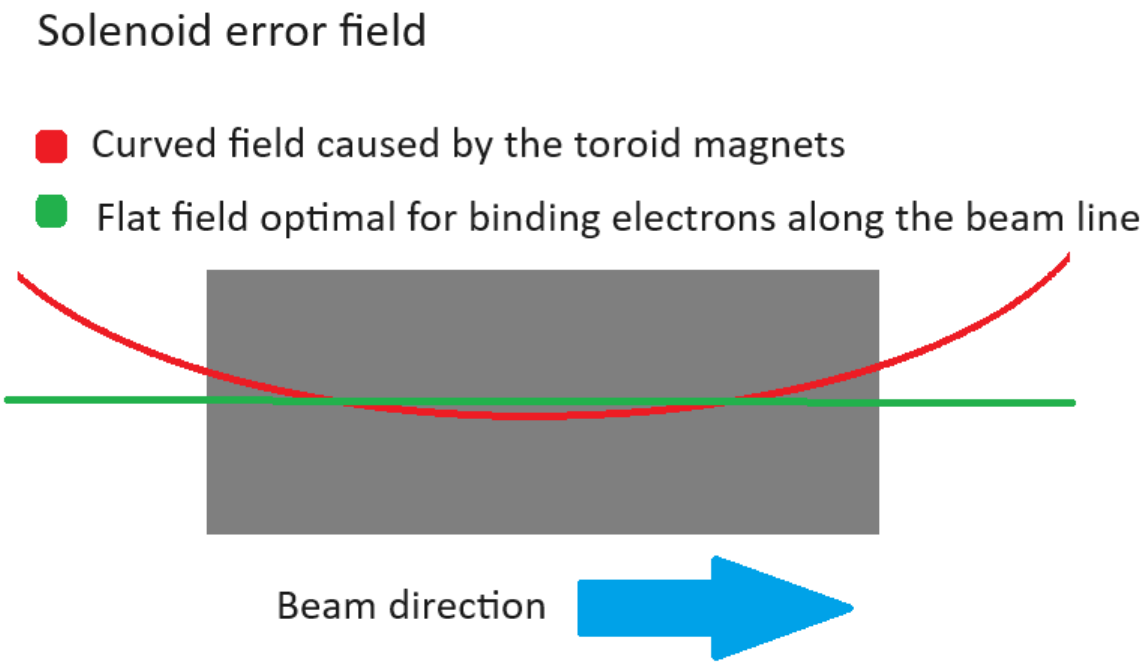

Figure 2.3. The uncorrected field line of the drift solenoid (red line) in the electron cooler setup next to the optimal line for the cooling process (green). The curve of the red line is introduced from the outside magnets seen in figure 2.2

The flat solenoid field will make the electrons rotate around the beam path due to the Lorenz force applied by the solenoid field. One of the main parameters affecting the performance of the electron cooler is the flatness of the field in the specific good-field region where the beam and electron path intersect. Another performance deciding parameter is the temperature of the

cathode that decides the initial momentum of the electrons. The temperature is not affected by the magnets which means that the temperature of the cathode and the error in the good-field region of the magnet can be seen as two independent sources of error. In this report, the focus will be to obtain the best possible field flatness in the drift solenoid.
The solenoid field in general, the correction scheme of the field and the parameters for which the antiproton decelerator electron cooler is designed to reach is explained in the sections 2.2, 2.3, and 2.4.

2.2 Solenoid magnetic fields

The solenoid magnetic field is the field occurring through the bore of a wound coil. The field is usually expressed using three different terms, namely B_z, B_r, and B_φ which are described as the field lines or changes in the field along the three different axis in cylindrical coordinates. A simplified illustration of these coordinates can be seen in Figure 2.4 where the arrows represent field components.
The blue arrow represents the change in the field along the z-axis, the green arrow represents a change in the field as a result of moving away in any direction perpendicular to the z-axis, and the red arrow represent the change in field as a result of a rotation around the z-axis at a fixed distance.

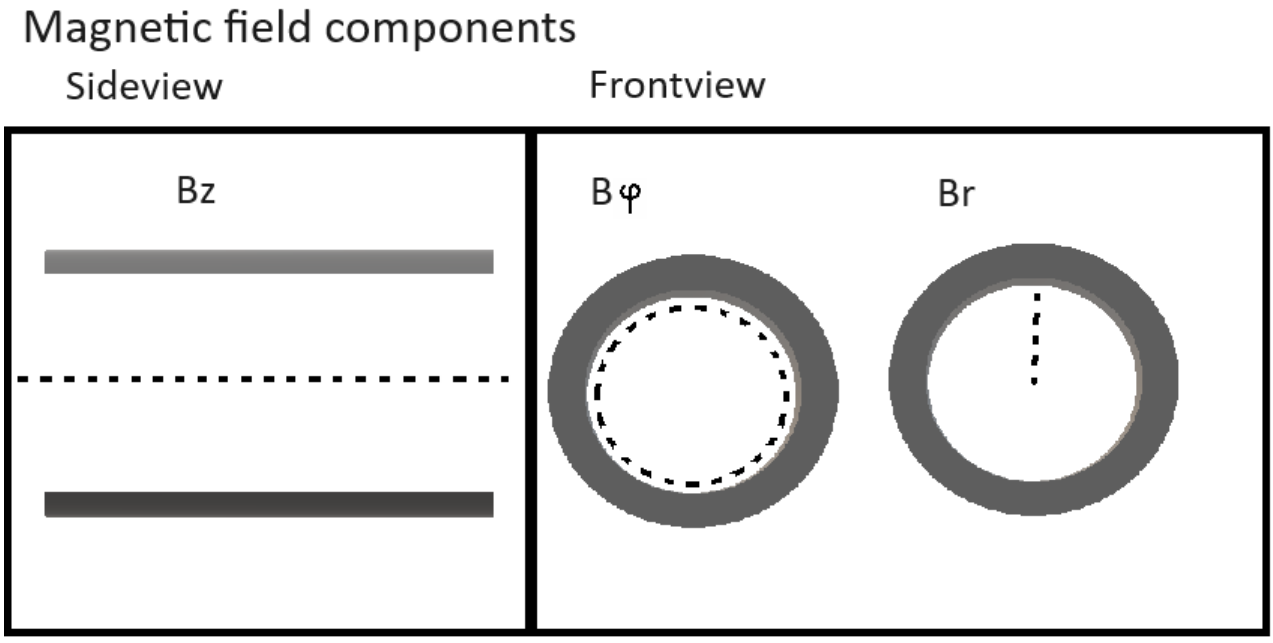

Figure 2.4. An illustration of the field components in a solenoid magnet. Each dashed line is along the direction of which the gradient of the scalar potential of the field is the B field component.

The general shape of a field can be seen in the Figure 2.5 generated in a simulation software.

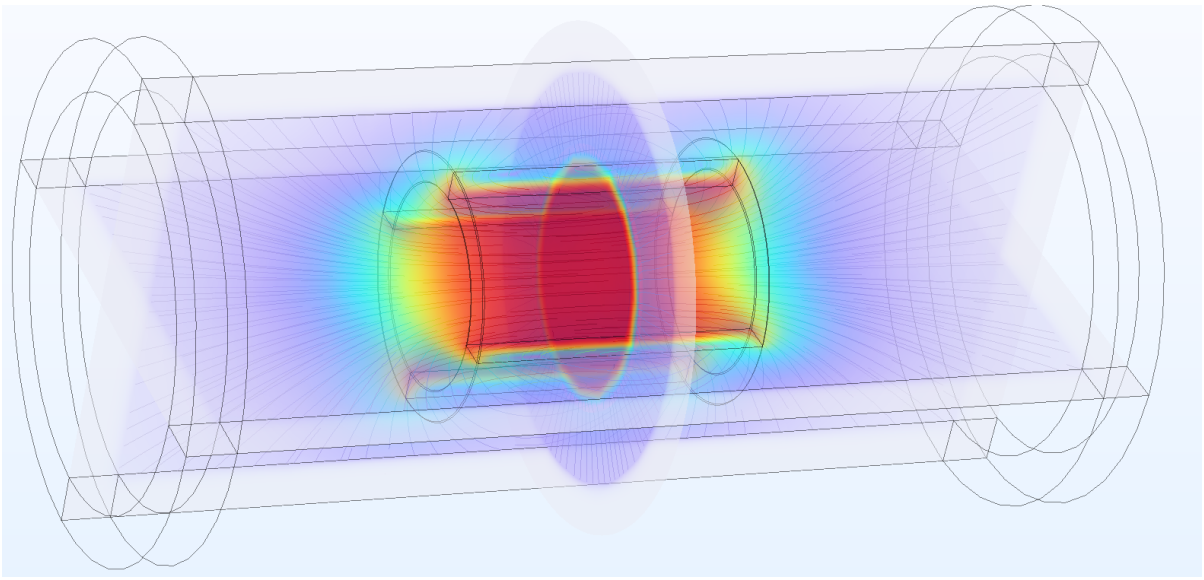

Figure 2.5. The general solenoid field profile generated from an arbitrary wound coil expressed in the COMSOL-Multiphysics simulations software[8]. The blue lines are magnetic lines. The colors indicate the relative strength of the field.

The solenoid field in Figure 2.5 is generated using the simulation tool Comsol. All field lines inside the aperture at the center of the magnet is parallel to the z-axis in the center of the magnet which is the general case with solenoid magnets. The field quality is very purely aligned along the longitudinal axis z in the center of the magnet.
This also imposes that if a solenoid could be infinitely long the solenoid field would be completely pure. However, the infinite case is a theoretical abstraction and not feasible in real-world applications which give rise to other field components than the parallel field B_z Another thing to notice in Figure 2.5, which is very much finite, is that the field in the radial direction increase at the ends of the solenoid. If the figure is rotated around itself it adds the third dimension of the cylindrical coordinates. The third coordinate B_φ is an angle on which the radial coordinate is rotated from a baseline perpendicular to the z-axis. The amount of field line tangents in the direction of the B_φ coordinate tangent is usually assumed negligible or zero which is symmetric propagation of the B_r field around the z-axis. Generally, these assumptions only hold to some accepted degree of error since no field in reality is perfect.

2.3 Solenoid correction scheme

The drift solenoid correction scheme has the objective of correcting the unwanted dipole field effects induced by the toroid magnets in the drift solenoid implied in Figure 2.3.
The correction is mostly needed in the end regions of the magnet where the additional dipole field from the toroid magnets bends the flat solenoid field line to an arc. To decrease the amount of unwanted dipole field the field errors will be counteracted with a dipole field generated by a saddle coil created to fit the particular magnet. The design of the drift solenoid can be seen in Figure 2.7 where the saddle coils are wrapped around the solenoid in opposite pairs that can create a dipole field between them as seen in Figure 2.6.

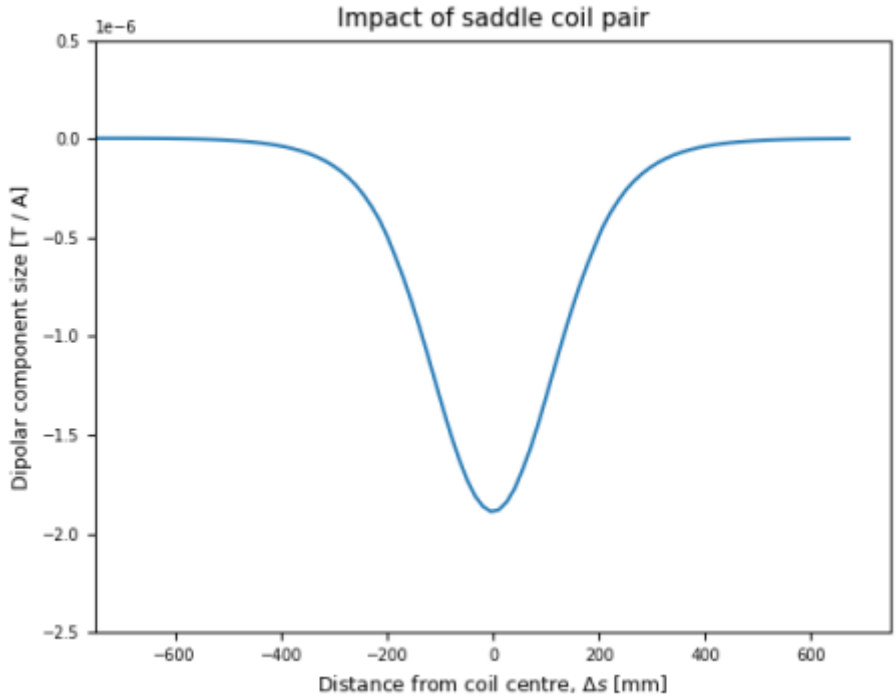

Figure 2.6. the expected magnetic transfer function of the saddle coil. Sourced from CERN, TE-TM-AD section.

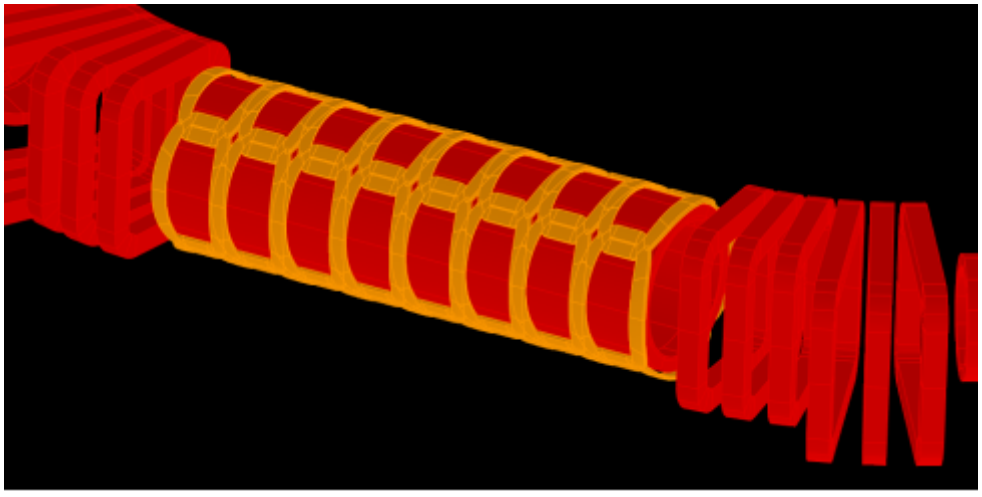

Figure 2.7. The saddle coils placed along the drift solenoid. Sourced from CERN, TE-TM-AD section.

The idea is to utilise the ability to push the center of the magnetic field in a flat shape that makes the electrons follow a desired motion along their direction of motion through the solenoid. The correction scheme assumes a linear relation between the dipole coils which means that the correction of the field can be applied as a solution to a linear algebra equation.

$$\begin{bmatrix} B_1^e \\ B_2^e \\ \vdots \\ B_n^e \end{bmatrix} + \begin{bmatrix} B_{11}^t & B_{12}^t & \cdots & B_{1n}^t \\ B_{21}^t & B_{22}^t & \cdots & B_{2n}^t \\ \vdots & \vdots & \ddots & \vdots \\ B_{n1}^t & B_{n2}^t & \cdots & B_{nn}^t \end{bmatrix} \cdot \begin{bmatrix} B_1^c \\ B_2^c \\ \vdots \\ B_n^c \end{bmatrix} = \begin{bmatrix} B_1 \\ B_2 \\ \vdots \\ B_n \end{bmatrix} \tag{2.1}$$

B^e	The current field along the magnet with a dipole component skewing the solenoid field.
B^t	The transfer function of B^c to B^e.
B^c	The correction dipole field from the external saddle coils.
B	The resulting magnetic field.

The challenge is to find the vector B^c that minimises the amount of field error in the good-field region of the drift solenoid. To measure this, especially in a setup with multiple magnets, proves to be very difficult.

2.4 Solenoid measurement requirements

To obtain the vector of currents applied to the saddle coils that minimises the field error some specific knowledge about the magnet is needed.
The general transfer function between field and current for each set of corrector coils needs to be known to some extent to apply the correct magnitude of correction on each coil.
Another important knowledge is the radial field strength and the center of the radial field throughout the magnet.
The precision of the measurement needs to be to a degree that ensures that the field error will not dominate the combined error of the temperature of the cathode and the field error.
Alongside the challenge of obtaining an error small enough to be in the desired range, another theoretical challenge is to separate the solenoid and the dipole field since the correction should compensate primarily the externally added dipole.
The summarised requirements of the measurement project can be set up as:

- Make a field map of the magnet and fiducialise the magnetic axis.
- Isolate a description of the dipole components of the magnetic field.
- Know the magnetic moment from a correction coil to find the optimal vector of inputs for the corrections scheme.

This project will investigate different measurement techniques to obtain the desired knowledge of the field using a newly developed sensor for normal conductive solenoid magnets.
Due to the novelty of the sensor the general performance measure and how to obtain the best possible field measurements are of interest. Therefore, the primary problem analysed throughout this project will be an attempt of optimising the measurement quality with a fluxmeter as the primary instrument. The next chapter investigates possible ways of measuring the magnet and introduces the translating fluxmeter which is the sensor to be used in the measurement campaign.

Solenoid magnetic measurement 3

This chapter will address the magnetic measurement of the solenoid magnet. In the chapter a description of how to represent a solenoid field, a presentation of a novel proposed fluxmeter and an analysis of the measurement noise and quality is described. A solenoid magnet can be represented in multiple ways. One possible solution is to create an elaborate description of the field in the entire aperture of the magnet.
A meaningful general way to describe the field inside the aperture is to obtain an infinite series that is a solution to the Laplacian with some predefined boundary conditions. Using this approach might enable the extraction of more information about the magnet.
To be able to relate the data of a measurement to the information needed it is important to understand how the sensor interacts with the field. The general sensor used for solenoid measurements will be a translating fluxmeter designed for the specific purpose of measuring solenoid magnets.
Another important understanding is that of the measurement technique and the noise which can affect both the measurement of the solenoid alone and the full system.
The next sections will introduce the sensor used to approach the requirement of the electron cooler project and the analytical approach used to gain the relevant information.

3.1 Field modelling

The multipole in general relates to electrostatic problems where there are no time varying fields affecting the magnetic field in which Maxwells equations simplify to Gauss law and a Ampère's law, meaning that the solution to the differential equation $\vec{\nabla} \cdot (\vec{\nabla} \mathrm{f}) = 0$ holds the solution to how the field propagates through a domain free of currents.[9]
A description of this propagation through the domain can be related to the separate field components which can be used to track the field through the solenoid and thereby give an indication of how to correct the errors.

3.1.1 Cylindrical coordinates

The cylindrical nature of a solenoid magnet makes it suitable to use the cylindrical coordinates to describe the field. The mapping from $\mathbb{R}^3$ to $\mathbb{R}^3$ of the cylindrical coordinates denoted r, φ, and z to the cartesian coordinates x, y, and z.

$$\mathrm{x} = \mathrm{r} \cdot \cos(\varphi) \tag{3.1}$$

$$y = r \cdot \sin(\varphi) \tag{3.2}$$

$$z = z \tag{3.3}$$

z is the longitudinal displacement from the origin through the cylindrical aperture while the other two coordinates are polar coordinates used to place the coordinate in the plane perpendicular to z.
The Laplacian in cylindrical coordinates are often used in magnetostatics to describe the propagation of fields in current free regions. The Laplacian in cylindrical coordinates used for defining the boundary value problem $\vec{\nabla} \cdot (\vec{\nabla} f) = 0$ can be seen in Equation 3.4.

$$\vec{\nabla} \cdot (\vec{\nabla} \Psi) = \frac{1}{r} \frac{\partial}{\partial r} \left(r \frac{\partial \Psi}{\partial r} \right) + \frac{1}{r^2} \frac{\partial^2 \Psi}{\partial \varphi^2} + \frac{\partial^2 \Psi}{\partial z^2} \tag{3.4}$$

solving for the field inside the solenoid setting Equation 3.4 to zero.

$$\frac{1}{r} \frac{\partial}{\partial r} \left(r \frac{\partial \Psi}{\partial r} \right) + \frac{1}{r^2} \frac{\partial^2 \Psi}{\partial \varphi^2} + \frac{\partial^2 \Psi}{\partial z^2} = 0 \tag{3.5}$$

Ψ	The magnetic scalar potential in the cylindrical area.

In general, an assumption that can be made is that the azimuthal field is invariant, or at least negligible over a full rotation which means that the Laplacian can be expressed.

$$\frac{1}{r} \frac{\partial}{\partial r} \left(r \frac{\partial \Psi}{\partial r} \right) + \frac{\partial^2 \Psi}{\partial z^2} = 0 \tag{3.6}$$

The solution to the problem can be found assuming that coordinate-depending expressions for the field can be found using separation of variables. In a cylindrical magnetic field, the solution consists of the three terms R and Z so that there is a dependency on each variable coordinate.

$$\Psi(r, z) = R(r)Z(z) \tag{3.7}$$

R	Function describing the magnetic scalar potentials reliance on r.
Z	Function describing the magnetic scalar potentials reliance on z.

Enables solving the differential equation using separation of variables. expressing Equation 3.6 in the terms of R(r) and Z(z) results in.

$$\frac{1}{R} \left(\frac{1}{r} \frac{\partial}{\partial r} \left(r \frac{\partial R}{\partial r} \right) \right) + \frac{1}{Z} \frac{\partial^2 Z}{\partial z^2} = 0 \tag{3.8}$$

Separating Equation 3.8 yields the two expressions.

$$r^2\frac{\partial^2 R}{\partial r^2} + r\frac{\partial R}{\partial r} + \lambda^2 rR = 0 \tag{3.9}$$

$$\frac{\partial^2 Z}{\partial z^2} - \lambda^2 Z = 0 \tag{3.10}$$

λ^2	Constant introduced when separating the expression.

Where the solution to Z and Φ can be expressed as Fourier series expansions and the solution to R is found with a Bessel series.

$$Z(z) = \sum_{n=0}^{\infty} \mathfrak{A}_n \cos(\lambda z) + \mathfrak{B}_n \sin(\lambda z) \tag{3.11}$$

$\mathfrak{A}$	The cosine scaling coefficients of the Fourier series.
$\mathfrak{B}$	The sine scaling coefficients of the Fourier series.

$$R(r) = \sum_{n=0}^{\infty} \mathfrak{C} I_0(\lambda_n r) + \mathfrak{D} K_0(\lambda r) \tag{3.12}$$

$\mathfrak{C}$	Scaling coefficients of the Bessel series.
$\mathfrak{D}$	Scaling coefficients of the Bessel series.
I_0	0th order modified Bessel functions of the first kind.
K_0	0th order modified Bessel functions of the second kind.

However, since the magnet does not have an undefined potential at the radial center the second kind of Bessel series is disregarded as it is possible to derive $\mathfrak{D} = 0$.

$$R(r) = \sum_{n=0}^{\infty} \mathfrak{C}_n I_0(\lambda r) \tag{3.13}$$

The values of λ_n can be fixed using the assumption that the scalar field is longitudinally symmetric around the magnetic center.

$$\psi\left(r, \frac{L}{2}\right) = \psi\left(r, -\frac{L}{2}\right) \tag{3.14}$$

L	Length of the simulated area where the scalar potential drops of to zero at each end.
ψ	Magnetic flux.

which means that lambda can be determined by.

$$\lambda_n = \frac{(2n)\pi}{L} \tag{3.15}$$

combining the equations gives the formula for the scalar potential of the magnetic field.

$$\psi(r,z) = \sum_{n=0}^{\infty} \mathfrak{C}_n I_0(\lambda_n r)\left[\mathfrak{A}\cos(\lambda_n z) + \mathfrak{B}\sin(\lambda_n z)\right] \tag{3.16}$$

By partial derivatives of Equation 3.16 with respect to the r and z coordinates it is possible to derive equations for the B_z and B_r components of the field.

$$B_r(r,z) = -\frac{\partial\psi}{\partial r} = \sum_{n=0}^{\infty} \lambda_n I_0'(\lambda_n r)\left[\mathfrak{C}_n\mathfrak{A}_n\cos(\lambda_n z) + \mathfrak{C}_n\mathfrak{B}_n\sin(\lambda_n z)\right] \tag{3.17}$$

$$B_z(r,z) = -\frac{\partial\psi}{\partial z} = \sum_{n=0}^{\infty} \lambda_n I_0(\lambda_n r)\left[\mathfrak{C}_n\mathfrak{A}_n\cos(\lambda_n z) - \mathfrak{C}_n\mathfrak{B}_n\sin(\lambda_n z)\right] \tag{3.18}$$

Combining the terms $\lambda, \mathfrak{A}, \mathfrak{B}$, and $\mathfrak{C}$ into the two coefficients $\mathfrak{F}$ and $\mathfrak{G}$ gives the resulting terms for the B_z and B_r field components.

$$B_r(r,z) = \sum_{n=0}^{\infty} I_0'(\lambda_n r)\left[\mathfrak{F}_n\cos(\lambda_n z) + \mathfrak{G}_n\sin(\lambda_n z)\right] \tag{3.19}$$

$$B_z(r,z) = \sum_{n=0}^{\infty} I_0(\lambda_n r)\left[\mathfrak{F}_n\cos(\lambda_n z) - \mathfrak{G}_n\sin(\lambda_n z)\right] \tag{3.20}$$

$\mathfrak{F}$	$\lambda\mathfrak{C}\mathfrak{A}$.
$\mathfrak{G}$	$\lambda\mathfrak{C}\mathfrak{B}$.

Different approaches to using this expression for the solenoid field will be used to fit the measurements to correlate some of the measured data to a full description of the field. This can be particularly helpful when sensor readings have better quality in some places in the magnet and not others.
This technique will be revisited in the testing section combined with filtering techniques to optimise the use of the sensors.

3.2 Translating fluxmeter

The translating fluxmeter is a sensor specifically designed for solenoid magnets that utilises Faradays induction principle to measure the magnetic field in the aperture.

Translating fluxmeters has previously been used for solenoid measurements of different kinds and has shown to have an accuracy in the 10^{-5} Tesla range.[10][11][12][13] It consists of a PCB with induction coils that is translated through the solenoid magnet along the longitudinal axis. The measurement considered is the voltage induced in the coils of the sensor which relates to the magnetic flux through the surface of the coil.

$$\Phi = \mathrm{B} \cdot \mathrm{S_i} \tag{3.21}$$

Φ	Magnetic flux measured.
B	Magnetic field through the surface.
$\mathrm{S_i}$	Surface of the Coil i.

Equation 3.21 can then be substituted into Faradays law.

$$\mathcal{E} = -\frac{\mathrm{d}(\mathrm{B} \cdot \mathrm{S})}{\mathrm{dt}} \tag{3.22}$$

$\mathcal{E}$	Induced voltage.
t	Time.

When using the translational fluxmeter, an important assumption is that the measurement is initiated from a location outside of the magnetic field. If this assumption holds the relation between the induced voltages and the field becomes.

$$\mathrm{B} = \int_{\mathrm{t_0}}^{\mathrm{t}} -\frac{\mathcal{E}}{\mathrm{S}}\mathrm{dt} \tag{3.23}$$

From equation 3.23 a general conversion of coil voltages to B-field can be derived. The sampling of the sensor is a discrete interpretation of the continuous signal which means that the integral can be expressed as the sum.

$$\mathrm{B} = \sum_{\mathrm{i=0}}^{\mathrm{k}} -\frac{\mathcal{E}_\mathrm{i}}{\mathrm{S}}\mathrm{dt} \tag{3.24}$$

The knowledge of the sensor's placement and the flux induced by the fluxmeter makes it possible to derive some information of the field. Combine this information with knowledge of the movement direction of the sensor, and assumptions about the geometry of the field and it is possible to make elaborate descriptions of the magnets using the fluxmeter technology.
The translating fluxmeter for sweeping solenoid magnets was initially designed for superconducting magnets with relatively strong magnetic fields. However, in this project, the usage is on a normal conducting magnet which needs to guide low-energy electrons and have as little direct impact on the beam as possible. The setup therefore requires a very weak magnet which again will induce a weaker signal than what the original fluxmeter was designed for. For this reason, a new fluxmeter was designed for the normal conducting magnets.
A description of the design of the new fluxmeter is in the following section.

3.2.1 Design

To measure normal conducting magnets that are weaker than the originally intended strong superconductive solenoids, the translating fluxmeter design developed at CERN[10] has been redone in a second version increasing the surfaces of the coils in the PCB significantly.[14]
At the same time, the fluxmeter is equipped with additional smaller radial coils symmetrically distributed around the center of the sensor to allow for a better azimuthal resolution of measurements than previously where the coil had disc coils and sector coils. A sketch of the placement of the coils and the naming convention can be seen in Figure 3.1.

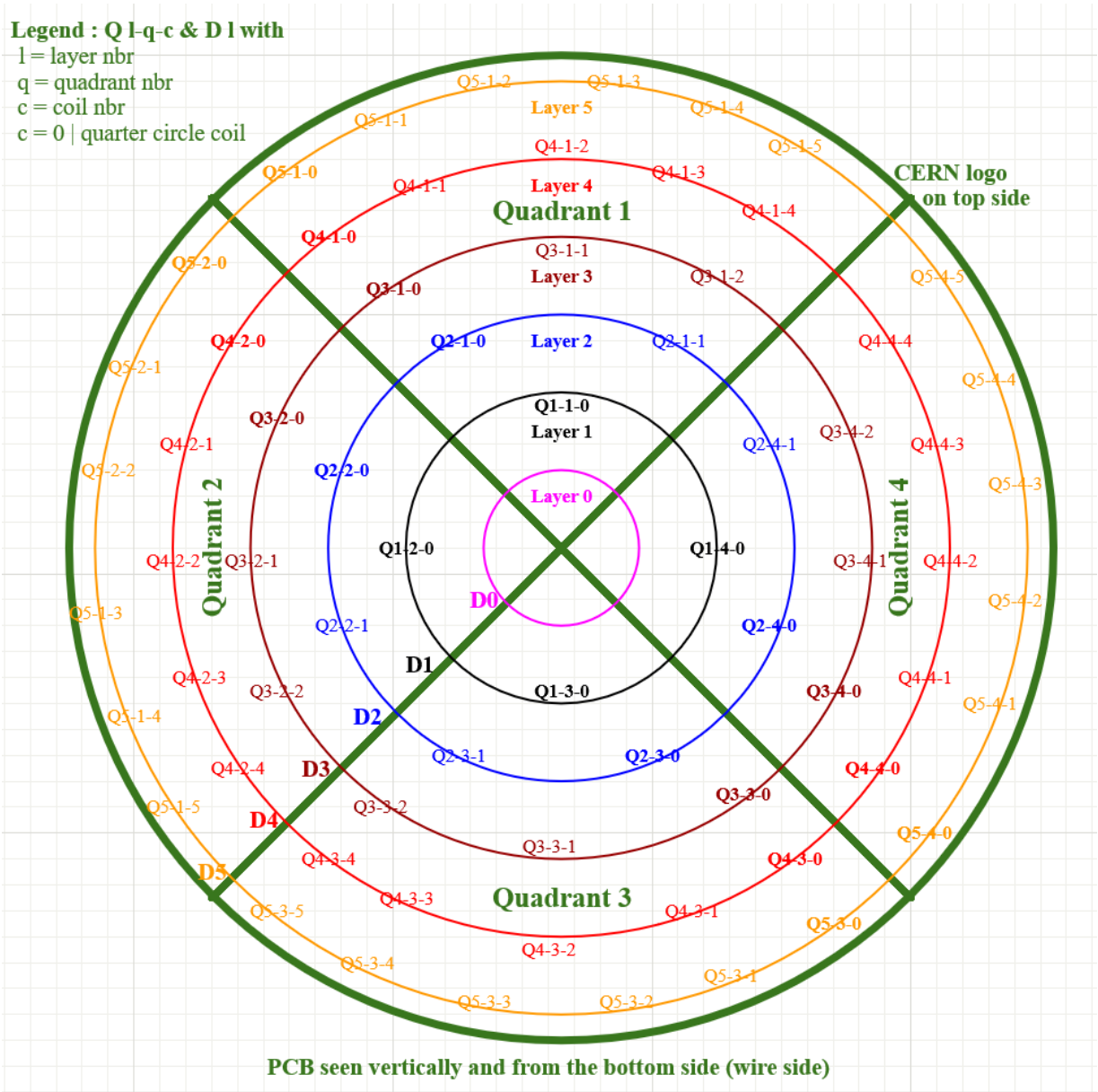

Figure 3.1. A sketch of the new translating fluxmeter with coil naming convention.[15]

The naming convention as seen in Figure 3.1 specifies coils in three groups. D-l, Q-l-q-0, and Q-l-q-c where c is larger than zero.

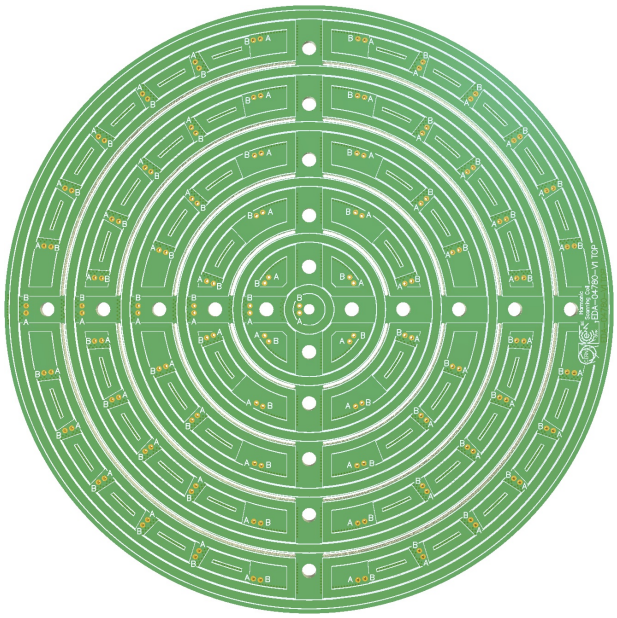

Figure 3.2. A sketch of the PCB from the front where the design and placement of the different coils can be seen.[15]

The coils are placed as illustrated in Figure 3.2. The D-l coils are circles that encompass the surface of the disc, the Q-l-q-0 coils are bent rectangles that encompass approximately $\frac{1}{4}$ of the disc circumference, and the Q-l-q-c coils are the smaller squares that are placed around the disc. The surfaces of the coils starting from layer 0 which is the innermost D-l coil and ranging to layer 5, are calculated as.

Coil	surface m^2
D-5	4,687826917
D-4	3,08
D-3	1,811414324
D-2	0,87667459
D-1	0,27754125
D-0	0,022797782
Q-5-q-0	0,217159694
Q-4-q-0	0,168165868
Q-3-q-0	0,119146979
Q-2-q-0	0,070087613
Q-1-q-0	0,020587879
Q-5-q-c	0,009462062
Q-4-q-c	0,009415021
Q-3-q-c	0,009396782
Q-2-q-c	0,009363059

Table 3.1. Coil surfaces given their type and placement. The Q-coils are only defined by their layer since all coils of the same type in same layer have similar surfaces.

The new fluxmeter with bigger surfaces and better resolution is tested to describe the inherent

noise in the setup where it is used. Some initial noise measurements and an analysis of the impact on the signal is made in the following section to investigate the capabilities of the sensor.

3.2.2 Translating fluxmeter noise characterisation

To gain an understanding of the quality of the sensor output a study of the noise in the sensor and acquisitions are conducted.
Some knowledge is obtained from the first generation of fluxmeters which can be used to initially know some of the behaviour of the signal. A general challenge in measuring the translating fluxmeter is that the voltages measured is measured with electrical equipment that to some degree induces a time-varying noise voltage.
This introduces a drift to the signal due to the integration from Equation 3.23. The measured signal can be described as a discrete sum since no acquisition is continuous and the system thereby relies on an integration between discrete points.

$$\mathcal{E}_{\text{meas}} = \mathcal{E} + \text{v}_{\text{noise}} \tag{3.25}$$

$\mathcal{E}_{\text{meas}}$	Induced voltage readout from the sensor.
v_{noise}	Noise voltage inherent in the system.

which means that the discretely sampled measured flux becomes.

$$\text{B}_{\text{meas}} = \sum_{\text{i=0}}^{\text{k}} -\frac{\mathcal{E}_{\text{i}}}{\text{S}} + \sum_{\text{j=0}}^{\text{k}} -\frac{\text{v}_{\text{j}}^{\text{noise}}}{\text{S}} \tag{3.26}$$

To obtain some characterisation of the noise variable v_{noise} from Equation 3.26 studies of several induction coil measurements is conducted.

Noise analysis

The noise analysis is conducted in multiple steps. First, a raw acquisition with a sampling rate of 50 kHz is sampled multiple times without any intentional magnetic induction in the coils. The magnet is turned on but since the coils are not moved there should be no signal to measure. This means that the most apparent noise sources can be internal electrical noise on the instruments or electromagnetic noise generated from noise in the current signal in the magnet. While not all sources of noise are seen in a measurement like this experiment, it provides an overview of some of the noise sources that are present in an acquisition.

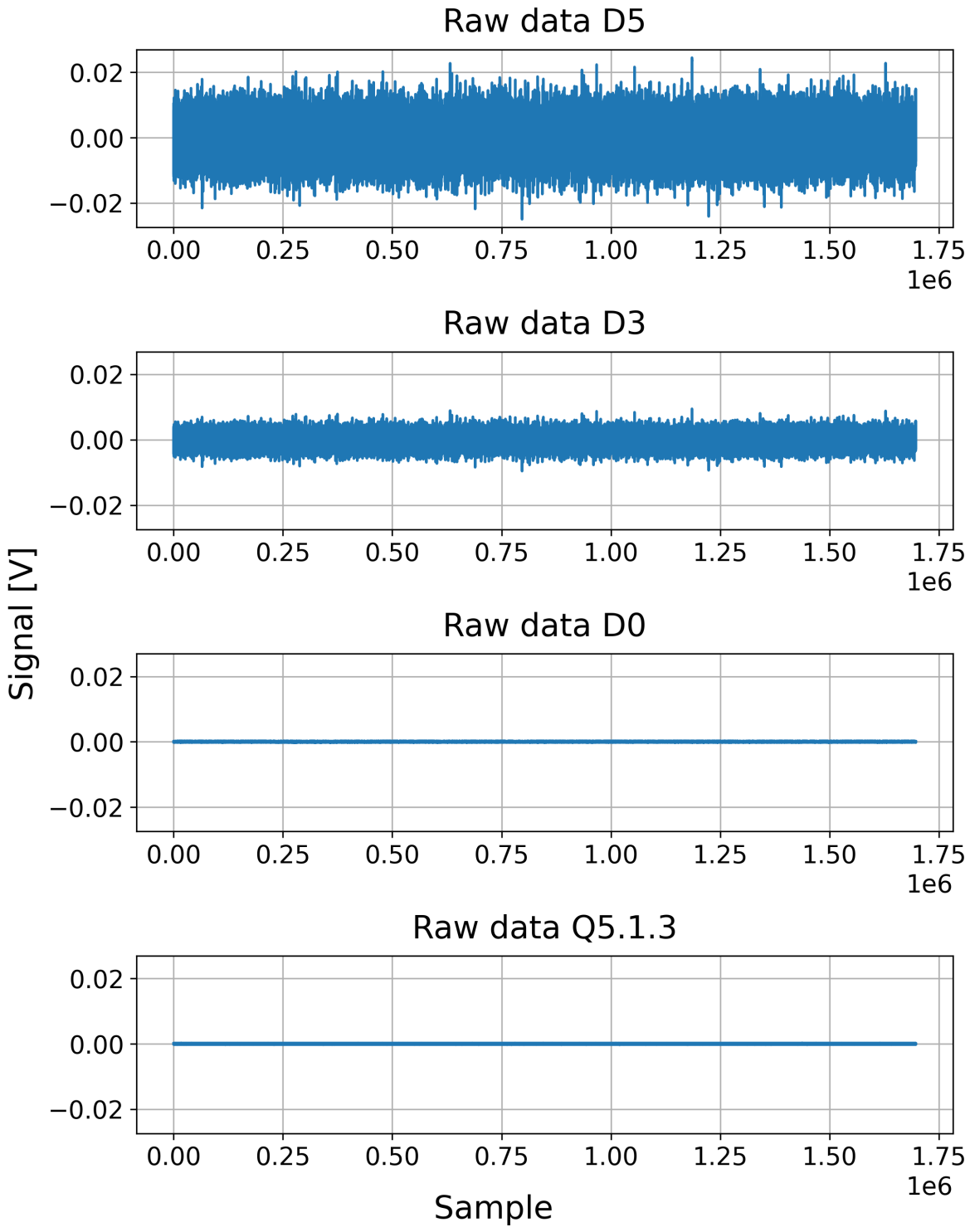

Figure 3.3. Raw acquisitions from the coils D3, D2, D1, and D0.

As seen in Figure 3.3 the voltage signals have a slight offset from a zero mean which can be interpreted as an inherent bias in the measurement acquisition system. This can cause a drift throughout a sample period and is generally assumed constant in the measurement systems. To accommodate this bias offset the mean of the voltage signal is subtracted from all samples before calculating the magnetic flux. The subtraction of the mean will make the magnetic flux

measurement begin and end up in zero, which follows the assumption that all measurements start and end outside of the magnet when using the translating fluxmeter for field mapping. In all further analyses of the noise content, the zero mean signals are used since these are the signals used in measurements.
The spectral content of a noise acquisition shows that the noise is distributed across all measurable frequencies almost equally. Figure 3.4 shows that a linear function fits the scale of the absolute cumulative noise very well. The similarity to a line can suggest that at least some amount of the noise is electromagnetic noise. This line also gives a way of calculating an expected signal-to-noise ratio of a given measurement if the movement speed, the desired coil surface, and the field strength of the magnet is known. The formula for the signal-to-noise ratio can be derived using the expectation of the noise and knowledge from Equation 3.22 where the term d(B)A can be seen as dependent on the velocity of the fluxmeter and the B field as $d(B) = v \cdot B$ since the change in the field is introduced by translating the coil.
The linear fit yields the slope 0.00099 and an offset of 3.27846e-05 which makes the formula for the expected signal-to-noise ratio over a 30 seconds acquisition.

$$\text{snr} = \frac{v \cdot B \cdot S_i}{0.00099 \cdot S_i + 3.27847e^{-05}} \tag{3.27}$$

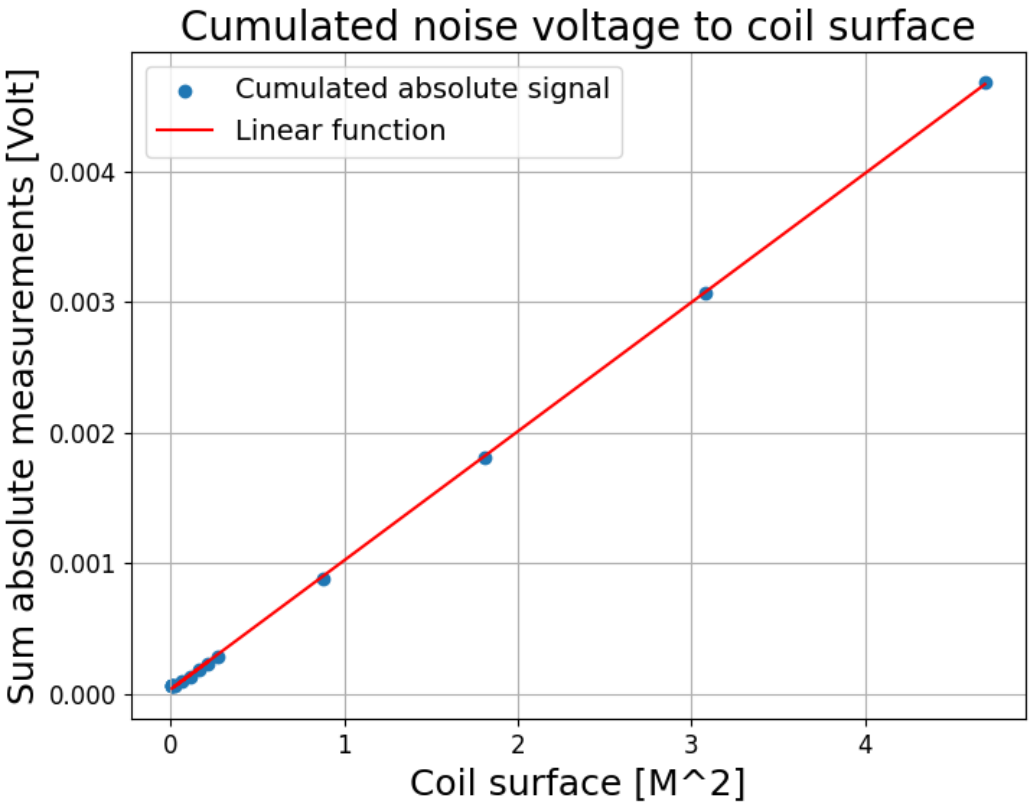

Figure 3.4. A graph of the magnitudes of the cumulative content of the noise signal of all different coils on the fluxmeter.

A feature of interest is also the effect of the inherent electrical noise in the system on each coil. While the inherent electrical noise cannot be decoupled completely from the electromagnetic

noise its effect on the measurement can be determined from the noise signals divided by the coil surfaces. This division by coil surfaces should almost equalise the electromagnetic effects on the coil while scaling the inherent electrical noise with $\frac{1}{A}$. The division by coil surface as seen in Figure 3.5 gives a noise-to-surface pattern that is vastly different from the linear relation where it shows that the smaller coils are way more affected than the large coil surfaces. This also means that while the drift noise over a measurement cannot be completely removed the signal-to-noise ratio can be improved by enlarging the surface of the measurement coil. However, the shape and size of the magnet can affect the possible size of a coil and thereby might limit the surface effect on the signal-to-noise ratio to an upper boundary.

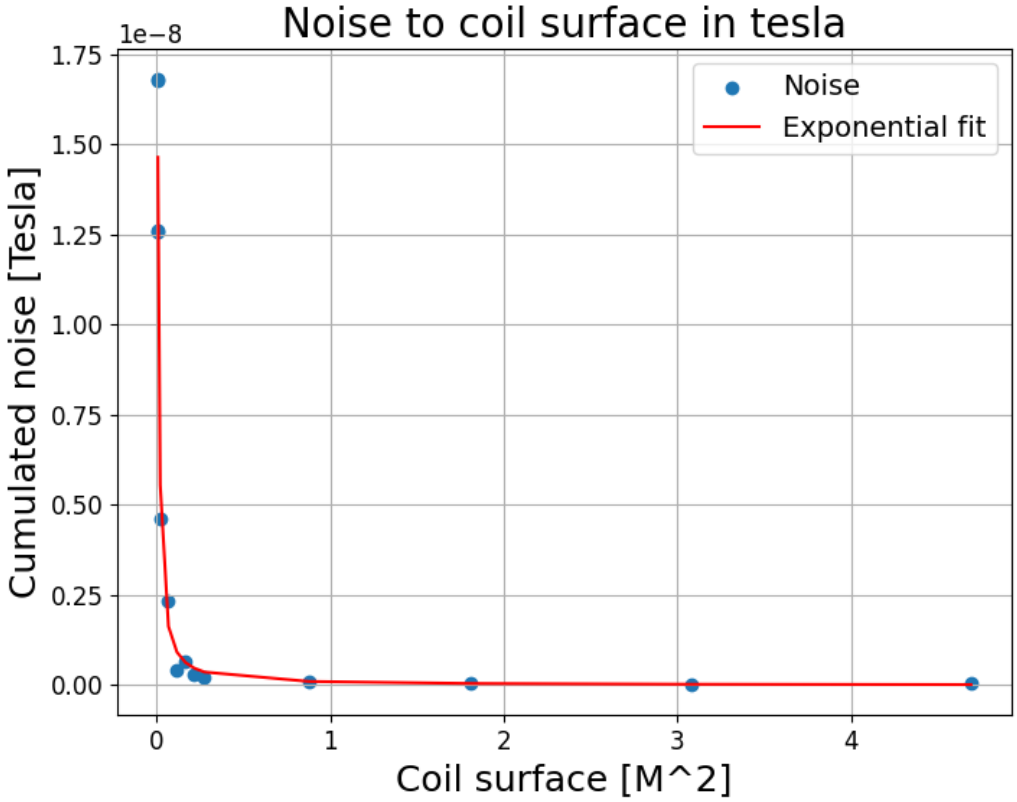

Figure 3.5. A graph of the magnitudes of the cumulative content of the noise signal of all different coils on the fluxmeter divided by the coil surface.

The comparison of the graphs in Figure 3.6 shows that in the frequency domain, the noise has somehow similar characteristics for all the coils, but that the amplitude scales with the size of the coil. This was also documented in Figure 3.4. Most of the noise seems to behave as white noise with an equally distributed amount on all frequencies while it should be heavily minimised when taking the cumulative sum as done in the signal acquisitions.

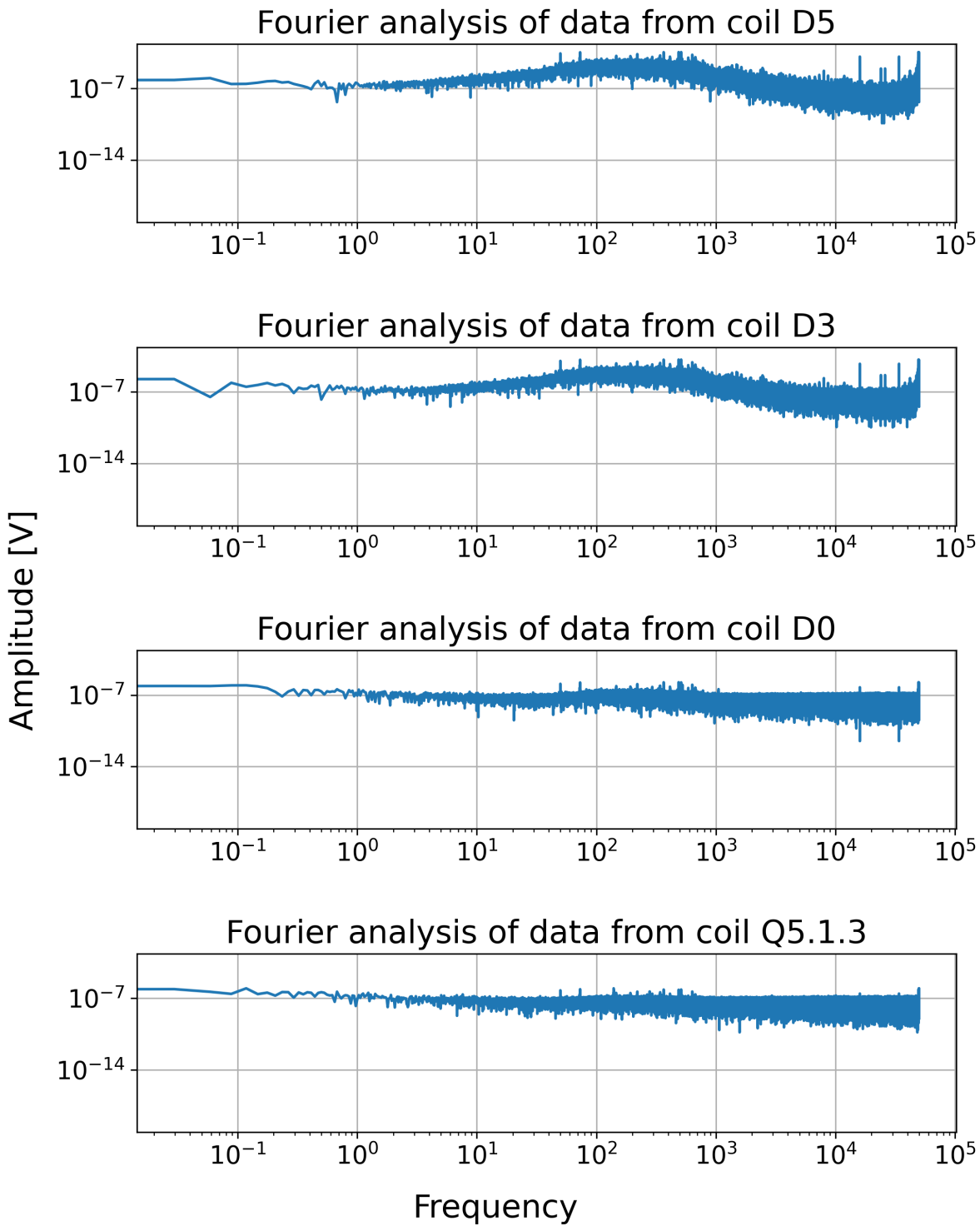

Figure 3.6. Spectral content of raw acquisitions of the fluxmeter, sampled at 50.000 Hz. The image shows acquisitions from the coils D5, D3, D0 and Q5.1.3

The spectral content of the cumulative signal can be seen in Figure 3.7 where the noise-to-coil surface ratio changes behaviour and the low-frequency noise voltage decreases when the size of the coil increases. At higher frequencies up to 700 hz, the larger coils still seem more sensitive than the smaller coils. However, when dividing by the coil surfaces the low-frequency content

dominates the noise behaviour in comparable measurements of the magnetic field.

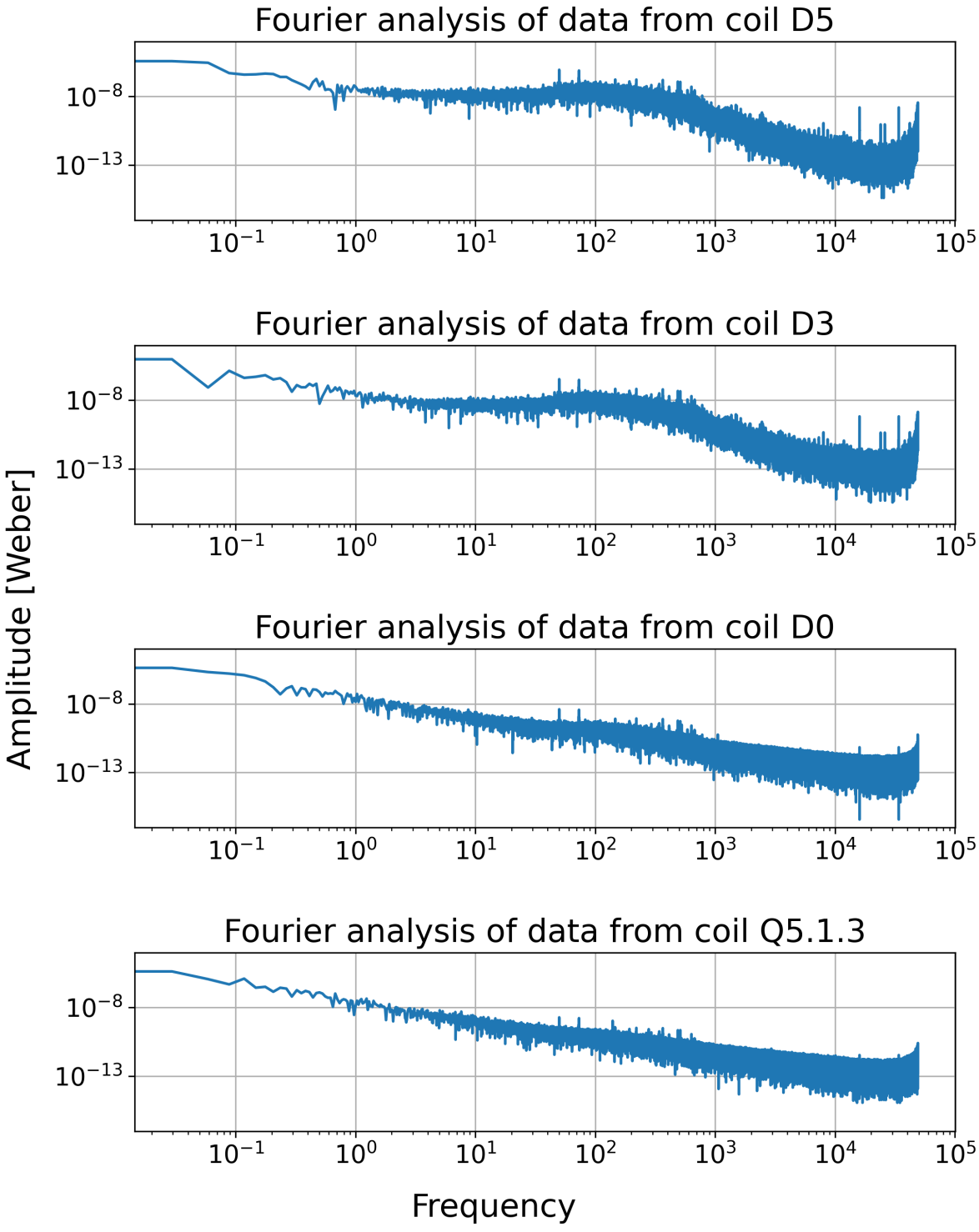

Figure 3.7. The spectral content of cumulative sum of the raw acquisitions of the fluxmeter, sampled at 50.000 Hz. The image shows acquisitions from the coils D5, D3, D0 and Q5.1.3

A plot of the cumulative sum of the noise acquisition can be seen in Figure 3.8 where the high-frequent noise has a larger impact on the bigger coils while the drift of the signal is within the

same amplitude order of magnitude on all coils.

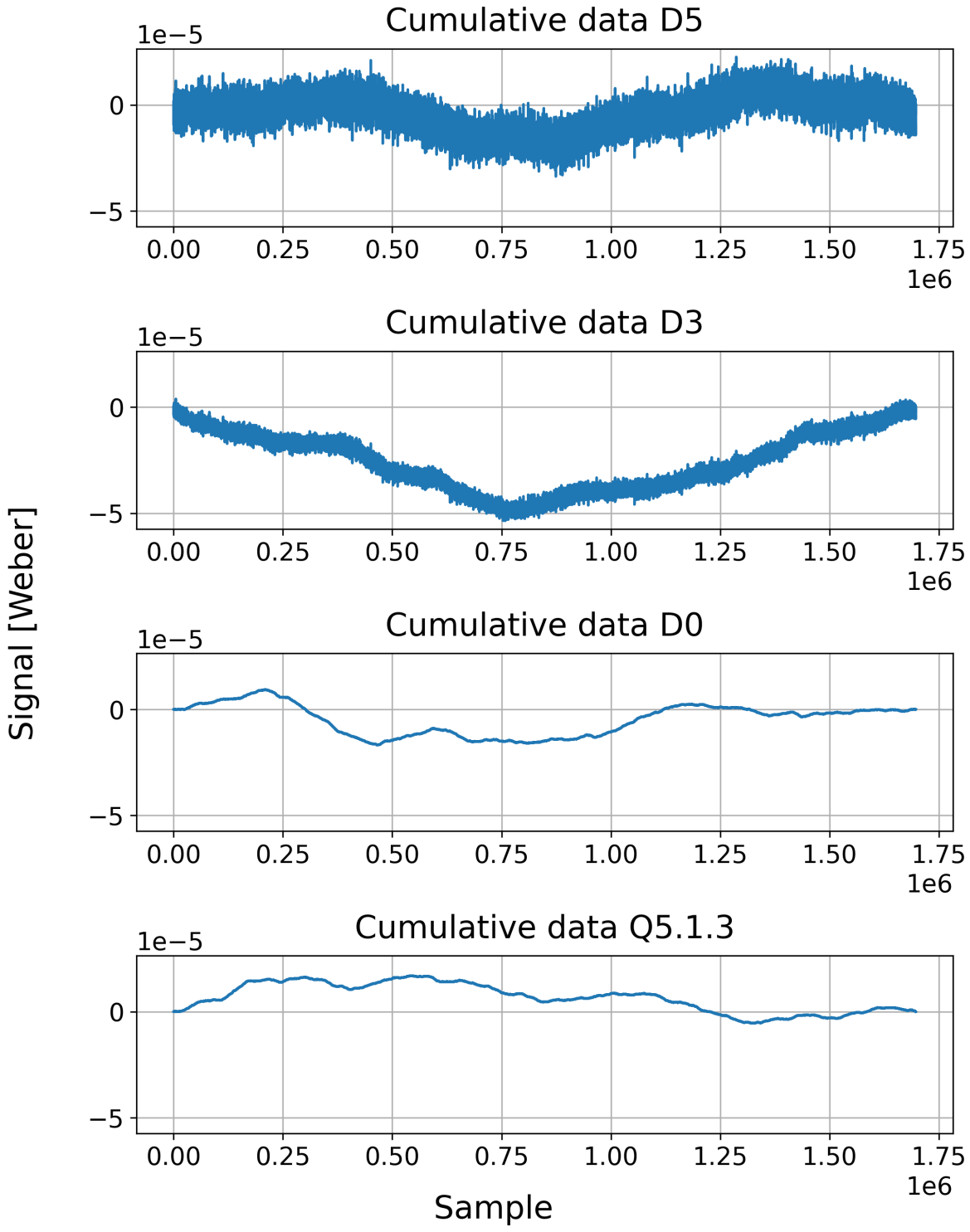

Figure 3.8. A cumulative sum of the noise acquisition without any scaling from coil size.

In Figure 3.9 it can be seen that when divided with the surface of the coil, the high-frequent noise in the larger coils becomes insignificant and the best quality signal becomes the signals received through the larger coils.

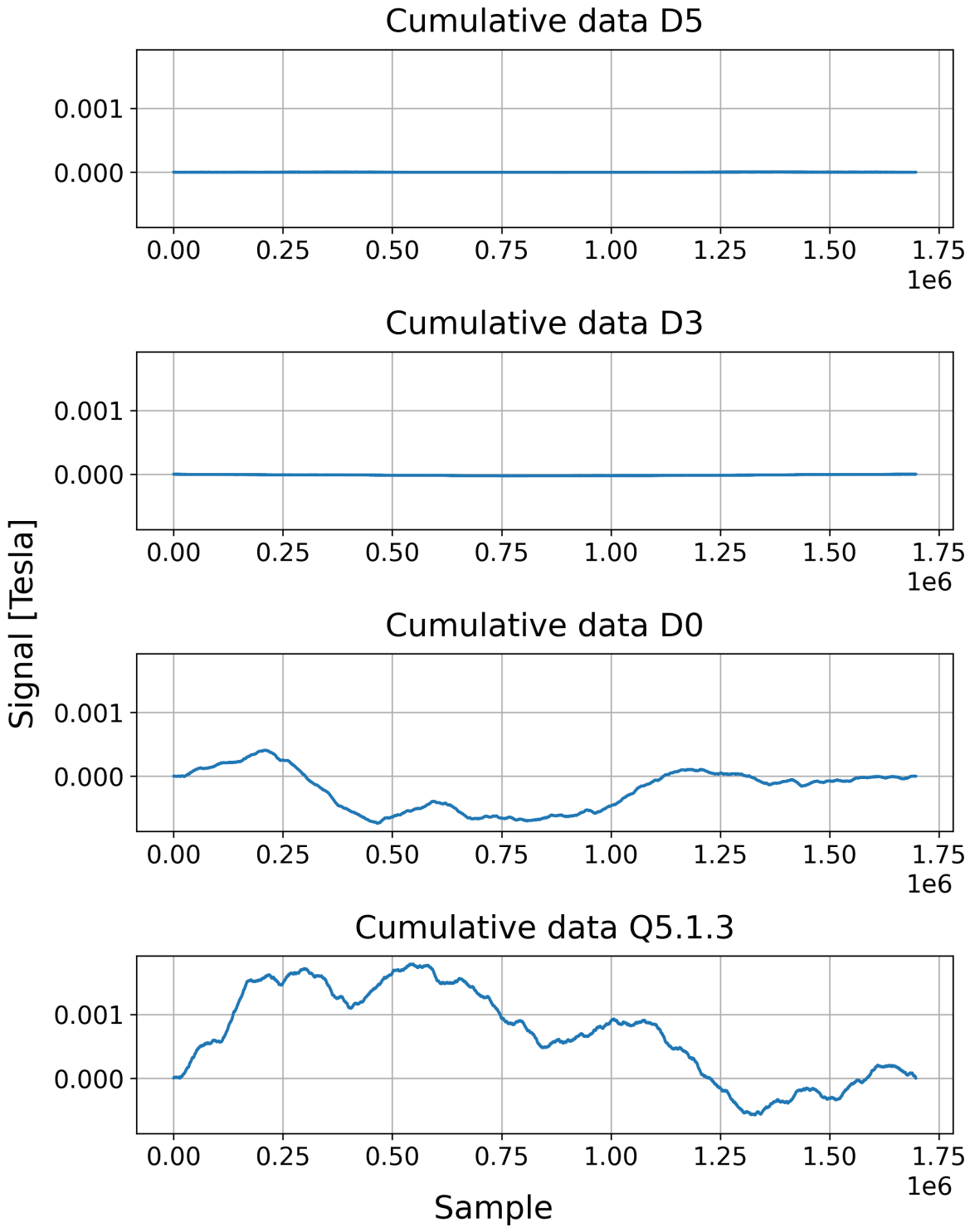

Figure 3.9. The cumulative noise signal from figure 3.8 scaled with coil sizes.

The analysis of the noise content shows that the largest error in field measurement arises from the low-frequent noise on the smaller coils, since the signals are dependent on the coil size the noise will similarly be scaled with that coil size. The result means that the smaller the coil the larger the effect on the signal. Any way to increase the amount of signal in the acquisition will similarly improve the signal-to-noise ratio. While this section explores a basic understanding of

some of the unknown noise components of the magnet the next will address the general ways of extracting field components from the magnetic measurements performed with a translating fluxmeter.

3.2.3 Extraction of field components

The field components making up the solenoid field B_z, B_r and B_Φ are of importance when analysing whatever content is in the solenoid magnet. Fitting the measurement to an infinite series also needs the different components of the field since the solution relates to how the field propagates in the different coordinates. The B_z and B_r field components going through the disc coils are extracted from the sensor by two different formulas that are known.
The B_z field is calculated as.

$$\bar{B}_{z,i}(z_k) = \frac{\psi_i(z_k)}{S_i} \tag{3.28}$$

$\bar{B}_{z,i}$	Measured B_z field by coil i.
z_k	The longitudinal position at the kth measurement.
ψ_i	Measured magnetic flux through coil i at z_k.
S_i	The surface of coil i.

And the B_r field is calculated as.

$$\bar{B}_{r,i}(z_k) = \frac{\psi_i(z_k) - \psi_i(z_{k-1})}{2\pi r_i (z_k - z_{k-1}) N} \tag{3.29}$$

r_i	Radius of coil i.
N	Number of turns of coil i.

However, this information extraction in itself is only tested on a pure solenoid magnet where the relation between the B_z and B_r fields are known and on the disc coils which does not give the information of the misalignment of the field expected from the external coils. In the new sensor, a way to read out the field center displacement can be by comparing the measurement readings from the new symmetrically distributed coils.
The field extraction is a way to infer what information is in the coil when translated through the magnet. With an understanding of the induction principle generating the voltages measured in the coils and a way to express the measurement as field components, it is possible to do some preliminary measurements with the coil and an experimental setup.
The next section will contain a description of the experiment setup followed by some preliminary measurements expressed as the longitudinal field B_z.

3.3 Fluxmeter measurement

A scan of a solenoid magnet is conducted to test the quality of the measurements of the fluxmeter. This scan will be related to the knowledge from the data from section 3.2.2 and the surfaces from section 3.2.1.
The measurements are performed with the setup used throughout all of the project.

3.3.1 Experimental setup

The test setup consists of the elements used to generate the magnetic measurements of the solenoid.
The system contains the following equipment.

- Tube for guiding the fluxmeter through the aperture of the magnet.
- Pole for translating the fluxmeter through the aperture of the magnet.
- A fluxmeter installed at the end of the translation pole.
- An acquisitions system.
- A Leica camera for position readings.

Figure 3.10. Whole translation system with the tube in the aperture of the magnet and the sliding system on the right side of the image.

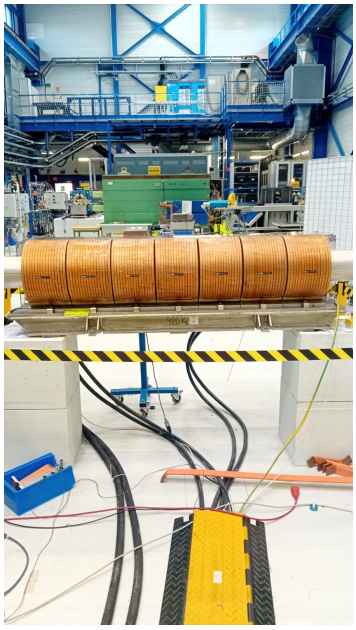

Figure 3.11. The magnet seen from the side.

The full setup of the magnet can be seen in Figure 3.10 where the tube starts on the right and follows through the magnet which can be seen from the side in Figure 3.11. Also visible in Figure 3.11 is that the magnet consists of seven sections. However, only the rightmost section seen from the figure is used for the initial tests of the 2. version fluxmeter to simplify the measurements.

Sliding system

The sliding system consists of a tube to guide the sensor and a pole to pull or push the measurement head through the tube. The tube is aligned as precisely as possible through the magnet. The pole is fixed in position with a 3D-printed device to keep it from rotating while translating since an unknown amount of random rotation would render the internal relations between the coils unusable with the current setup.

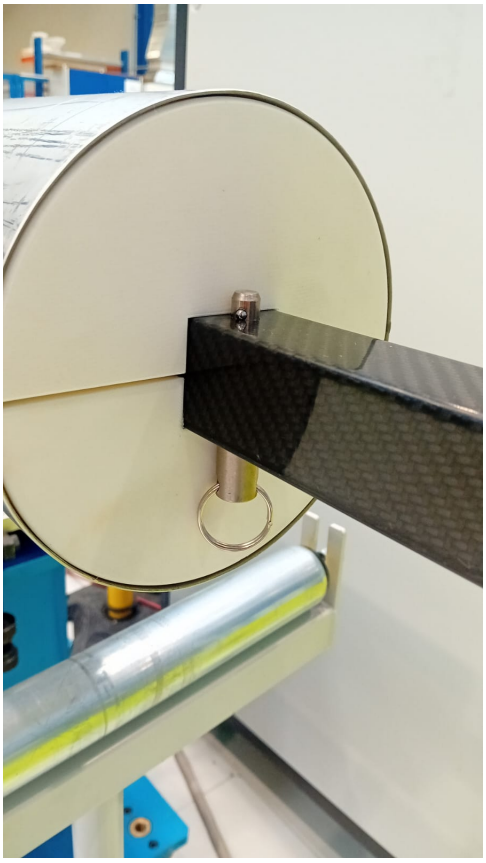

Figure 3.12. The round 3D printed fixture that locks the sliding pole in place to avoid rotations. The metal rod through the sliding pole serves as a mechanical stop, limiting the amount of the translation and keeping the measurement head in the tube.

In Figure 3.12 the 3D-printed part can be seen in the tube where it is aligned and fixed with screws. In the pulling rod, a stopping mechanism is fixed to avoid pushing the measurement head too far while a stopping mechanism for pulling it too far is inside of the tube.

Measurement head and panel

The sensor is attached to the sliding pole using a machined measurement head where the wires from the sensor can run through to the acquisition system. The wires from the sensor are attached to a panel that gives a manageable interface when attaching the acquisition system wires. An overview of the panel that is designed to resemble the board and avoid cabling mistakes when rapidly changing configurations can be seen in Figure 3.14.

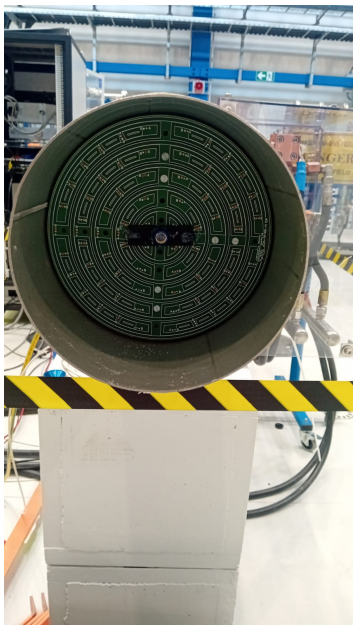

Figure 3.13. The fluxmeter disc in the tube through the magnet.

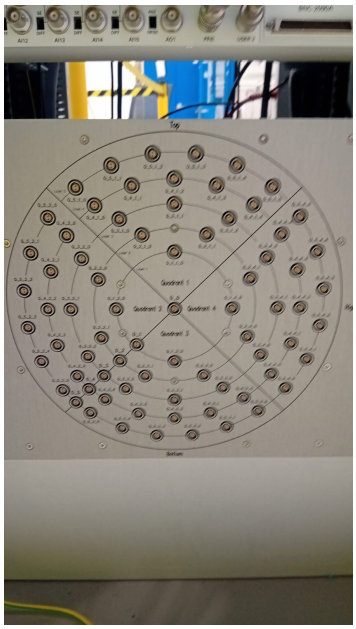

Figure 3.14. The patch panel connecting the wires from the fluxmeter to the FDI acquisition device.

In Figure 3.13 a picture of the fluxmeter attached to the translating system is shown and in the middle of the disc a reflector is attached for the Leica tracker to give a 3D position of the fluxmeter at the fixed sample frequency.

Acquisition system

The measurements are made with CERN's developed fast digital integrator[16]. The system can sample at a rate of 500 kHz and integrates the samples between triggers which means that we can sample at rates where the rest of the equipment which has significantly lower sampling frequencies can also be used.
In Figure 3.15 the cabling from the specially designed pact panel to the fast digital integration channels can be seen. The figure also adds simple cabling of the sensor to avoid errors.

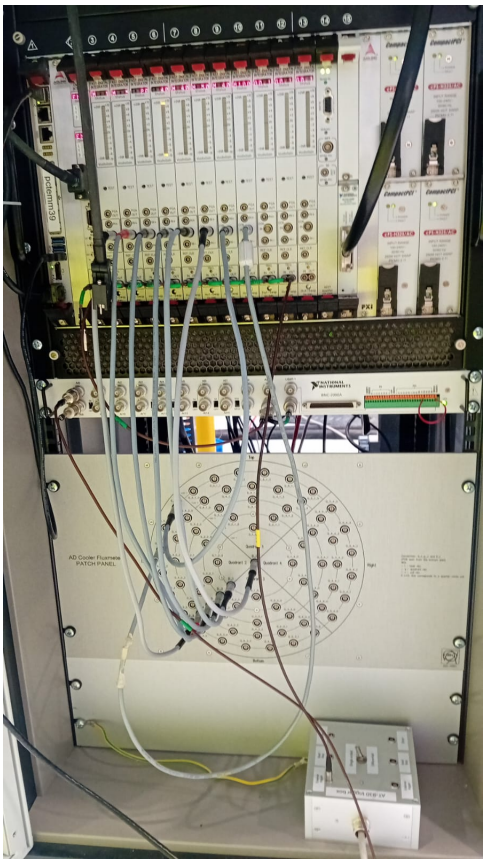

Figure 3.15. An image of the acquisition system used to sample the fluxmeter measurements.

Leica laser tracker

To track the absolute position of the sensor and thereby have the magnetic field mapped as a result of the spatial coordinates instead of just the sample number, the Leica laser tracker[17] is installed and triggered with the same external signal as the acquisition system. The simultaneous triggering ensures that there is an absolute positional measurement for every measurement sample.

3.3.2 Measurements

With the setup described in the preceding section, a sample of 11 acquisitions on the fluxmeter is measured.
The acquisitions are made with a sampling frequency of 1024 hertz which is the highest frequency where the camera has shown to be able to keep up.
In Figure 3.16 the measurement from the FDI's is plotted directly without more postprocessing. It is obvious from the graph that there have been inconsistencies in the movements and different movement speeds. The inconsistencies are seen in the large differences in how the graph moves, and the change in speeds can be seen on the maximal and minimal ΔTesla values where the larger values are induced by a faster movement speed. The difference in velocity also results in various amounts of time samples which results in a big difference between the signals when plotted on the z-axis.

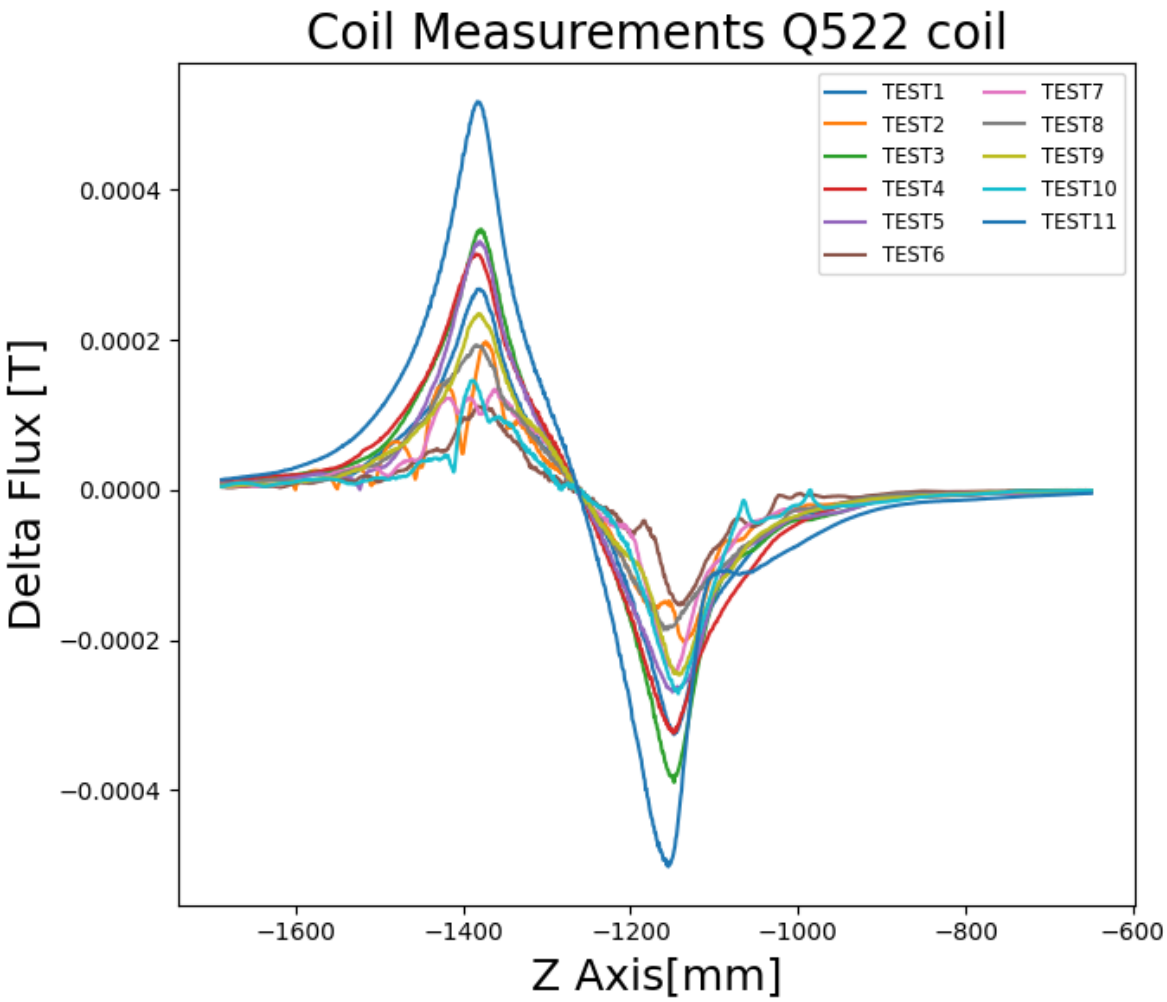

Figure 3.16. The unintegrated measurement of the solenoid magnet taken with the Q522 coil.

Integrating the signal results in the magnetic flux in the magnet. In Figure 3.17 it can be seen that even though the signals look very different in Figure 3.16 they come from the same underlying signal. The quality of interest is the ability to describe that particular underlying signal.

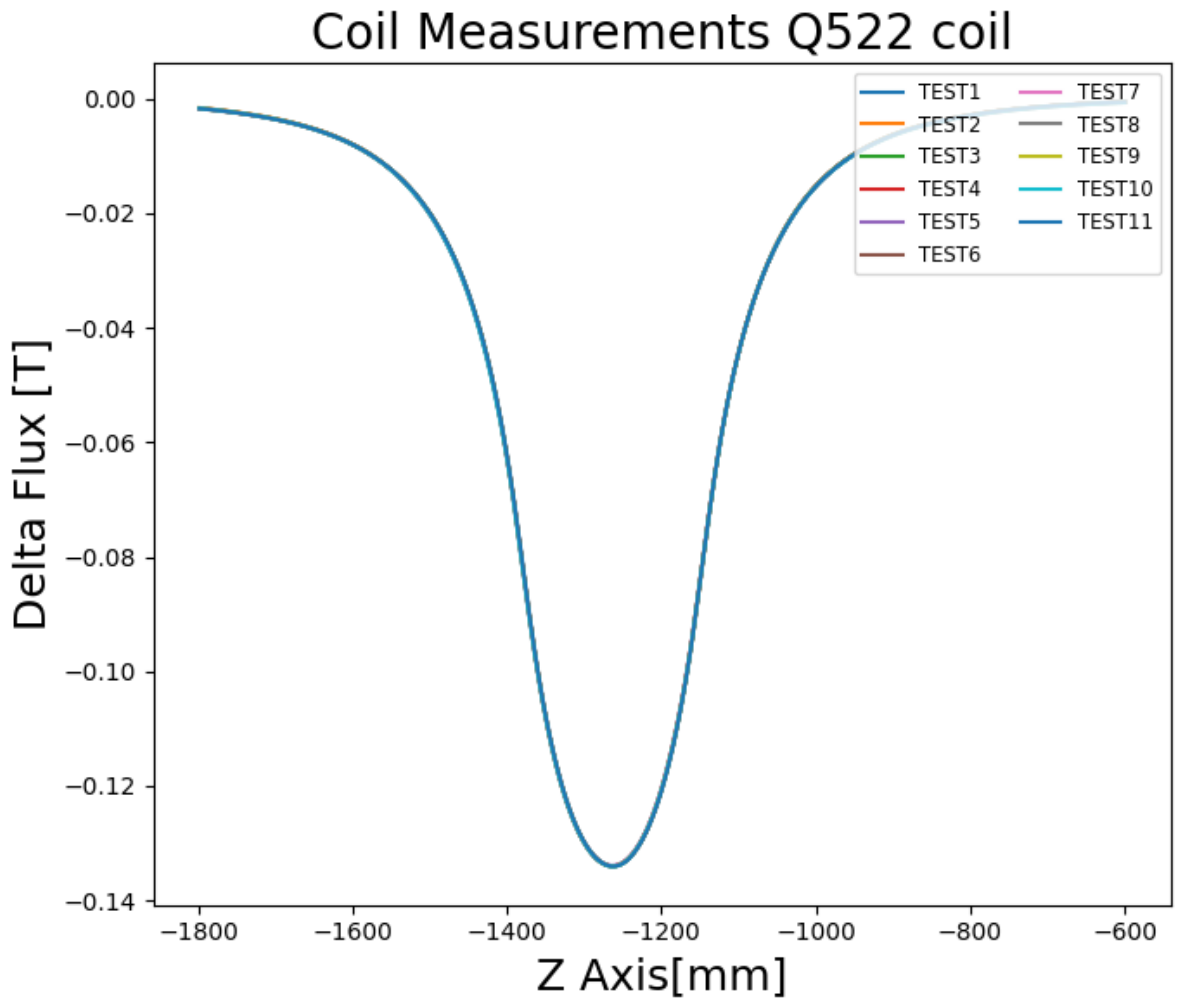

Figure 3.17. The integrated measurement of the solenoid magnet.

One way to describe the quality of the capturing of the induced signal is to investigate the repeatability of the measurement when performed multiple times. However, error does not only arise from the measurement imperfections but also from positional uncertainties induced by the Leica camera. The positional uncertainty effects on the errors of the signal are most prominent where the gradient is the steepest.

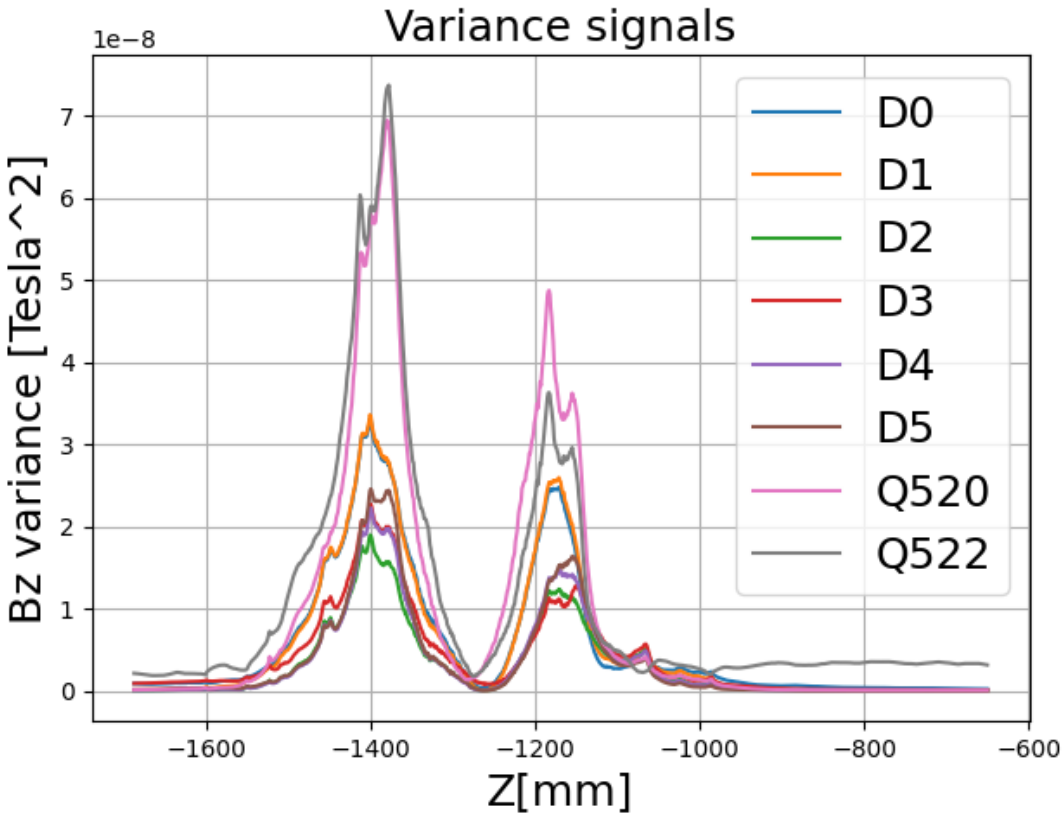

Figure 3.18. The unintegrated measurement of the solenoid magnet.

The variance of the measurement as a result of position can be seen in Figure 3.18 where the D5, D4, D3, D2, D1, D0, Q520, and Q522 coils are measured to have a broad spectrum of surfaces to compare. The variances in Figure 3.18 shows that the uncertainty in the measurements scales inversely with the coil surface where the smaller coils have a larger variance.
The peaks of the Q522 measurements from Figure 3.17 can be seen in Figure 3.19 where the difference over multiple measurements becomes more visible.

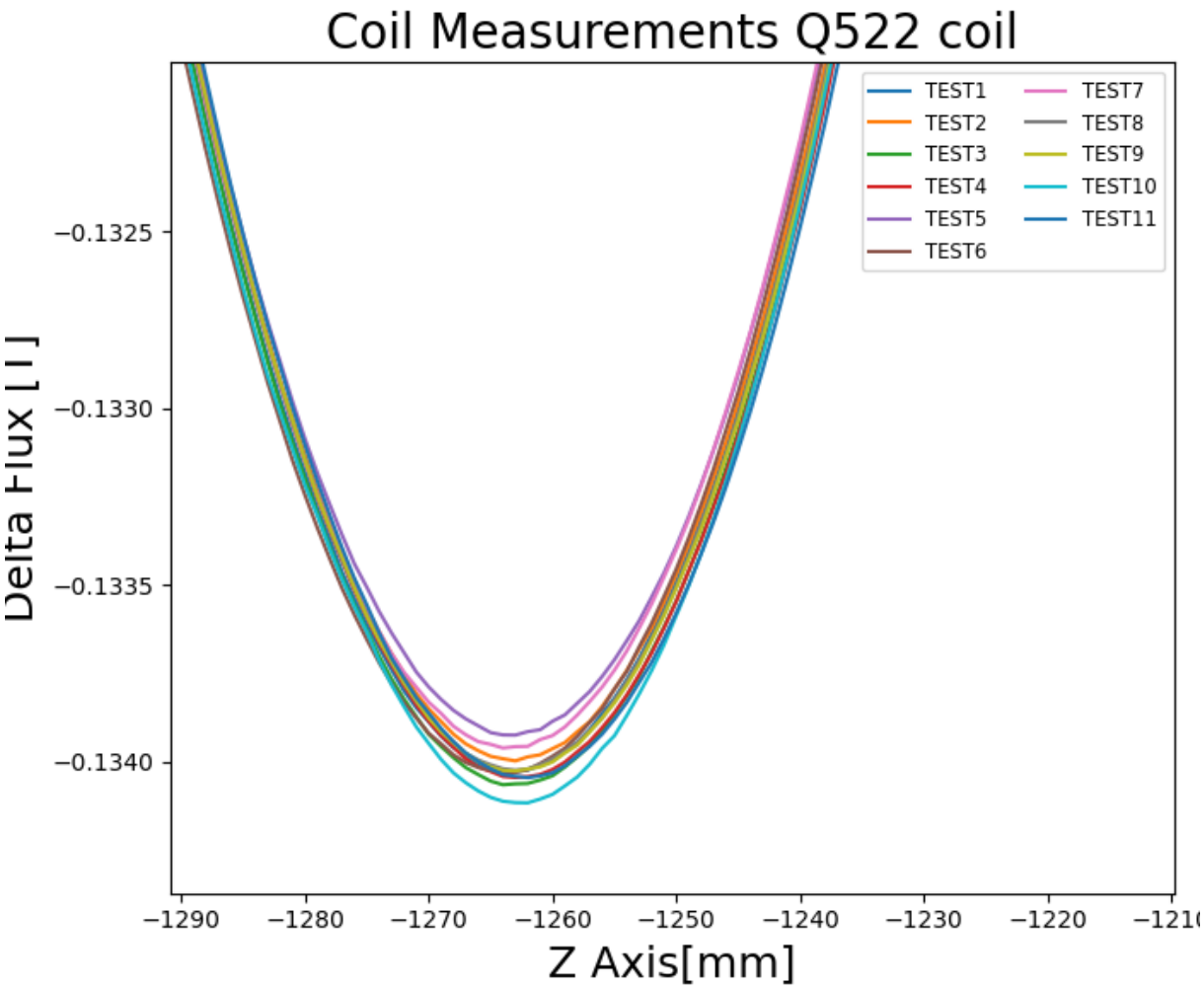

Figure 3.19. A zoomed image of the 11 acquisitions on the Q522 Coil where the differences between each acquisition becomes visible.

In the next section the problem of measuring a solenoid magnet with best possible precision is revisited and the electron cooler project goals is analysed defining a scope of further work.

3.4 Problem limitation

While the general measurement campaign will begin to take place in 2025 and by then a fully developed way of measuring the field of the magnet will have to be developed and tested.
The problem of measuring the drift solenoid and separating the field components from the solenoid field and the external dipoles are the general goal of the antimatter project. Due to the novel approach to this task, some preemptive work have to be done. One important task is the understanding of the signal and different post-processing options in case the measurement in its raw form is not enough to obtain the required accuracy.
Another task is minimising the mechanical contribution to the imperfections of the measurement. That work will encompass building a test setup with every source of imperfection being at least considered and alleviated or brought to a minimum.

Also, the general approach to how the field measurement relates to the different components of the solenoid magnet is needed to differentiate the external dipole contribution from the original solenoid field.
In this thesis, the scope is limited to the measurement principles of the sensor to gain information about the magnet, and post-processing techniques that can improve the quality of the measurement.
General improvements of the setup that might be necessary to limit some of the mechanical effects will not be of larger concern even though an investigation of this is important for completing the electron cooler project.
Since the disc has well-defined ways to measure the radial and even more the longitudinal field components the signal processing will be applied to the measurement of the longitudinal B_z field component.
The next chapter will present an approach to deal with the low-frequency noise components present in the signal using a Kalman filter.

Signal processing 4

While the tests from section 3.2.2 show that the sensor, in general, has a very good performance on large coils, the drifting noise on smaller coils might be of concern when measuring the magnet. In situations where the information stored in the difference between the smaller coils is of importance for the extraction of information about the magnet, the drift can be an issue.
One approach to dealing with unwanted drift can be to apply filters that make information from sensors less or not affected by drift. Kalman filtering can be particularly interesting for this correction due to the already proven cases where it is applied. This section revolves around the design and implementation of a filter to reduce low-frequency noise and provide a cleaner signal.

4.1 Kalman filtering

From section 3.2.2 it can be seen that the quality of the measurement relies on the size of the coil. However, in section 3.2.1, it can be seen that some of the coils of interest are in a size range, which can cause trouble for the quality of the signal. There are multiple ways of trying to avoid the drift in the signal, one of which is Kalman filtering, where, if the noise is removed, the low-frequent drift noise on the smaller coils can be mitigated.

4.1.1 Additional sensor inputs

In general, the Kalman filter utilises the ability to combine different sensors and recursively update the best estimate of a signal given multiple estimations of it. This section describes all sensors considered and limits the choices of interest.

Magnetic compass

One sensor solution used in the design of the previous electron coolers is the magnetic compass developed in Novosibirsk where the displacement of a magnetic needle is used as a result of the field lines which can then be used as a measure of the dipole components of the field in the region of interest.[18]

Hall probe

Hall probes are another sensor type that has been used in multiple electron cooler setups. The advantage of a Hall probe is that it gives an absolute measurement of the field at each point. The Hall probe uses the Hall effect to measure the strength of the magnetic field perpendicular to one direction. The Hall effect is the displacement of electrons running across a conductive plate due to the Lorenz force.[19]
The Hall probe's ability to measure the magnetic field on a single axis requires multiple sensors combined for a three-dimensional resolution of the field, which can cause problems. Other challenges in the use of Hall sensors are the nonlinear response to temperature and field changes.

Additional fluxmeters

Another solution to fuse the signal and gain more relevant information about the magnetic field is to add multiple coils that measure the same as the initial fluxmeter.
If the noise in the fluxmeter is zero centered, a sufficient amount of fluxmeters will average out to a very small error in the measurement. Another possible solution is placing fluxmeters particularly sensitive to some of the field components of interest in a more complete sensor for the particular task. However, the number of sensors needed to reduce the noise with multiples of the same sensor makes it infeasible to solve the noise issues with this system in the current setup.

Nuclear magnetic resonance

Nuclear magnetic resonance sensors use the fact that the spin of a known particle can align with a magnetic field.[19]
When the aligned particles are then reacted upon by another magnetic field, they will oscillate with a frequency proportional to the strength of the field with which the particles are aligned.
By finding the resonance frequency of the particles, the field strength can be determined very accurately. The nuclear magnetic resonance sensors can, however, only measure the field strength and not the direction of the field. Another possible drawback of the nuclear magnetic resonance sensor is that it can have a lower bound to the measurable field strength, where the fields of interest in electron coolers are generally very low.

Filtering Using coils on the same disc

Given that the signal from the fluxmeter is split into multiple channels, each delivers a separate measurement of a point in the magnet. Fitting the larger coils to some fitting models might provide a reference signal that can be used to filter the smaller coils if needed. Different models can be used as the corrective signal depending on the magnetic field of interest and which field needs to be explored. The filtering using coils from the same disc has two different drawbacks.

Sensor selections

The sensor selections are done on the background of feasibility and availability.
The nuclear magnetic resonance sensor is used since it is not direction sensitive, and it is not a setup that is easy to apply together with the fluxmeter, making it unsuited in practicality and functionality. The magnetic compass is direction-sensitive and could, in principle, be used with other sensors. However, the development of the magnetic compass for a specific magnet is a large and time-consuming effort in itself and, thereby, not an applicable solution to this project. The Hall sensor is also functional and has previously been used to measure magnets for electron coolers.

4.1.2 Filter application

The Kalman filter is finite-impulse-responsest applied to the longitudinal field B_z of the magnet. The filter is made under the assumption that the magnetic system can be approximated from the state space equations.

$$B_z = B_{z-1} + Y_z^f \tag{4.1}$$

B_z	The magnetic flux at position z.
B_{z-1}	The magnetic flux at the previous position z.
Y_z^f	The measurement from the fluxmeter at position z.

$$Y_z^f = \Delta B_z + u_z \tag{4.2}$$

u_z	the noise induced at the measurement taken at position z.
ΔB_z	the increment in magnetic flux between the previous position z and the position z.

$$Y_z^h = B_z + w_z \tag{4.3}$$

Y_z^h	The measurement from the Hall sensor at position z.
w_z	the noise induced at the measurement taken at position z.

If the values are already expressed in the unit tesla, the measurements and states can be expressed as scalars, the system and control input matrices both equate to one which is why they can be left out of the equations. The same relation can be seen between the measurement of the system and the system state. The general calculation of the B field is an integration of the ΔB measurements, so another important assumption is that the samples are taken with fixed time intervals.
Using an absolute measurement and an incremental measurement enables the filter to be formulated from the idea used in inertial-measurement-unit-driven Kalman filters where the model is driven forward with an incremental measurement and corrected with an absolute measurement.[20]
Representing the state as the magnetic field B and the lowest frequencies of the noise on the

fluxmeter makes it possible to approximate the drift of the signal and subtract it during the integration of the fluxmeter signal.
Initially, an attempt to apply the filter simply by using the difference between the estimates as the drift was done which results in the equations.

Prediction/propagation step

$$B_z^- = B_{z-1} + Y_z^f - D^k \tag{4.4}$$

B_z^-	State before the update step.
B_z^+	State after the update step.
D^k	Drift estimate .

$$P^- = P^+ + P^f \tag{4.5}$$

P^-	Variance after the current prediction step.
P^+	Variance after last update step.
P^f	Variance of the fluxmeter measurement.

Update step

$$K = \frac{P^-}{P^h + P^-} \tag{4.6}$$

P^h	Variance of the Hall sensor measurement.

$$B_z^+ = B_z^- + K(B_z^- - Y_z^h) \tag{4.7}$$

$$P^+ = (1 - K) \cdot P^h \tag{4.8}$$

$$D^k = B_z^+ - B_z^- \tag{4.9}$$

The issue with this approach is that the high-frequency noise from the Hall sensor seems to enter the signal and make the resulting estimate unstable. To accommodate this instability in the estimate of the drift, an extra step is added where the high-frequency noise from the Hall sensor is not allowed into the signal as far as possible. The new method makes use of the fact that the low-frequent noise component in the fluxmeter is strongest and that the noise drops orders of magnitudes when going towards the higher frequencies.
The issue of the high-frequent noise means that estimating the D^k variable in the low-frequency domain might be beneficial instead of using the raw difference between estimates.

Drift estimation in frequency domain

The drift of the fluxmeter comes from the noise in the electric system and can be estimated as $\frac{1}{f}$ noise that is inherent in the electrical components.
Correcting the drift of the system with an absolute measurement from the Hall sensor, however, introduces the signal to a very high-frequent noise with a large amplitude. While the variance of the fluxmeter and the Hall sensor determines a Kalman gain on the signal updates, the estimate of the drift is channeled through a different process.
The challenge in this sensor fusion is to filter the signals in a way that can correct the drift without introducing the frequent high-frequency noise from the Hall sensor. The attempt to make this drift approximation is done through an finite-impulse-response filter on the difference between the Hall measurement and the model with the fluxmeter increment. The finite-impulse-response filter is designed to look like the expected noise in the frequency domain, and the infinite series of coefficients is then multiplied on a cyclic buffer that keeps track of the n latest values. In Figure 4.1 an example of tracking the low-frequency noise is put forth. The finite-impulse-response attempt to find the estimated drift as the difference between the drifting measurement-driven propagation model and the absolute value with little to no drift is to make the function $\frac{1}{f}$ in the frequency domain and map it to a series of coefficients that are also scaled to give a gain of 1. However, the function $\frac{1}{f}$ corresponds to an infinite series in the time domain. The truncation of shortening it to a non-infinite number of variables introduces an error in the frequency response. To the estimate D^k, the difference $B_z^+ - B_z^-$ instead of being used directly is saved in a vector.

$$\begin{bmatrix} B_z^+ - B_z^- \\ 0 \\ \vdots \\ 0 \end{bmatrix} + \begin{bmatrix} 0 & 0 & \cdots & 0 \\ 0 & 1 & \cdots & 0 \\ \vdots & \vdots & \ddots & \vdots \\ 0 & 0 & \cdots & 1 \end{bmatrix} \cdot \begin{bmatrix} e_1^- \\ e_2^- \\ \vdots \\ e_n^- \end{bmatrix} = \begin{bmatrix} e_1^+ \\ e_2^+ \\ \vdots \\ e_n^+ \end{bmatrix} \tag{4.10}$$

e^- | Error vector from previous iteration.
e^+ | New error vector.

Then D^k is estimated as.

$$\begin{bmatrix} \varepsilon_1 \\ \varepsilon_2 \\ \vdots \\ \varepsilon_n \end{bmatrix} \cdot \begin{bmatrix} e_1^+ \\ e_2^+ \\ \vdots \\ e_n^+ \end{bmatrix} = D_z^k \tag{4.11}$$

ε | Coefficients of a low or band pass filter.

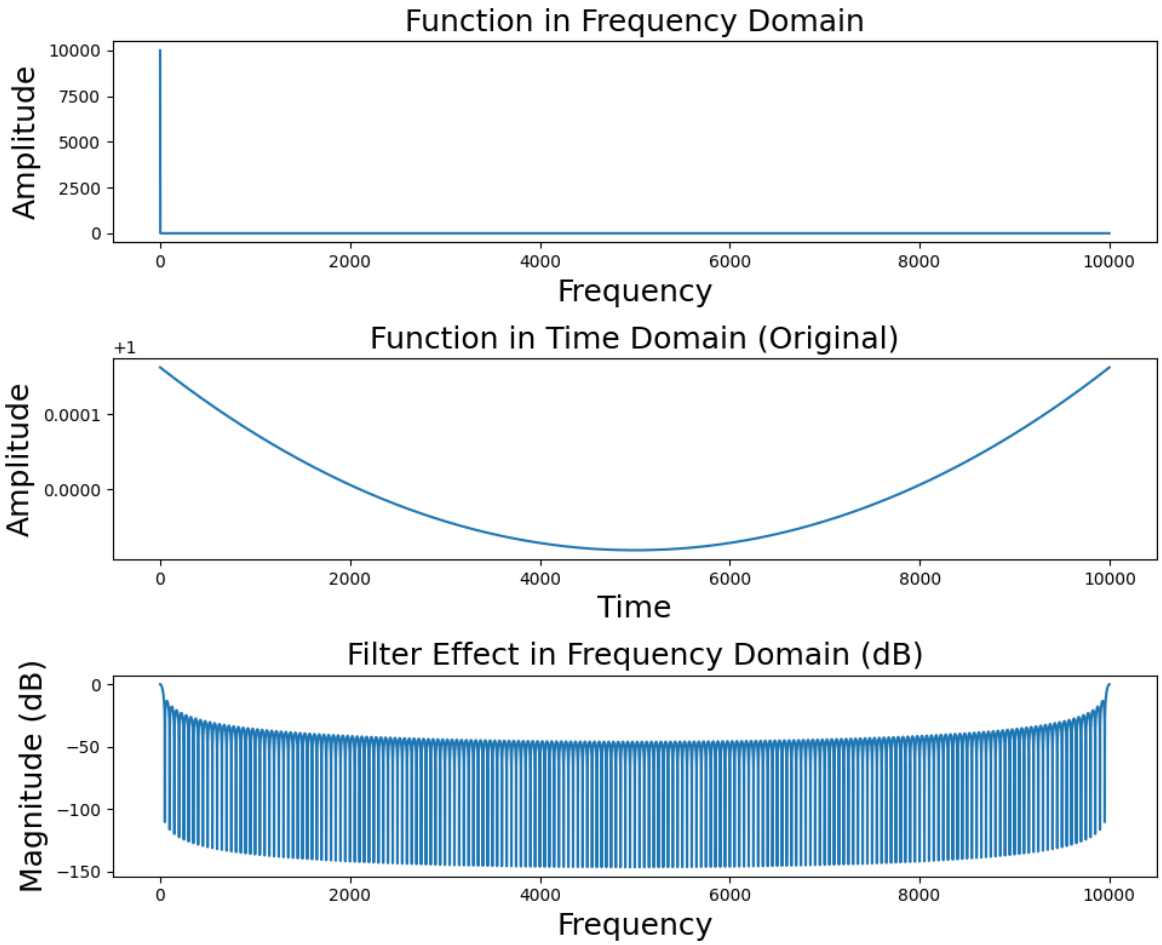

Figure 4.1. The plots of the process in the design of filter coefficients for the $\frac{1}{f^2}$ filter approximation. The top plot shows the initial $\frac{1}{f^2}$ function, the second plot shows the inverse Fourier transformed function while the third picture is the Fourier transform of the filter with 200 coefficients.

An example of the frequency domain design of the filter can be seen in Figure 4.1, where 200 coefficients are used. The trade-off when designing these filter coefficients is that the delay of the drift estimation compared to the actual drift increases with more coefficients. In contrast, the truncation of removing coefficients will result in adding a larger gain to the high-frequency noise. While the trade-off between a desired noise response and a suitable reaction time from the filter is hard to accommodate, another approach might offer a more desirable frequency response with fewer coefficients.

Drift estimation using Chebyshev filter

Another approach to fit the estimate of the drift to the low-frequent noise without delay from many coefficients is using low-order infinite-impulse-response filters. A Chebyshev filter with a sharp cutoff frequency has been chosen as a case study for this implementation. The chosen Chebyshev filter for simulation was made with a cutoff frequency of 0,4 Hertz, which gives a bode plot as seen in Figure 4.2

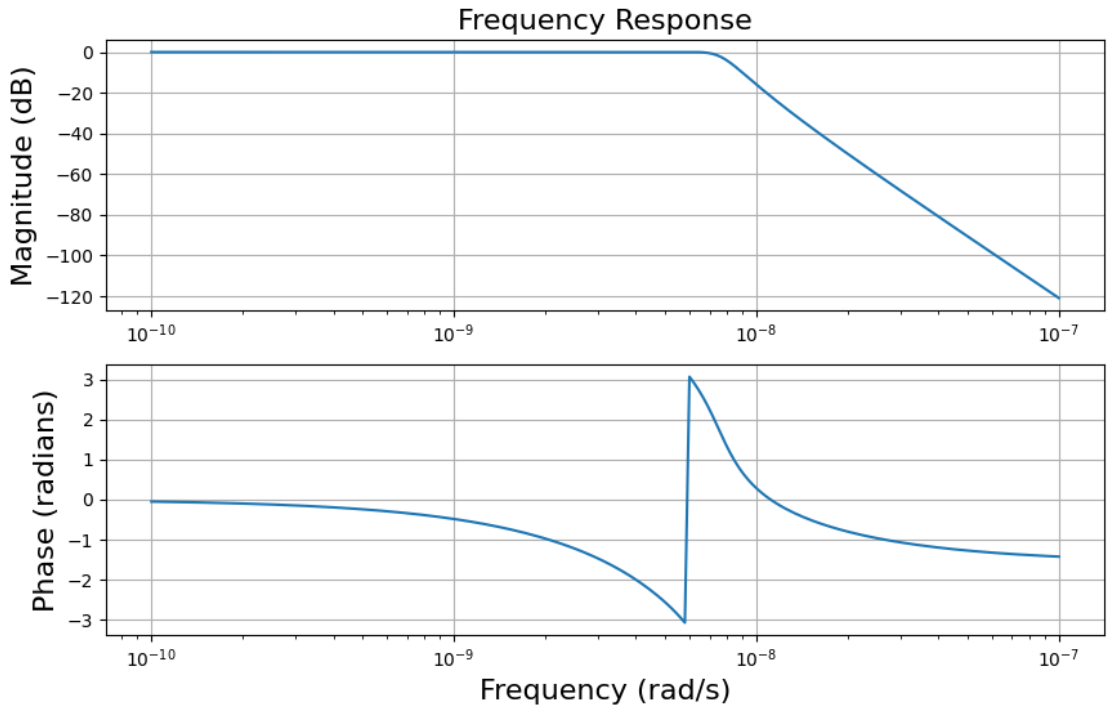

Figure 4.2. A bode plot for the filter used for bias estimation in the simulated environment.

As in the previous filtering method, the filter is applied to the difference between the propagated coil-driven model and the absolute measurement. Likewise, the estimate of the drift is used to update the state incrementally throughout the measurement.
The different methods are tested in a simulation before choosing an approach for further testing against measurement data previously used for filtering magnetic measurements. The following section describes the development of a measurement simulation in which filtering is applied.

Measurement simulation 5

To test the Kalman filter's ability, a simulation of the magnetic measurement system is used to explore the effects of the filter methods and the input signals on the output results. The simulation is written in Python and can produce different sensor readings of a predefined underlying signal.

5.1 Simulation development

The general goal of the simulation is to have a framework for comparisons of signal processing methods where the underlying signal is known. The main functionality is to create a structure that allows the creation of sensor models based on knowledge of the noise characteristics and sampling methods. From the created sensor models and the simulated data acquisition, a comparison between applied filters can be made to evaluate different approaches against a known reference.

5.1.1 General simulation overview

The general overview of the simulation will present the tools available and the intended use of the tools. Later in the following subsections 5.1.2 and 5.1.3 the particular use cases in this project for the initial studies of filtering techniques are laid out. The generally intended flow of the simulation environment is as seen in Figure 5.1, where the initial reference signal is converted to vectors of sensor measurements with some defined sampling frequency, which can be studied or used for filtering. To expand the functionality to other types of measurements, the framework can easily support more references, sensors, and filters than the ones used, particularly for this project.

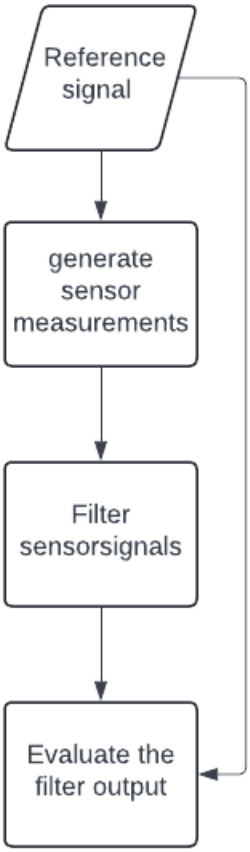

Figure 5.1. The straightforward intended use of the simulation tool.

For each specific sensor type, a block of code that specifies the conversion from underlying signal to acquisition is needed.
The block uses studies of noise and sampling techniques to define the needed additions to the signal. Before being sampled as a measurement, the signal undergoes the process seen in Figure 5.2, where uncertainty is added as a noise vector with a given spectrum and amplitude from the predefined noise functions in the noise generation class.

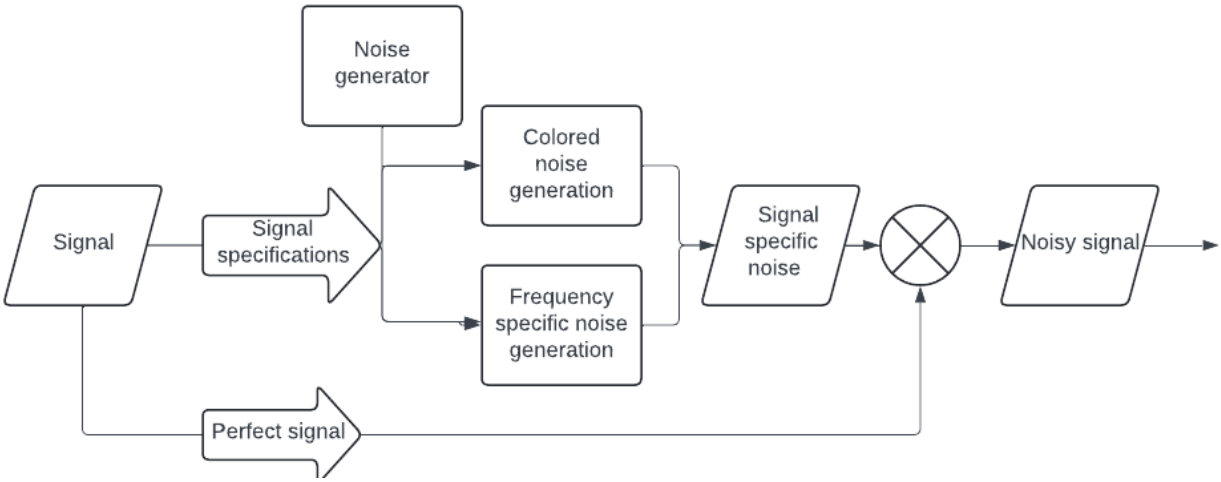

Figure 5.2. The general flow of noisy signal generation.

The generation of the reference signal and the sensor models used are described in the following sections.

5.1.2 Reference signal

The reference signal used in the simulation can be multiple signals that have different abilities. A B_z field component from a simulated model is used for initial testing. The model of a field is extrapolated from Biot-Savart equations applied to a cylindrical spacecurve. The spacecurve is a three-dimensional curve L_c from the vector function.

$$L_c = \begin{bmatrix} x = \sin(t \cdot 2 \cdot \pi) * r \\ y = \cos(t \cdot 2 \cdot \pi) * r \\ z = \frac{(t \cdot l)}{n} \end{bmatrix} \tag{5.1}$$

L_c	The space curve used to describe the turns of the magnet.
r	The radius of the magnet.
t	The incremental variable of the spacecurve.
x	x coordinate.
y	y coordinate.
z	z coordinate identifying the longitudinal axis of the magnet.

From Equation 5.1, it can easily be seen that L_c is rotating around and propagating along the z-axis as illustrated in Figure 5.3.

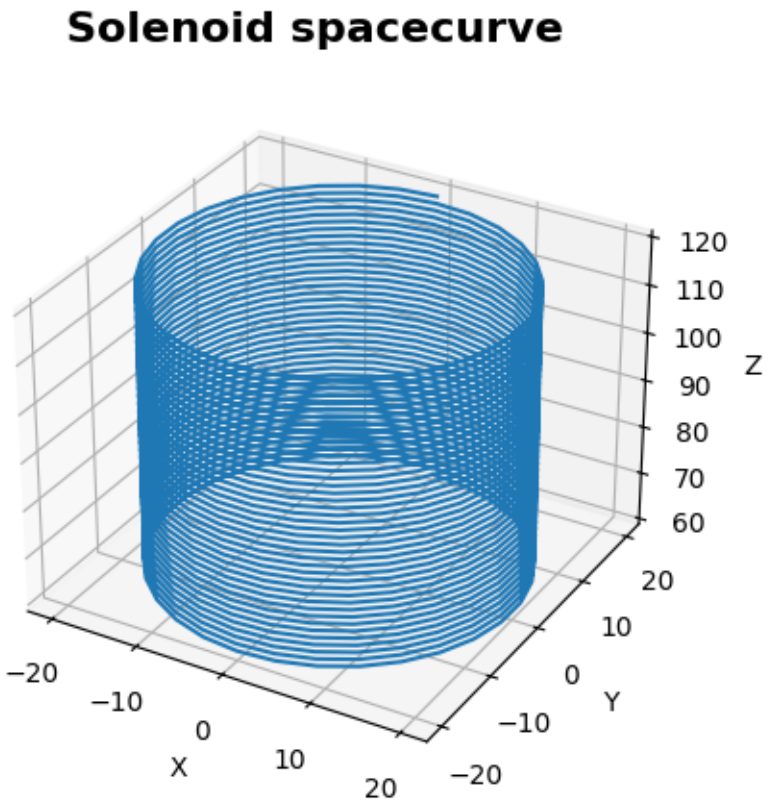

Figure 5.3. A 3D spacecurve L_c for computing an artificial solenoidal field.

Another spacecurve L_z described as a line along the z-axis is then defined. For each point on L_z, the magnetic vector contribution from each point on L_c is evaluated and summed to make an approximation of a solenoid field along L_z The evaluated fields along $L_z = \{z, 10, 10\}$ can be seen in Figure 5.4 where all three field components are included.

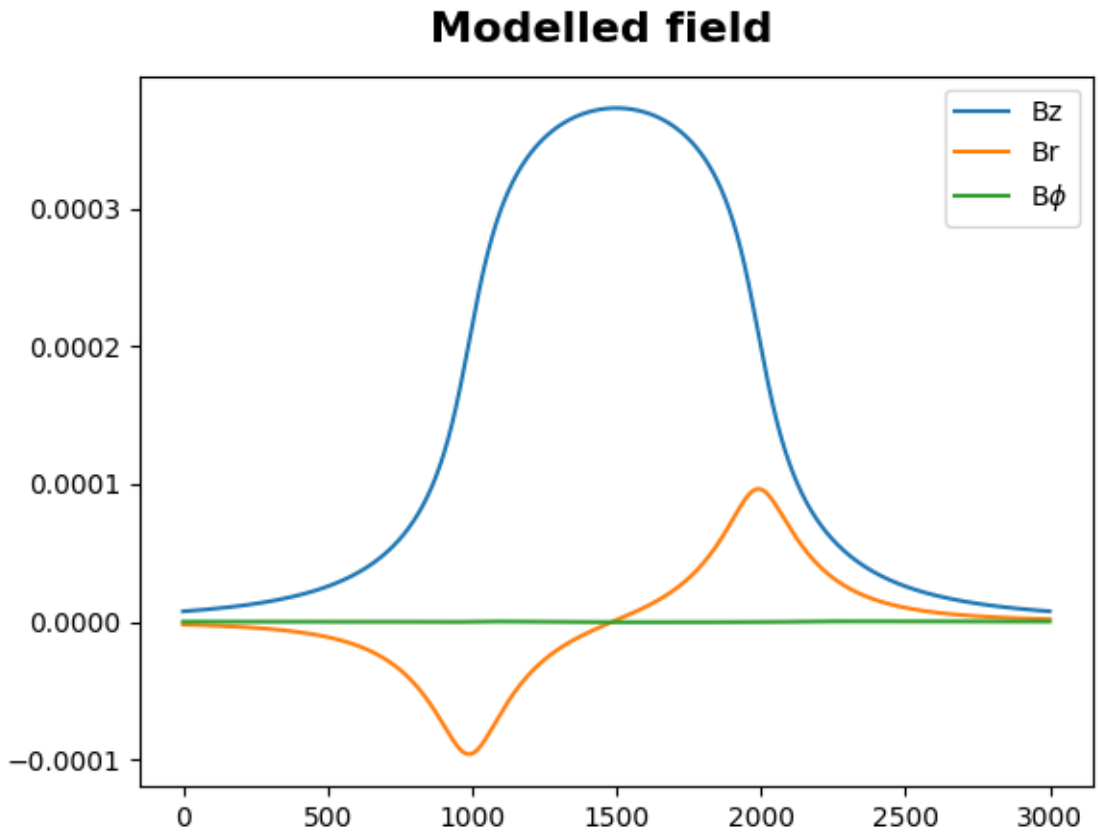

Figure 5.4. Field modelled along L_z.

For the proof-of-concept initial filter test, the B_z field component is chosen as it is the most regularly used measurement in a solenoid field.

5.1.3 Sensor modelling

The sensors are modelled by adding noise components to the underlying signal and mimicking the sampling of the signal.
The vector of samples is then the sensor measurement in the simulation. There are 2 types of sensors in the simulation the fluxmeter and the Hall sensor since these are deemed the best combination.
The sensor measurements are done by adding noise to the true signal and then sampling as done by the specific sensor as shown in Figure 5.2.

Colored noise generation

The coloured noise is created using an approach from astrophysics published in 1994[21] describing a fast way to generate different kinds of colored noise.
The method is based on sampling Gaussian distributed random variables as the real and complex

coefficients of a complex number sampled for each frequency in the Fourier transform of the desired time series.
Each random value is then multiplied by $(\frac{1}{\omega})^{\frac{\beta}{2}}$ where β is defined by the desired type of noise. That means that the Fourier transformed series is.

$$f(\omega_k) = A_k(\frac{1}{\omega_k})^{\frac{\beta}{2}} + iB_k(\frac{1}{\omega_k})^{\frac{\beta}{2}} \tag{5.2}$$

f	the Fourier series of the desired time series.
ω_k	The k^{th} frequency of f.
A_k	The real random Gaussian variable at ω_k.
B_k	The complex random Gaussian variable at ω_k.
β	The coefficient determining the type of noise.

The Fourier values for the negative frequencies are chosen by taking the complex conjugate of the value at $f(\omega_k)$.

$$f(-\omega_k) = f^*(\omega_k) \tag{5.3}$$

Doing the inverse Fourier transform of f then gives the time series used to add to the signal for the noise type defined by β corresponding to the table 5.1.

β	Noise color
-1	Blue
0	White
1	Pink
2	Red

Table 5.1. β values corresponding to different colors of noise.

Whatever time series created is in the code multiplied by a scalar determining the amplitude of the noise before adding it to the time series.
Examples of the spectrum of the pink and white noise can be seen in Figure 5.5 and Figure 5.6

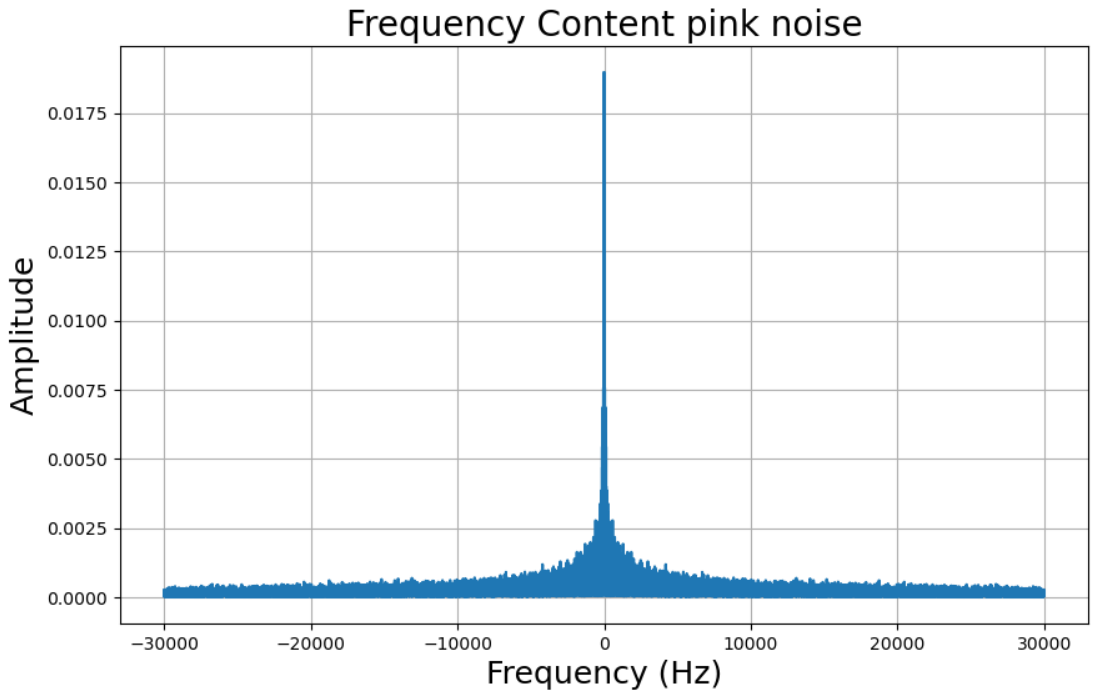

Figure 5.5. Frequency domain representation of the pink noise signal.

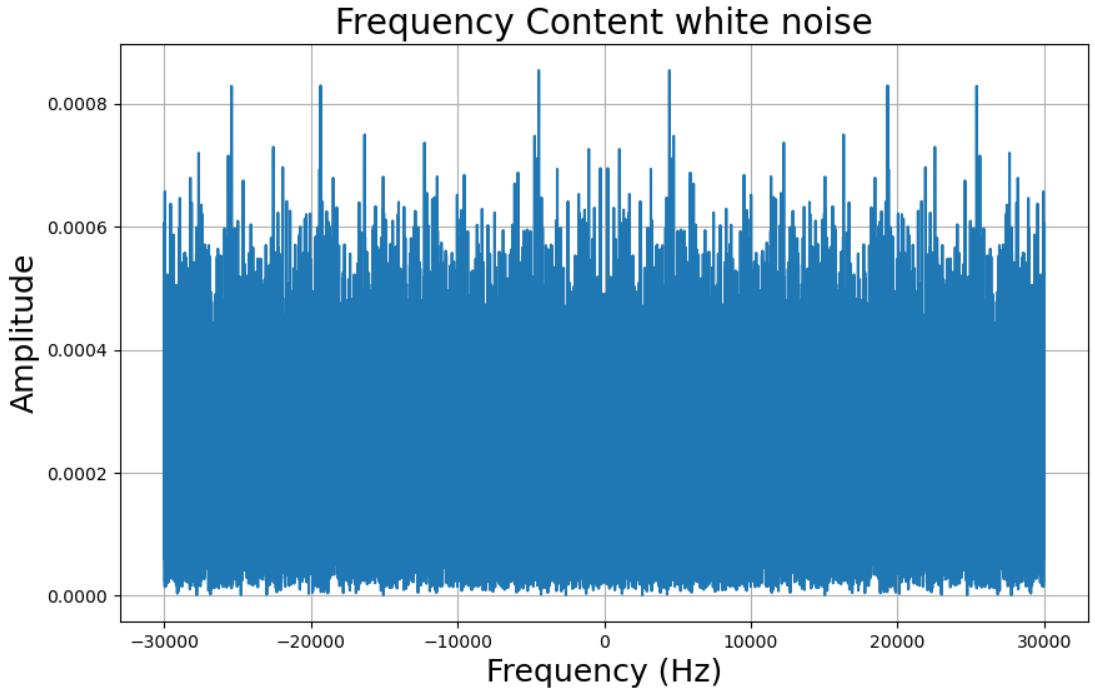

Figure 5.6. Frequency domain representation of the white noise signal.

With this algorithm, different noise types can be created. However, the case of frequency-specific noise requires a different approach.

Frequency specific noise generation

To model noise spikes on specific frequencies, a white noise signal is generated using the algorithm used to create colored noise. The white noise signal is then passed through a bandpass Butterworth filter with cutoff frequencies that fit the specifics of the signal. Figure 5.7, illustrates a Fourier-transform of a frequency-specific noise in the range from 5000 to 10000 Hz.

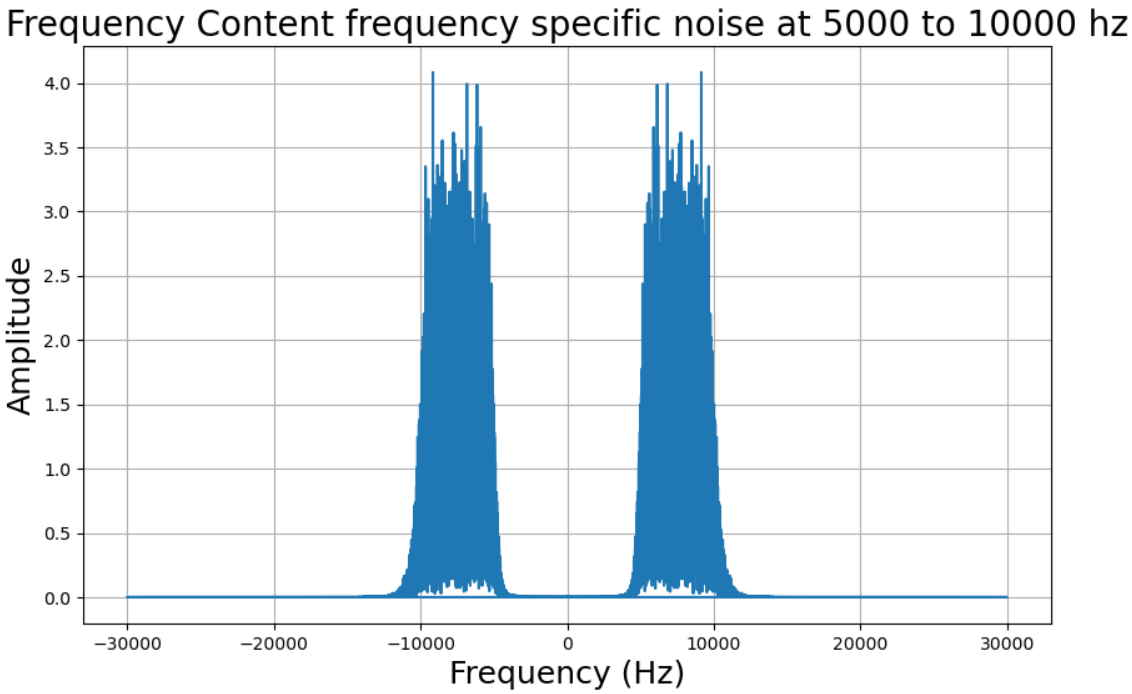

Figure 5.7. Frequency domain representation of the noise signal with frequency-specific noise between 5000 and 10000 hertz.

This approach is not necessarily efficient in giving a perfect cutoff, but the overflow into other frequencies is accepted in this simulation.
This overflow can, however, be treated as a source of error for some purposes.

Hall sensor

The noise of the Hall sensor is based on the noise components in the frequency domain normally present in a Hall sensor measurement.[22] [23]
The Hall sensors give absolute measurements of the magnetic field and, thereby, do not have the same integration errors as the fluxmeter. The Hall sensor usually still integrates over some time period of measurements, but the integration is over a set number of samples, and thereby, it becomes an average of the number of measurements taken in the time interval. The noise profile usually has some pink noise and a noise component at higher frequencies, in this simulation it is approximated in the range from 6.000 to 10.000 hertz. The noise in the simulation is then modelled with a pink noise component and plus frequency-specific noise component from 6.000 to 10.000 hertz.

The sampling of the signal is done over very short periods where the signal is averaged over the samples taken between two different timesteps defined by the sampling frequency.

Fluxmeter

The sampling noise of the fluxmeter is based on the spectral analysis from the section 3.2.2. The content of the fluxmeter signal is modelled as a combination of a derivative of the underlying signal and the noise components seen in the measurements taken for noise analysis.
The noise components can be seen as a white noise component integrated as a drift noise when integrating the signal. The drift noise can be modelled in multiple ways, one is to create a coloured noise component and add it directly to the sample, and the other is to add white and pink noise components and then integrate the derivative of the signal.
Integrating the derivative with the signal when reconstructing the measurement gives the most realistic representation of the effects where the frequency response of the noise also changes with the sampling frequency due to the integration functioning as a low pass filter.

5.2 Filter tests and performance evaluations

To evaluate the developed methods in the created simulation environment, different scenarios are set up and run with different parameters. Both filters are tuned with cutoff frequencies that perform the best overall through multiple iterations for the best comparison.

5.2.1 Kalman filter using Hall sensor and fluxmeter

A study of this case is important to show that the drift can be corrected and improved in coils with noise profiles similar to the noise occurring in the coils of the fluxmeter. A plot of the Hall sensor signal, the fluxmeter signal, and the Kalman filter signal can be seen in Figure 5.8, where it can be seen that all signals follow the artificial field very well.

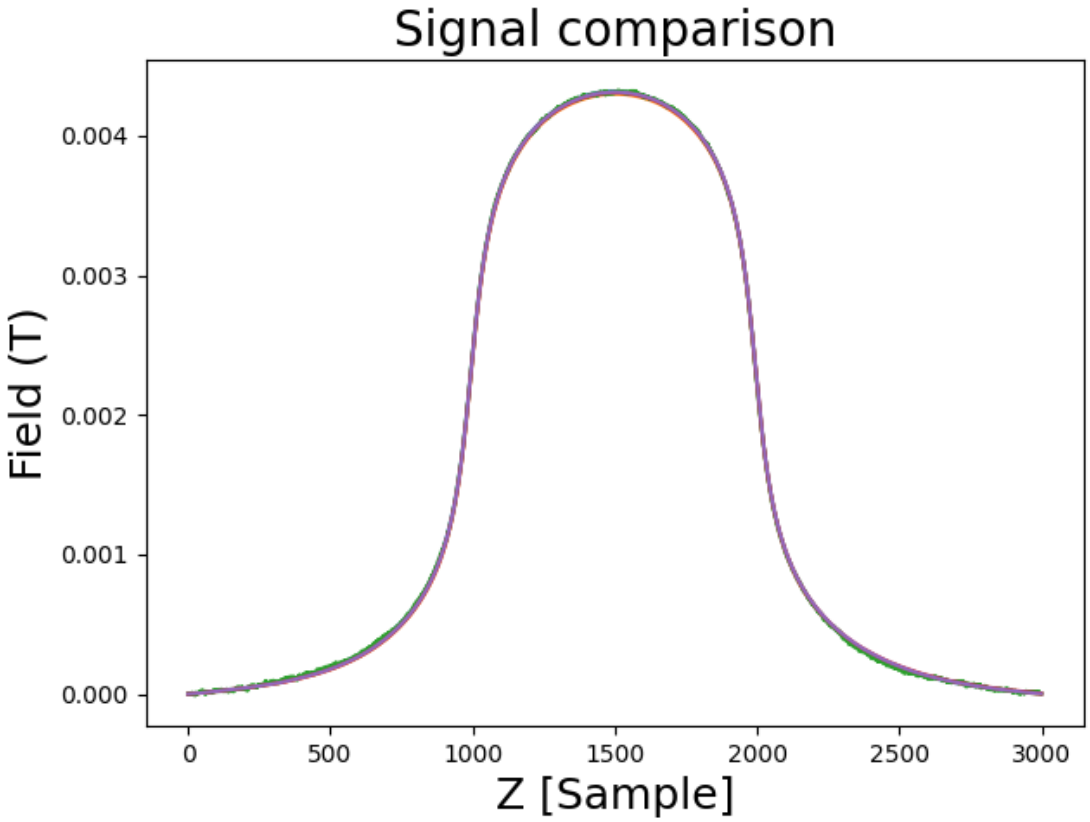

Figure 5.8. A plot of the signal generated with the simulation, the signals generated by the sensor simulations, and the Kalman filtered signal.

To evaluate the performance of the different sensors, the residuals are calculated alongside the root mean square error from the underlying true signal. In Figure 5.9, the residual plot shows that the high-frequent noise of the Hall sensor is the main challenge for measurement quality. The voltages over the fluxmeter coils are measured using the fast digital integrator system, and the measurement data are then integrated to generate the magnetic flux. This double integration gives a filtering effect that leaves the low frequencies in the signal. Therefore, the fluxmeter does not have the same problem with high-frequency noise but can float away from the actual value due to a bias in the voltage signal. To estimate the bias and make the measurement center around the underlying signal, the mean of the voltage signal is subtracted before integrating the measurement to a magnetic flux. This creates a measurement as seen in Figure 5.10 where the error drifts away from zero but returns at the end of the signal.

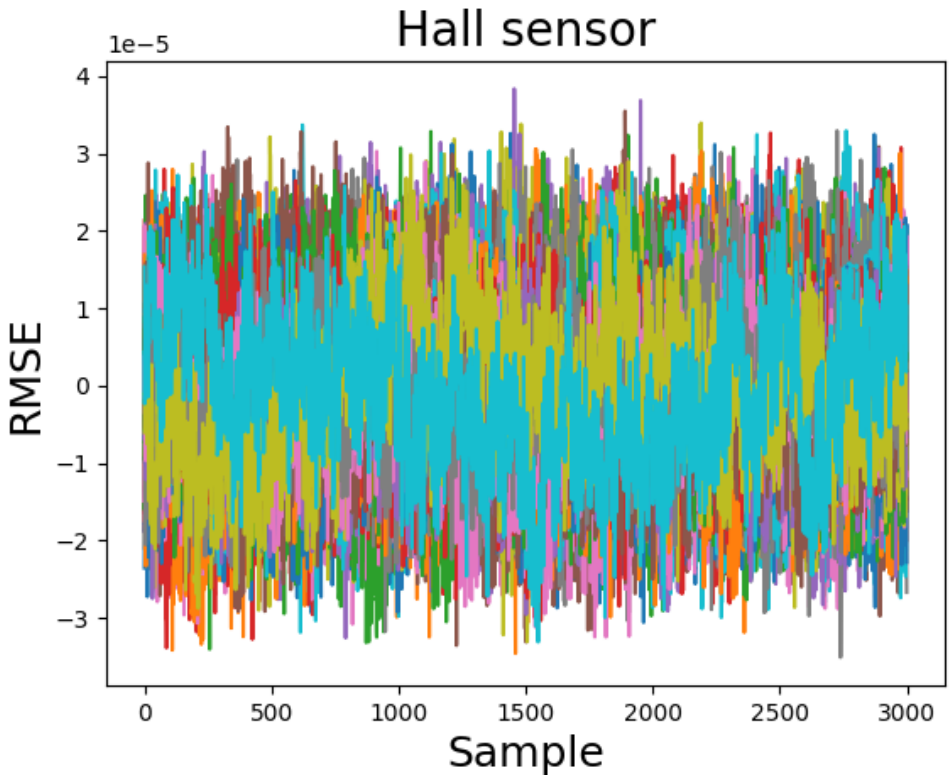

Figure 5.9. A figure displaying the error of the Hall sensor from the underlying ground truth.

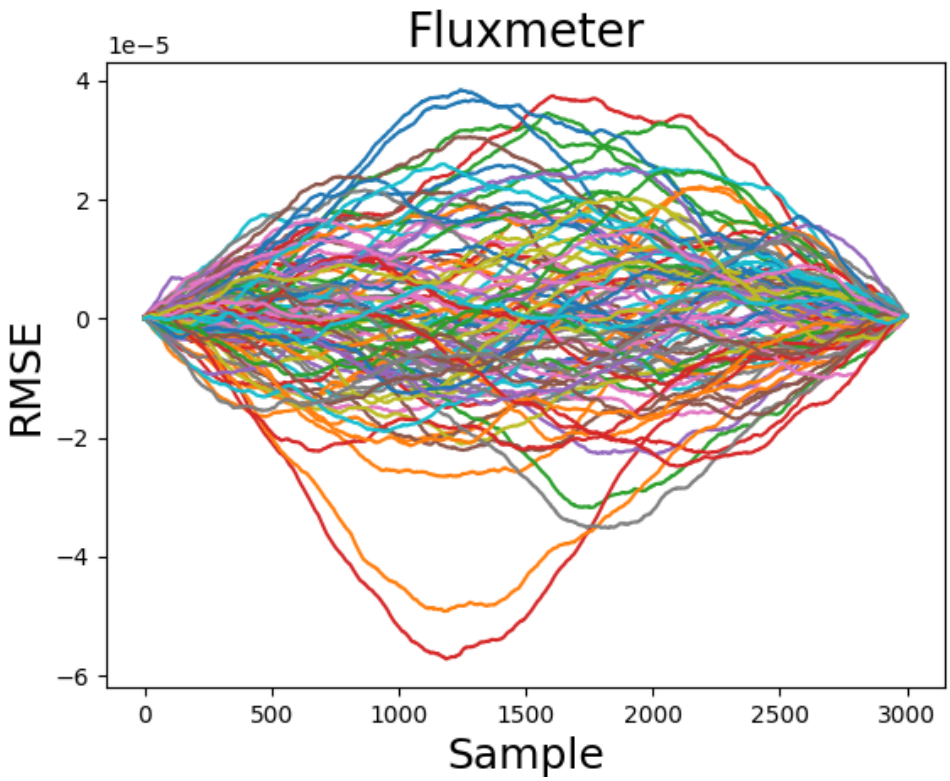

Figure 5.10. A figure displaying the error of the translating fluxmeter signal from the underlying ground truth.

The fused signal using the sensor shows a slight improvement of the drift by tracking the bias at the current sample and estimating the low-frequent noise in the signal. The ensemble simulations' root mean square error for the two filters can be seen in Figure 5.11 and Figure 5.12. The Kalman filter signal is generated using the Hall sensor and fluxmeter signals from Figure 5.9 and Figure 5.10. The mean of the root mean square error of the filters over all 100 simulations is slightly lower than any of the two sensor measurements.

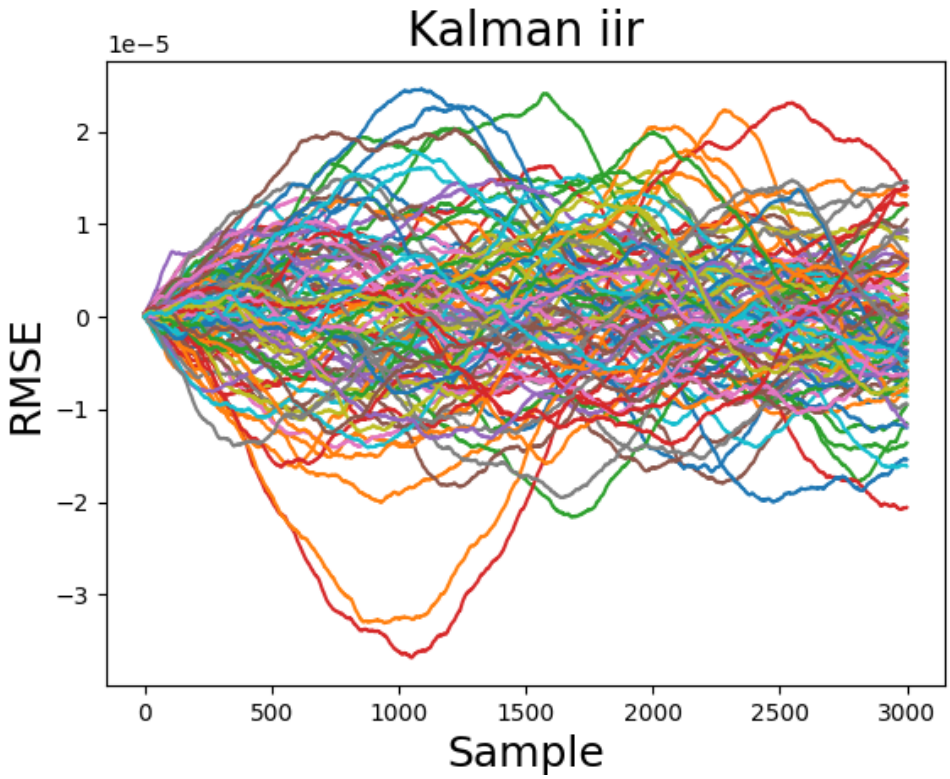

Figure 5.11. A figure displaying the error of the Kalman filter from the underlying ground truth.

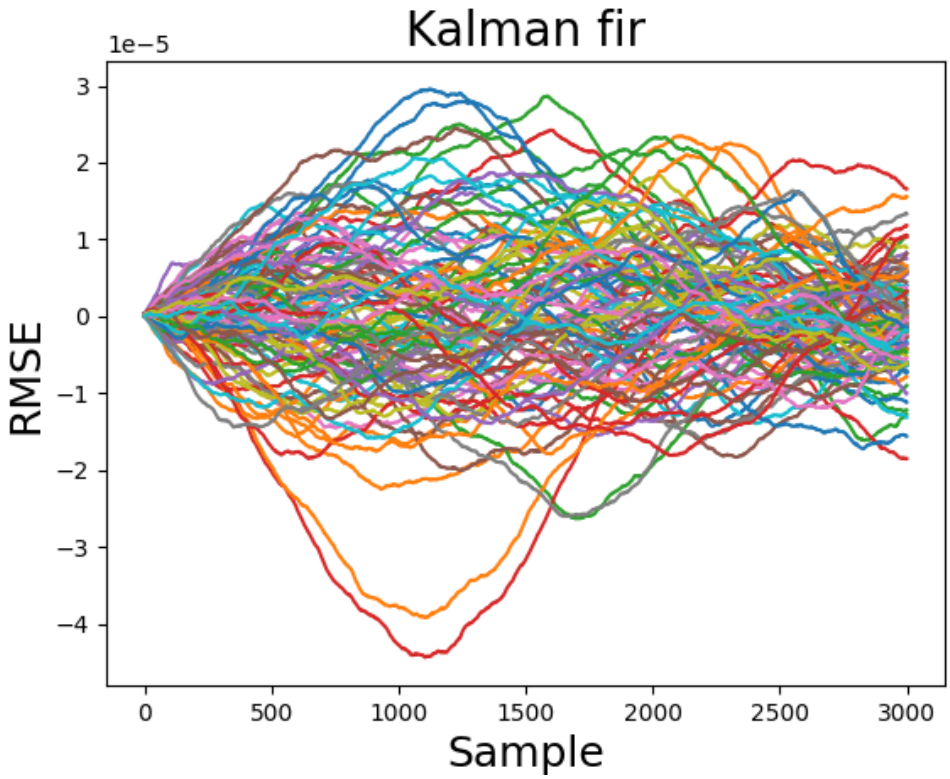

Figure 5.12. A figure displaying the error of the Kalman filter from the underlying ground truth.

The results show that the Kalman filter with the Chebyshev filter is best at adjusting to significantly changing bias throughout the measurement and delivers a continuously better mean squared error between the signal and the estimated field throughout multiple simulations. The average root mean squared error of the series of 100 simulations can be seen in table 5.2, which also shows that while both Kalman filters help create a better signal, the filter using the Chebyshev filter to filter the bias is generally better.

kalman infinite-impulse-response	6.494e-06
kalman infinite-impulse-response	5.717e-06
Hallsensor	6.776e-06
Fluxmeter	8.075e-06

Table 5.2. Root mean square error average over an ensemble analysis

Having tested filter performance in simulation and determined that the infinite-impulse-response Kalman filter is the most effective for correcting drifting measurements a performance analysis on real data can be performed.
The following section will describe the performance comparison against a linear Kalman filter used on a reference dipole.

5.2.2 Comparison of filter performance

To evaluate the performance of the filter on a real fluxmeter measurement, it is implemented on a real dataset taken for a paper on Kalman filtering between a fluxmeter and a Hall sensor[24]. The data is collected with a small fluxmeter and a Hall sensor tested with ramped signals in a reference dipole with a field strength of one Tesla. The magnet is ramped from zero to 1 Tesla through multiple iterations while the fluxmeter and the Hall sensor are both placed in the magnet.

The original goal of the paper was to investigate the effects of a classic linear Kalman filter on a fluxmeter measurement. The conclusion is an improvement in the signal with a significantly lower measurement variance compared to the fluxmeter and Hall sensor.
The bias estimating filter was implemented with a cutoff frequency of 0.001 Hz. The results of the filtering are shown in Figure 5.13 and Figure 5.14, where the peaks of the signal are isolated to get a clearer indication of the signals separately.

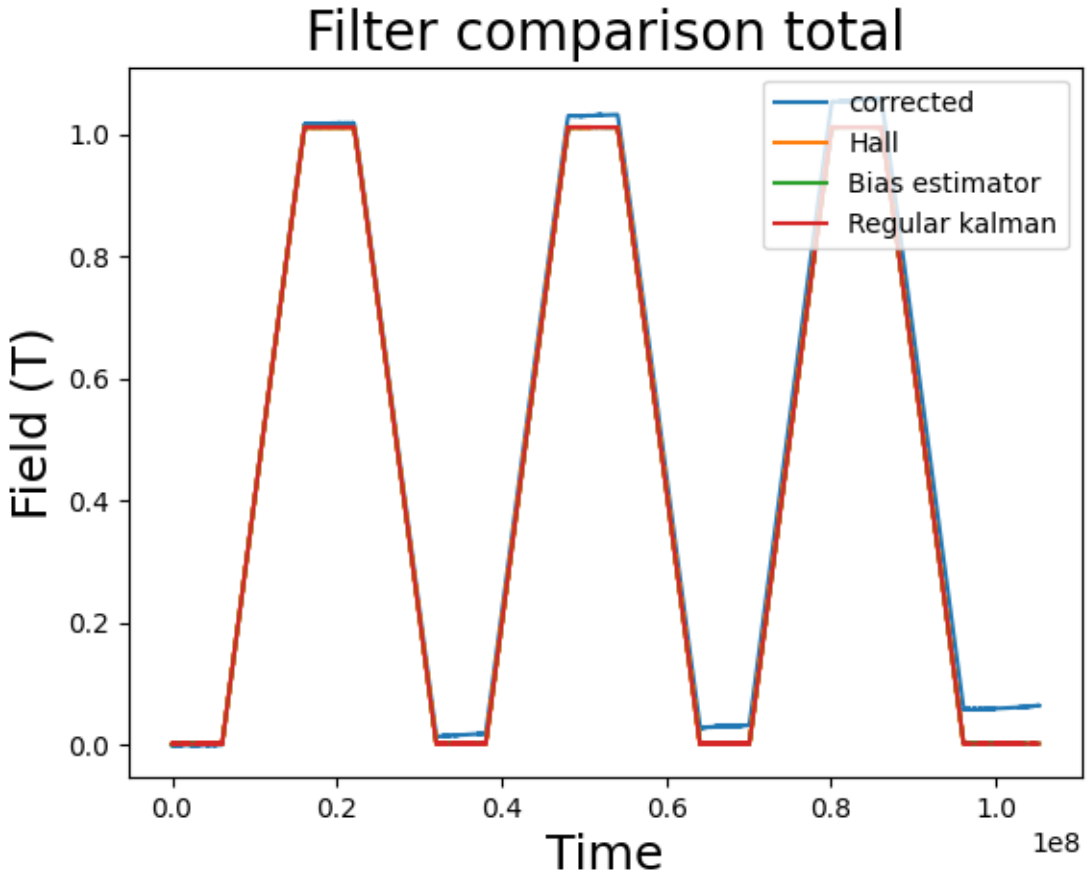

Figure 5.13. The full ramp signal used for the study of the linear and frequency bias tracking filter.

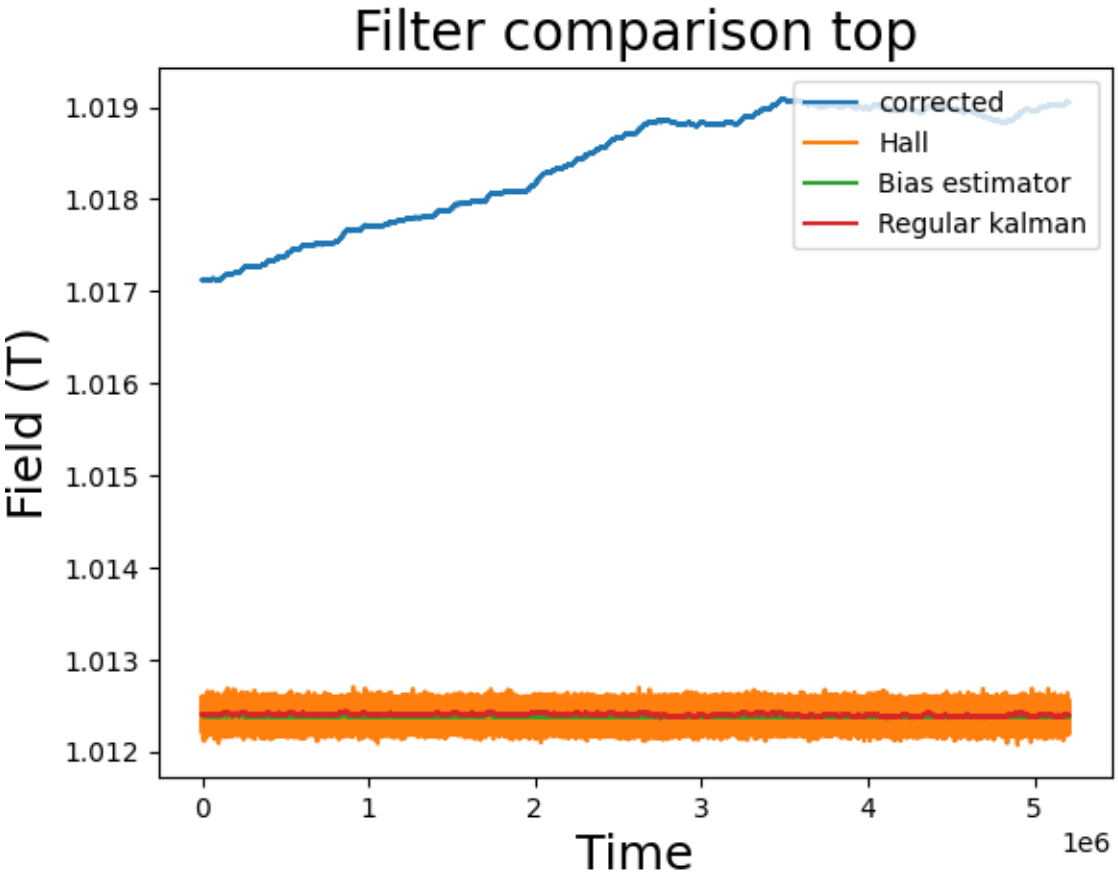

Figure 5.14. The top of the ramp used for comparing the linear Kalman filter with the bias frequency tracking filter.

With a variance of 5.70E-11 the new bias estimating Kalman filter has a lower variance than the general linear Kalman filter. The data from the acquisitions is displayed in table 5.3. The data displayed is the average of all tops and bottoms of the ramps where the current is stable. The deviation from the Hall mean is also presented as the Hall sensor mean value over more than 100.000 samples on a flat part of the ramp is considered relatively stable. The deviation from the mean of the samples of the Hall sensor on the flat tops is used as an accuracy measure since the Hall sensor, while having a relatively large variance, over more than 100.000 samples provides a somehow accurate estimate of the field strength.

Measurement	Variance	Deviation from Hall mean
Hall sensor	2.60891671e-09	0
Linear Kalman filter	1.08E-10	1.36E-05
Bias estimation Kalman filter	5.70E-11	9.63E-07

Table 5.3. Table of the variance and deviation from the Hall mean for the two Kalman filter types and the Hall sensor.

The numbers show that in situations where the coil's drift can cause a problem, the Kalman filter can increase the quality of the measurement. Whether or not it is necessary to implement the filter tracking the bias or whether it is sufficient with a linear Kalman filter will depend on

the noise in the sensors and the measurement requirements.

5.3 Filter for fluxmeter data

To test the filter using multiple signals from the same disc, an experiment using the fitting of the Bessel-Fourier-Fourier series and then using the model from the bigger coils to correct the smaller coils on the disc will be used. The variance of the signal will be compared to the variance of the signal of an acquisition without signal processing applied to numerically investigate the effects.

5.3.1 Data acquisition

The data acquisition used is a scan of D5, Q520, Q522, and D0. The selection of coils is to test the algorithm on different layers and on the same layer on the disc, which means that two tests will be performed. One is the test of the D5-D4 coil signal to correct the D0 signal, and the other is to use the Q520 and Q540 to correct the Q522 and Q542 coils.

5.3.2 Modelling measured data

The measured data is modelled using the Laplace solution from section 3.1.1. One approach for fitting the Bessel-Fourier-Fourier series solution to the is fitting an actual measurement to a specified number of terms in the bessel-fourier series expansion that is the solution to the Laplacian of the cylindrical coordinates. Since the sensor is the most sensitive to the B_z component of the field the attempt to fit will be done to this particular field component using a D5 coil.
To find the coefficients in Equation 3.16 that describes the solenoid magnetic field and an understanding of how the measurement corresponds to the field.
The change of field through the surface of the disc means that a surface integral for the entire disc is necessary, and thereby, it is not enough to fit a series that fits the radius of the disc. To solve this issue, an extra sum is added to Equation 3.20.

$$B_z(D_i, z) = \sum_{r=0}^{r_{D_i}} W_r \sum_{n=0}^{\infty} I_0(\lambda_n r)\left[\mathfrak{F}_n \cos(\lambda_n z) - \mathfrak{G}_n \sin(\lambda_n z)\right] \tag{5.4}$$

W_r	A weight scaling the contributions from the different radius.
D_i	The disc coil for which the measurement is modelled.

The coefficient W_r is needed since each radius does not contribute equally to the surface of the disc and therefore it is calculated as.

$$W_r = r_n^2\pi - r_{n-1}^2\pi \tag{5.5}$$

The greatest challenge is solving the integral quickly and efficiently since the quality of the surface integral fitting depends on the number of samples taken in the approximated surface integral. It is obvious from the summation of radius terms scaling the different field strengths at different radii that the resolution of r, increases the quality of the model. However, increasing the resolution of r also increases the computation time.

Fitting a measurement of the solenoid magnet taken with the D5 coil using a least squares function results in the field maps in Figure 5.15 and Figure 5.16.

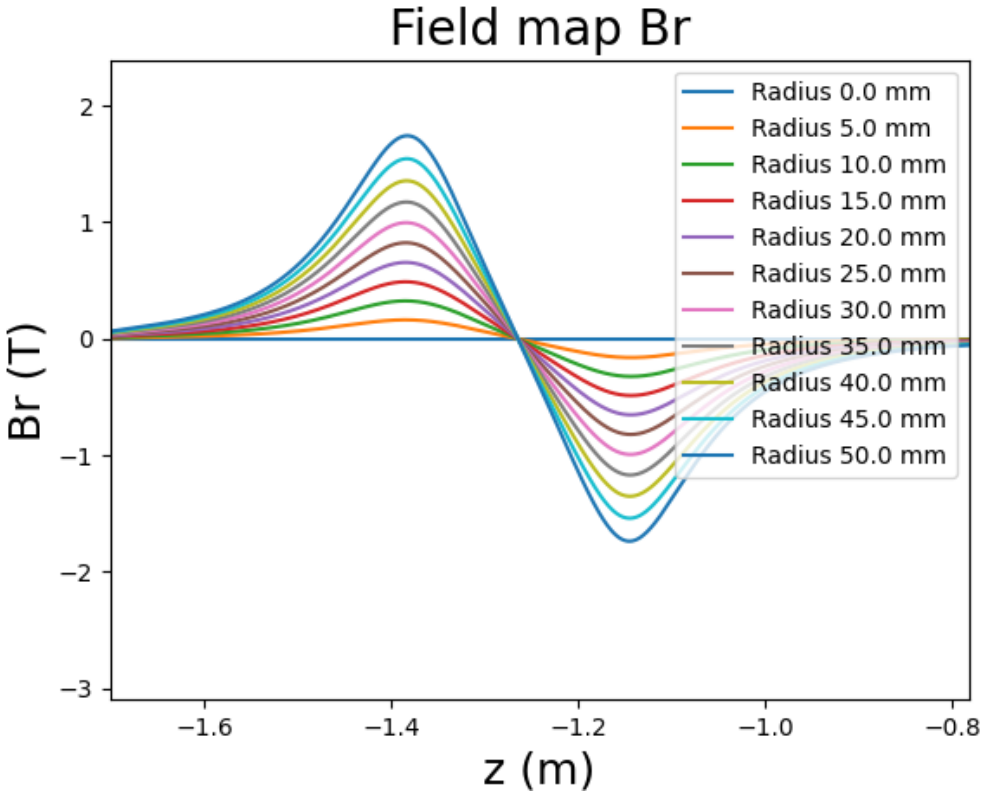

Figure 5.15. The B_r field extrapolated to different radii using a model of 30 coefficients fitted to a D5 coil measurement.

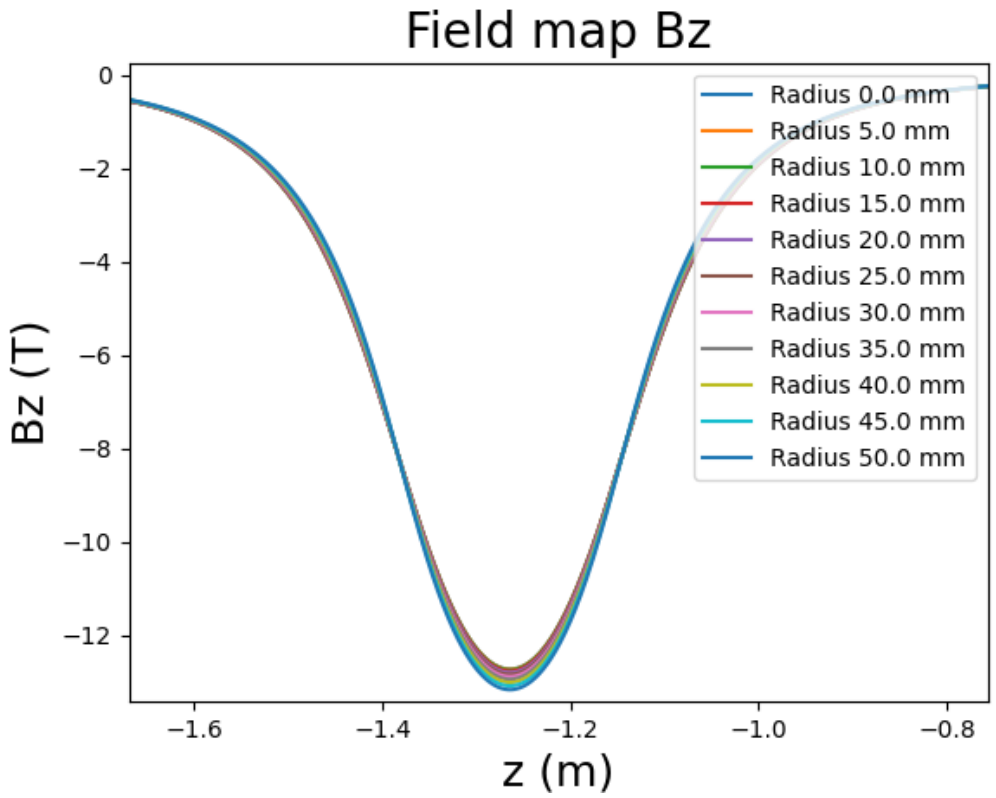

Figure 5.16. The B_z field extrapolated to different radii using a model of 30 coefficients fitted to a D5 coil measurement.

With coefficients of significance distributed as seen in Figure 5.17 and 5.18, which shows that the significance of each term drops after the 22^{th} term if fitted with 30 terms.

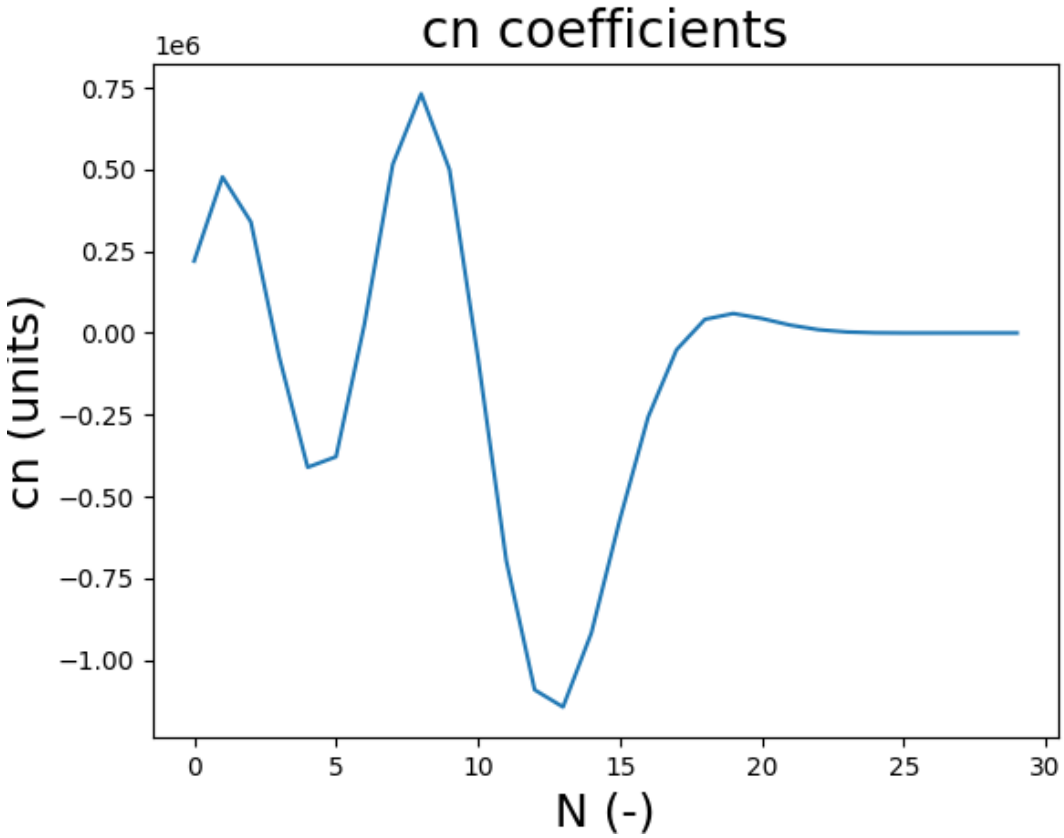

Figure 5.17. C_n coefficients of a series fitted to a D5 measurement.

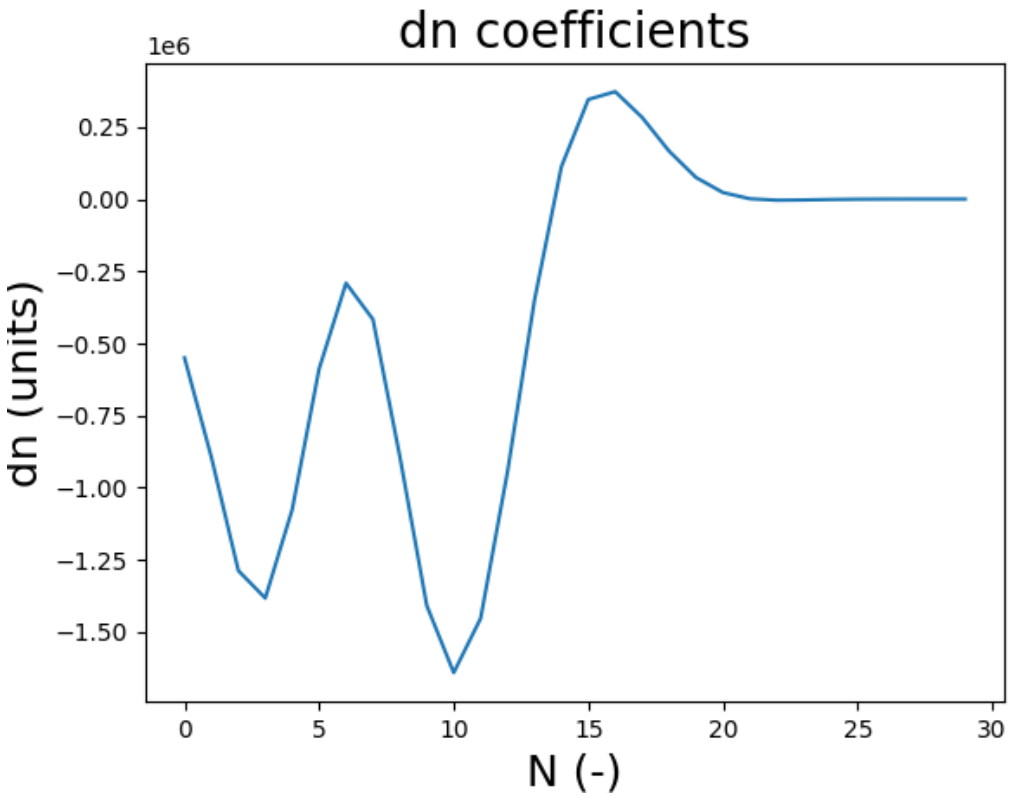

Figure 5.18. D_n coefficients of a series fitted to a D5 measurement.

The error in the fitting to the D5 coil measured against the actual measurement of the coil is presented in Figure 5.19.

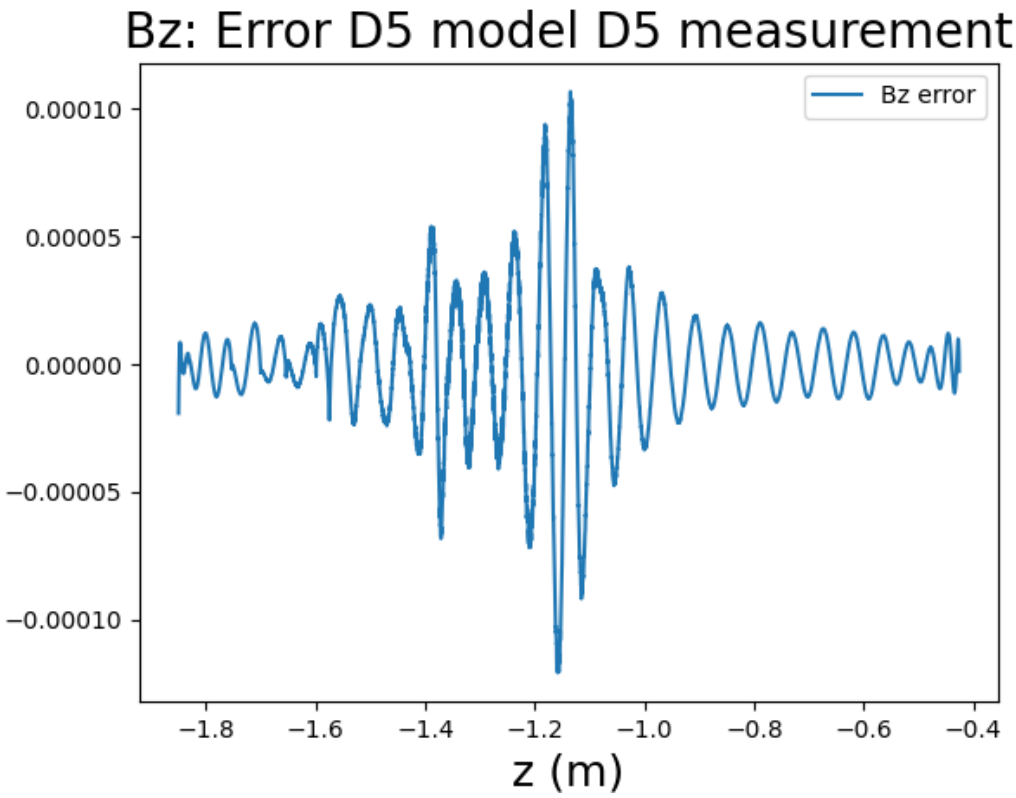

Figure 5.19. The error between the measured field on the D5 coil and the actual D5 measurement.

An issue with the fitting approach is that the field does not seem to scale well inside the magnet, which can be seen on the error plot shown in Figure 5.20 and in the field to model comparison in Figure 5.21 where the D4 coil measurement is estimated from a model of the D5 field. However, from the shape of the error, it can be inferred that the model underestimates the field as a function of radius but not necessarily the shape of the field.

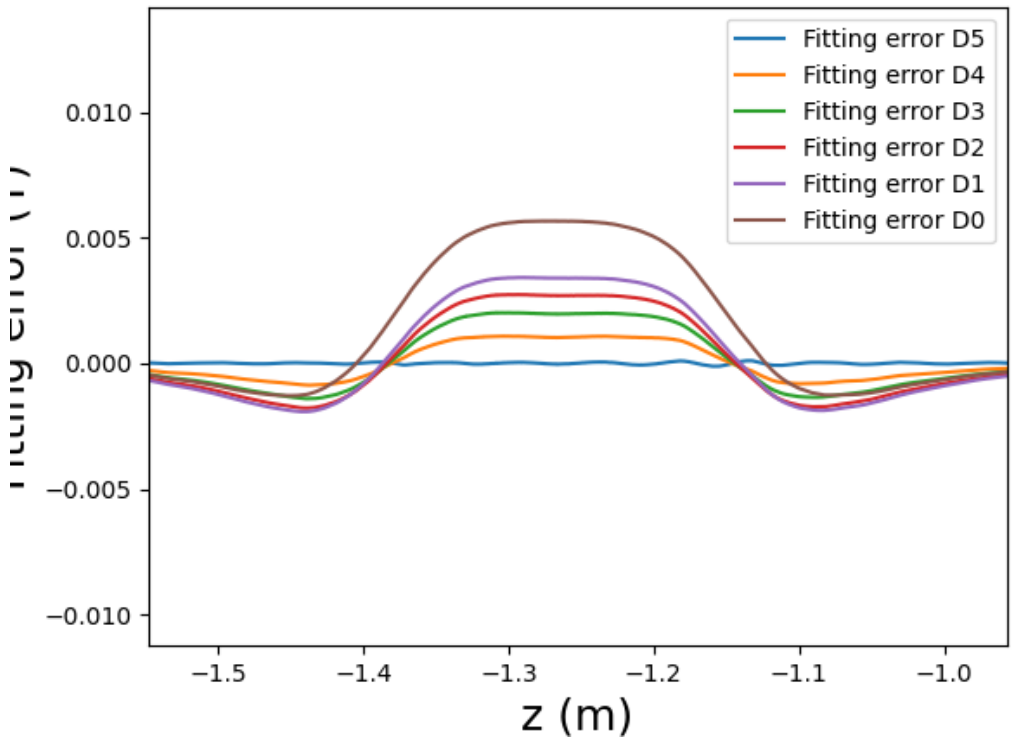

Figure 5.20. Fitting error between a model fitted to the D5 coil compared to the other disc coils in the same acquisition.

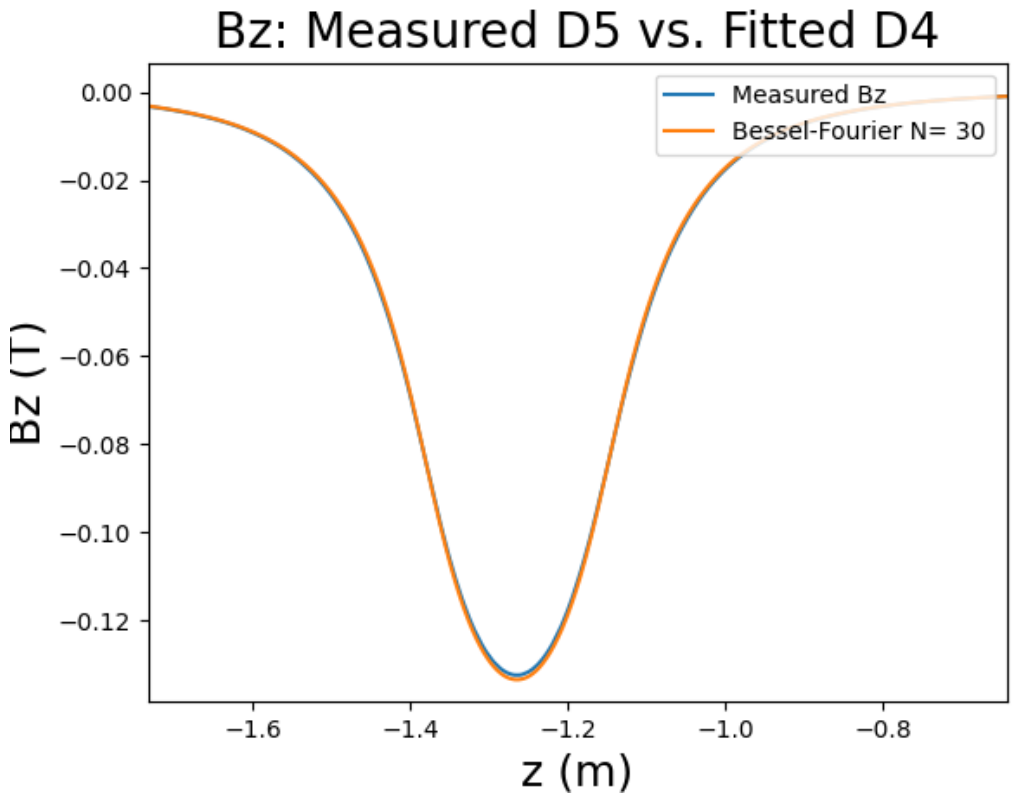

Figure 5.21. The B_z field of a D4 coil is estimated with a model fitted to a D5 measurement, and an actual measurement of a D4 coil.

The estimated error can originate from the discrete integration or other numerical results as well as the simplification made when assuming that $B_\varphi = 0$. Attempting to accommodate the discrepancy of the model by fitting the radii of the coil to the model parameters gives a model with a better prediction of the field.

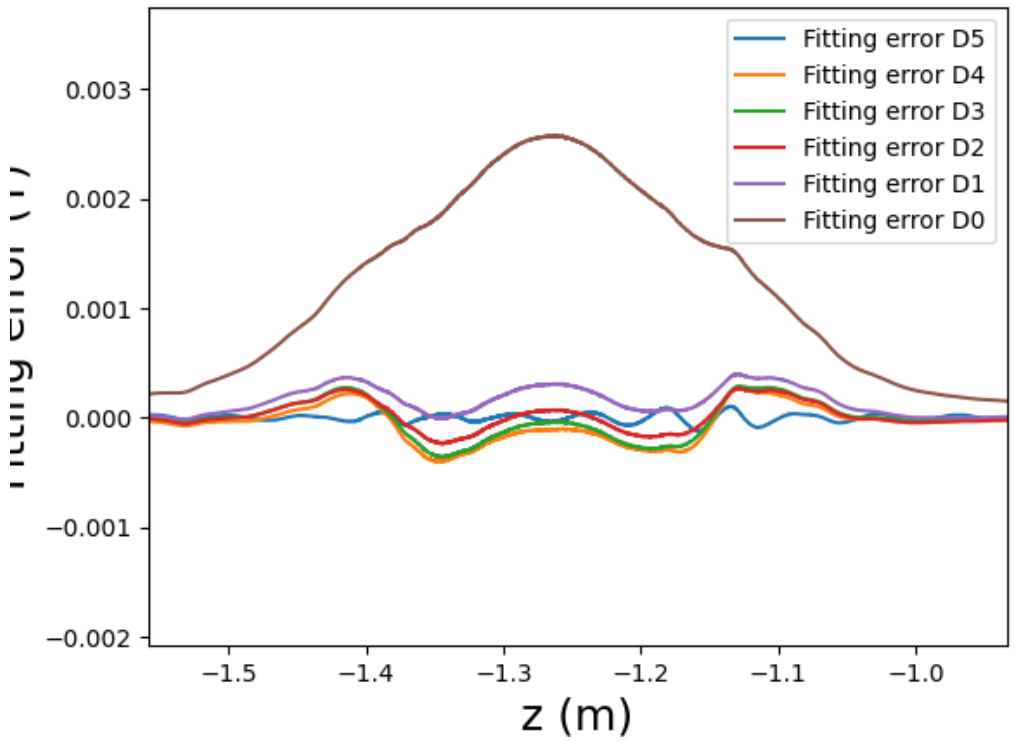

Figure 5.22. Fitting error between a model fitted to the D5 coil compared to the other disc coils in the same acquisition. Using the wrong radii for the coil widths.

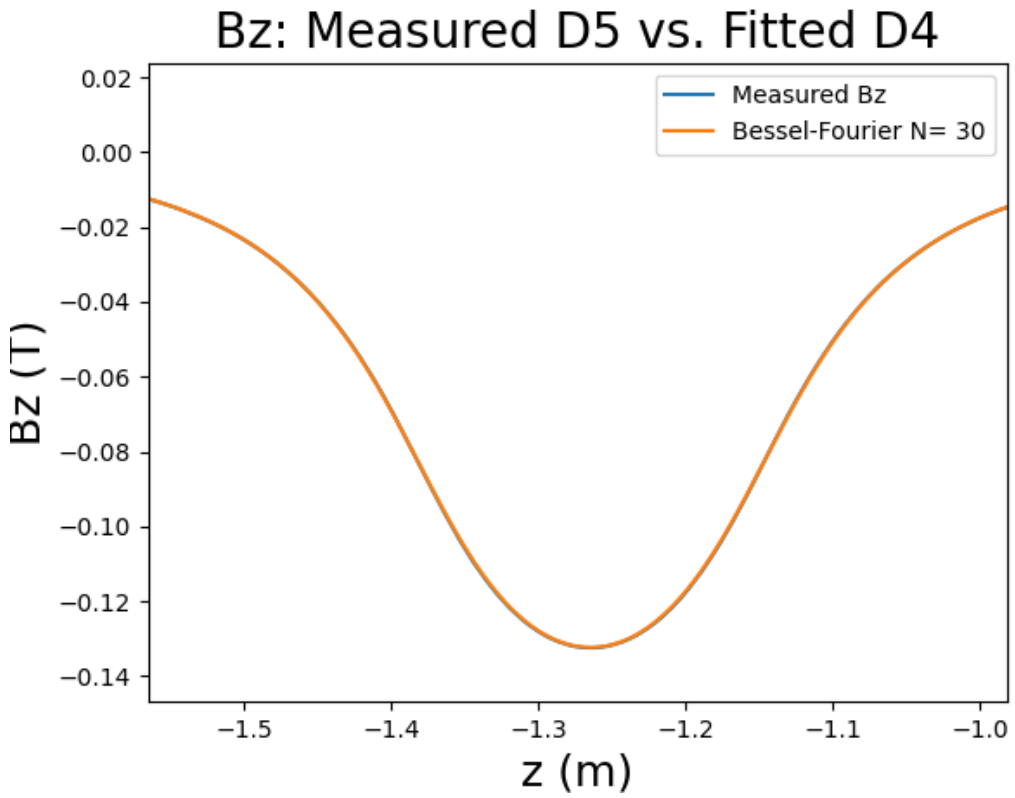

Figure 5.23. The B_z field of a D4 coil is estimated with a model fitted to a D5 measurement and an actual measurement of a D4 coil. Using the wrong radii for the coil widths.

In Figure 5.22 and Figure 5.23 a correction to the radii of the measurements has been made. This, of course, makes the model unable to directly correspond to reality, but it produces a good reference field.
While some improvements to the model might make it contain even more information about the magnet, the reference models will be used to attempt to filter the D0 coil using a field derived from D5 measurements.

5.3.3 Test description

This subsection contains a short description of the test and the expected outcome.

Q520 and 522

The target outcome of this experiment is to test the use of Kalman filtering on smaller coils using larger coils surfacing the same average radial distance from the center. The choice of coils to use is determined by the fact that the radial field changes as the radius of the coil changes, and therefore, the measured field will have different shapes depending on the radius from the center on which it is measured. The Q520 and Q522 coils have a center around the same radius and, therefore, might share some characteristics when it comes to field shape. Both are also placed on the same quadrant, which means that they might share some information about the field. The

measurement's bias estimate is also tracked since systematic outliers in this variable can show some key differences in the two signals that might need to be considered.

D5 and D0

To test the usage of the solenoid model for drift correction through filtering a Kalman filter is applied to the D0 coil using a model derived from the D5 coil from the same measurement. The test is repeated 11 times and the variance of the coils is compared to see if any improvements in the D0 coil measurements can be seen.
The bias estimate of the measurement is tracked in this test as well.

5.3.4 Results

In this subsection, the results of the measurements will be presented and discussed shortly.

Q520 and 522

The filtered signal between the Q520 and the Q522 coil, filtered with the bias-tracking infinite-impulse-response Kalman filter, should optimally have a lower variance than the Q522 coil and keep some of the characteristics from the specific shape.

A general overview of the mean of the Kalman filtered signal plotted with the means of the raw acquisitions from Q520 and Q522 in Figure 5.24 shows that the signals are very much alike at first glance.

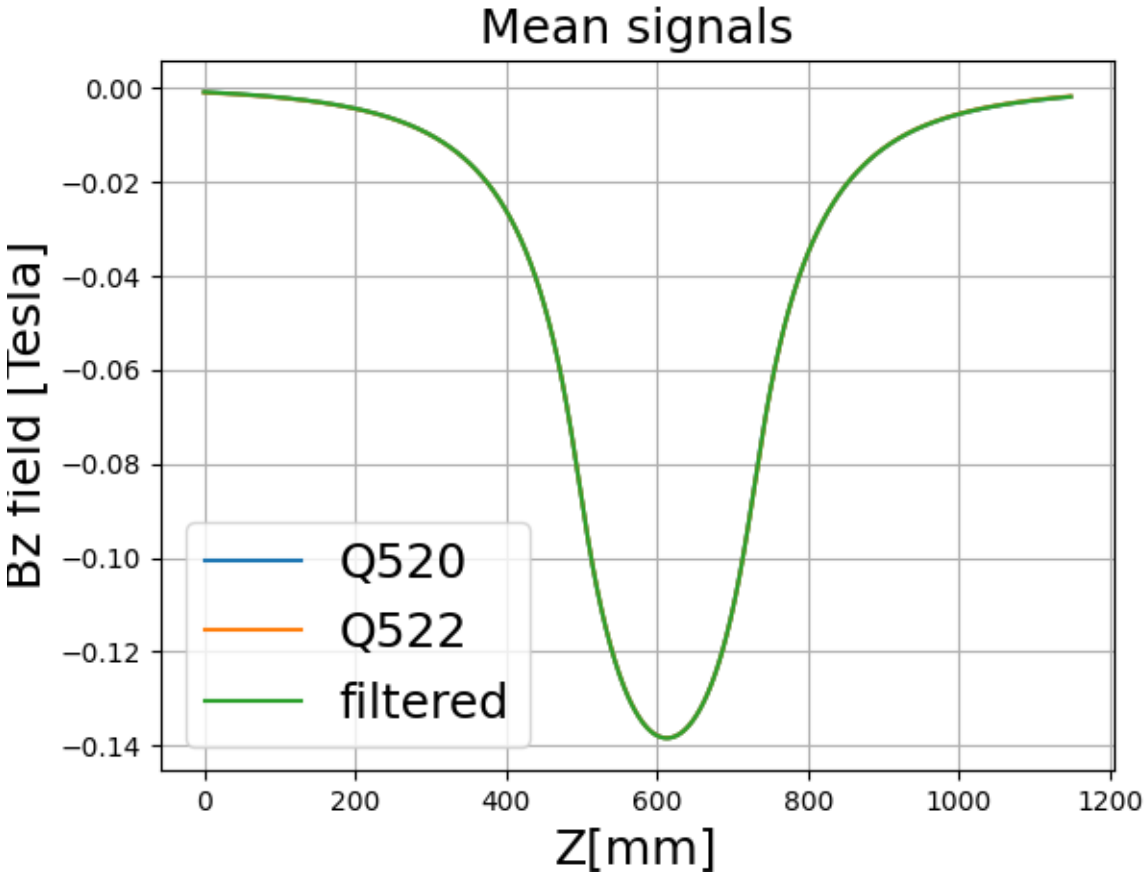

Figure 5.24. A plot of the two measurements taken with the Q520 and Q522, and the fused signal made from Kalman filtering.

The variance of the three signals seen in Figure 5.25 also shows that the variance of the Kalman-filtered signal is generally lower than that of the Q522 coil.

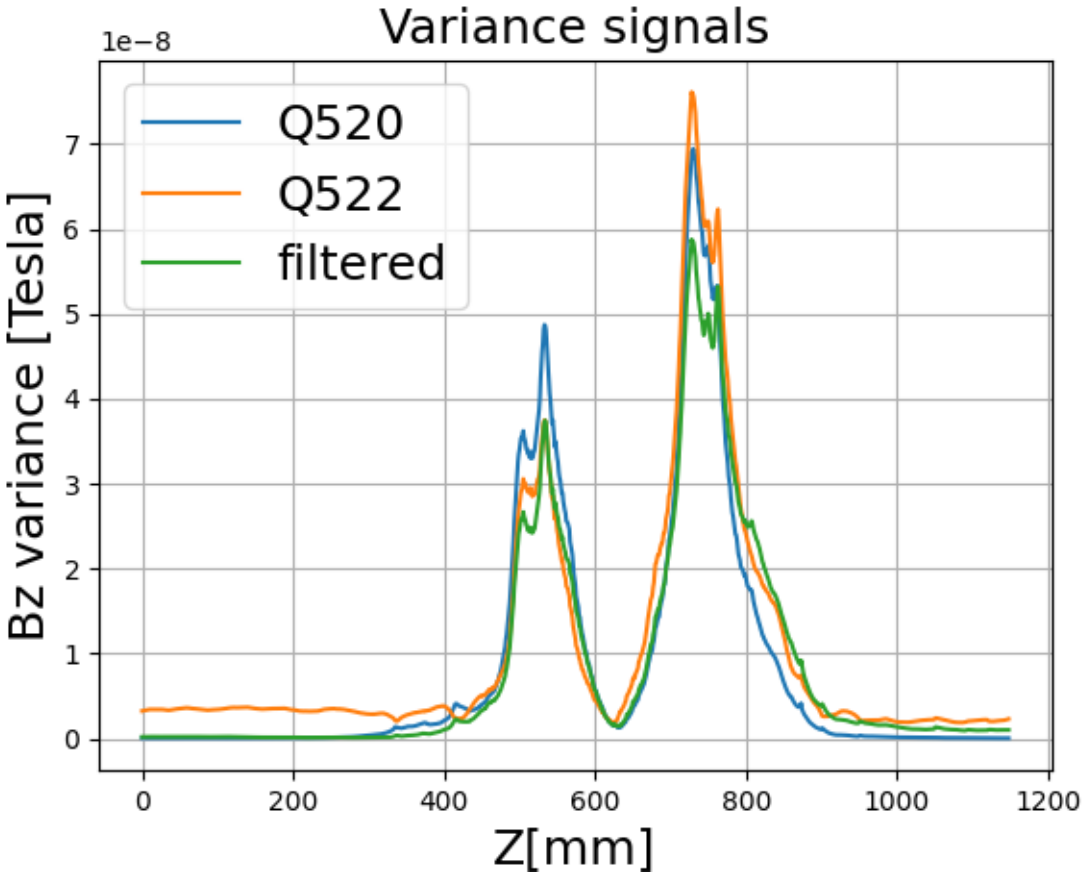

Figure 5.25. The variance of the two measurements taken with the Q520 and Q522, and the fused signal made from Kalman filtering.

There are different ways to test whether or not some of the signal's characteristics are removed by filtering. One of these ways can be to investigate the bias signal subtracted from the incremental measurement at each step. Figure 5.26 presents a plot of the bias estimated at each sample taken.

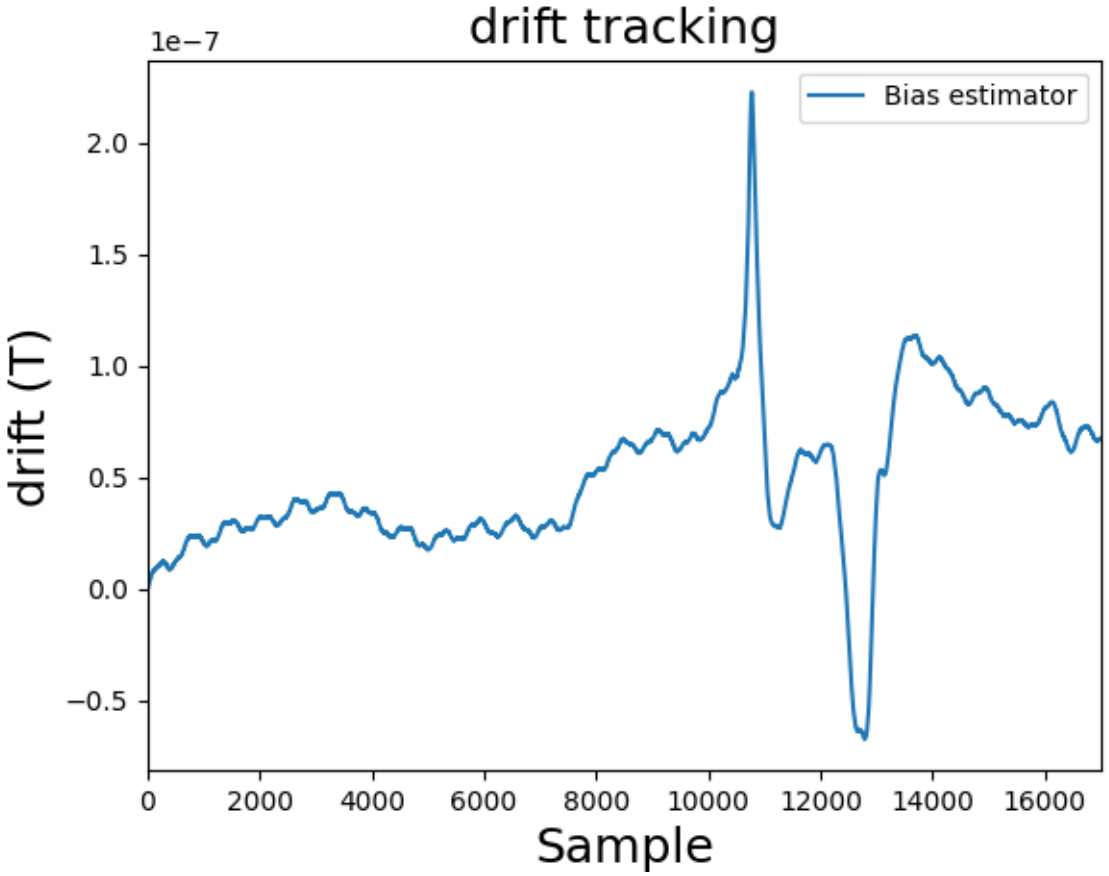

Figure 5.26. The drift estimated in the measurement of a Q522 coil.

In Figure 5.26 it becomes apparent that the error between the coils used to estimate the drift is large at two points different intervals. Relating these intervals to the B_z field gives a clear indication that the intervals are the fringe fields of the magnet, as seen in Figure 5.27.

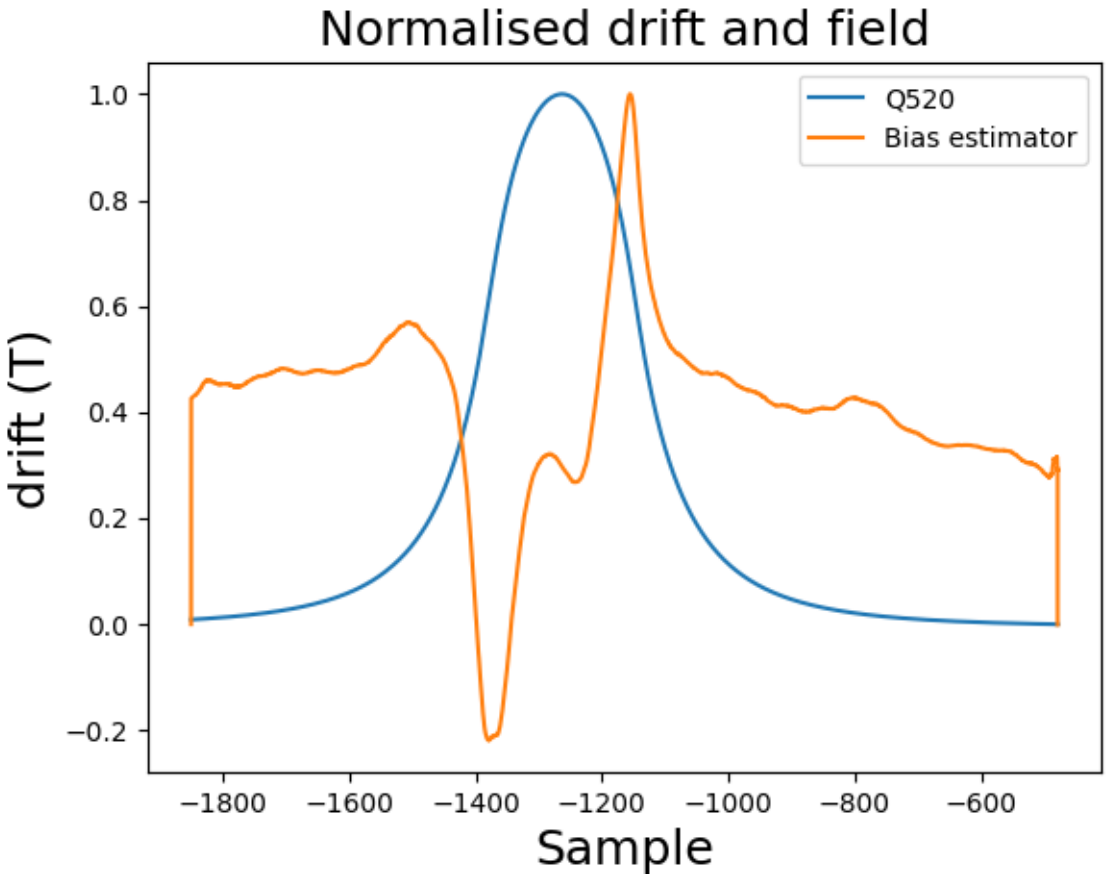

Figure 5.27. A plot of the normalised drift and field from a filtered acquisition of the Q522 coil.

The difference in the ends of the magnet can indicate that some information might be lost when filtering the smaller coils. However, as seen in the change in variance, the acquisition drift is reduced. The loss of information might, however, make the coils' raw filtering unsuitable for measuring high-precision systems.

D5 and D0

To filter the D0 coil signals, 11 measurements were performed with the D5 and D0 coils. The variance between the coils can be seen in Figure 5.28, where the scan is taken to the opposite direction of the z-axis. It is visible in the figure that the drift of the signal is more significant for the D0 coils than for the D5 coils.

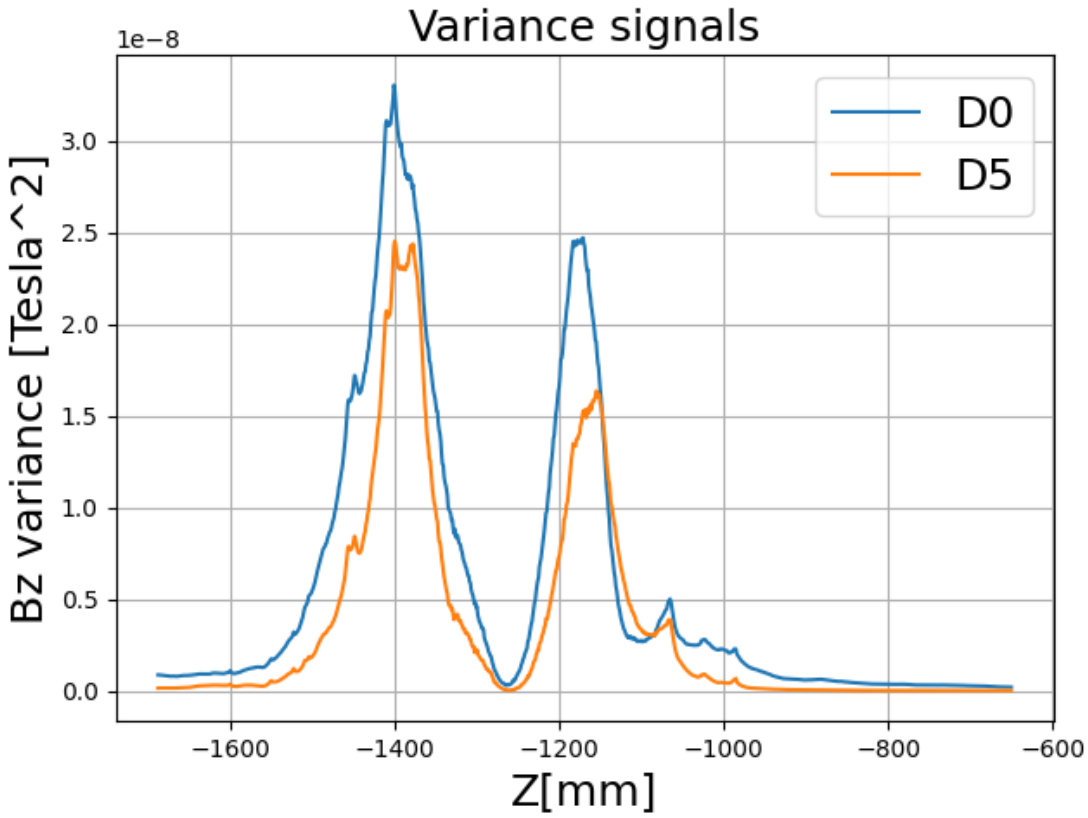

Figure 5.28. A comparison of the variance between the D5 and the D0 coil measurements.

The filtered signal is produced by using the D5 coil to fit a model and then taking the acquisitions of the ΔB_z measured with the D0 coil in the filter with the model derived of the D0 field as an absolute measurement to estimate the bias. The variances of the signals can be seen in Figure 5.29 together with the variances of the D5 and D0 coils.

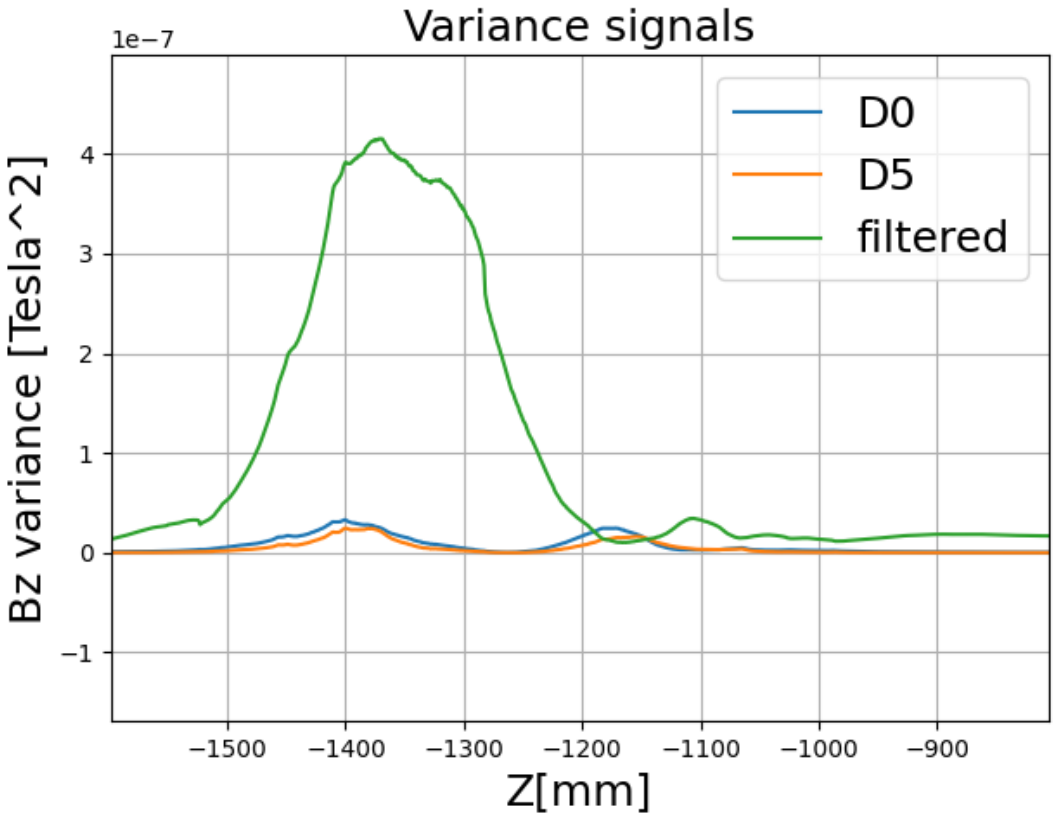

Figure 5.29. A comparison of the variance between the D5 and the D0 coil measurements.

The figure shows that the variance is bigger than that of both coil measurements, which can indicate an even larger error than the original measurement. Reasons for this worsening of the signal can possibly be attributed to errors in the model of the field, which can also be seen in Figure 5.22 where the fit to the D0 coil is also worse than that of the other coils. This assumption can indicate that better fits of the field, especially ones that scale well when extrapolating to the center of the disc are needed.

In the next chapter, the results of the tests and measurements, combined with the knowledge gained, will be discussed. This discussion will be followed by a conclusion to the effort in magnetic measurement filtering explored in this report.

Discussion 6

The discussion of the reports of this thesis is centered around three different topics:

- The application of noise analysis.
- The necessity of filtering in the final project.
- Future work.

Each topic cannot be discussed without additionally touching on one or both of the others. This dependency might become even more obvious throughout the discussion, but for the sake of clarity, some separation will be kept in the structure.

The application of noise analysis

An initial investigation of the properties of the signals measured with the translating fluxmeter 2.0 involved conducting a noise analysis. The noise patterns were used to identify some spectral properties of the noise that could affect the signal negatively. While the noise level tolerances themselves are very dependent on how the field components are extracted, the trends in the noise can be used for multiple purposes. One of the more useful purposes of knowledge of acquisition system noise is understanding the noise behaviour as a result of coil size. While the electromagnetic noise is scaling with the coil surface the drift noise is not.

This also means that from the analysis of how much noise in Tesla is occurring in the signal a new fluxmeter can be designed to meet the specifications of a measurement.
Of course, the next iteration should meet the requirements regarding noise levels but also be designed for solution. Design for solution indicates that the sensor is designed to accommodate whichever method is used to extract the field components with the required accuracy. Some surfaces might need an increased number of turns to become enough sensitive to the low field level (mT range), while others might have a large enough surface to need fewer turns.
This design change should be completely driven by the need for coil placements in the solution. However, if successful the design change might eradicate the need for filtering in the signal. However, while the design of a specific coil's surface and placements might indicate that filtering can be avoided, there can also be limits to the ability to design with a good enough resolution since every increase in surface per turn lowers the resolution in radial and azimuthal fields, and every turn will naturally decrease the resolution along the longitudinal axis.

The necessity of filtering in the electron cooler project

As already apparent in the discussions of the usage of noise analysis, this discussion is not completely independent.
However, the need for filtering depends on more than the design of the fluxmeter. While the design of the fluxmeter can alleviate a significant amount of noise problems it is not certain that it can be designed to both have the desired spatial resolution and describe the field adequately. The filter can be a way to fuse measurements with good resolutions for multiple directions or field components.

The general filtering can also be a way of using the coil measurements with low noise levels to correct the smaller coils which means that an extra sensor is not necessarily needed to apply the filter. However, this usage's feasibility depends on finding ways to extrapolate information of the field from one coil to another. Using signals from the same disc, however, removes the total independence of the measurements and might result in an amplification of mechanical imperfections or artifacts in the signal. Therefore, it is also important to address any such source of noise in the signal and reduce it to a minimum.
The use of filtering can also simply be affected by the addition of extra sensors for the sake of the project. It can be beneficial to add a Hall sensor to the setup since it gives the field along a desired direction. The ability to isolate a field direction and measure the field strength at an absolute position along that direction can be used to amplify the knowledge of the radial field in some positions of the magnet which can be a direct measurement of the field component that is needed for the correction scheme.
Generally, filtering in smaller and weaker magnets can be an asset that enables more accurate measurement of the field and provides the ability to make better physics. However, at the current stage, it might be unnecessary to improve the accuracy of some of the measurement techniques.

Future work

The further work consists of many different aspects of the project. In the measurement of the magnet, an analysis of the errors induced by mechanical instabilities needs to be performed and the setup needs to be improved to a degree where the variance of the measurements for any reason, being noise from mechanical sources, difference in the velocity of the disc or any other hindrance of creating a good enough solution. A solution to the design of the mechanics for the experiment could include a motor to translate the disc through the aperture which can provide a constant velocity.
A motorised system also provides multiple additional possibilities to either rotate or stop the sensor in different positions in order to obtain extra information about the field that is hard to get from the longitudinal sweep.
The further development of the experiment could also include an automated way of obtaining the field components since the modelling of the field in a meaningful way for the electron cooling experiment will need a B_φ component included. The reason is that the addition of the dipoles from both sides will shape the field in a way where the φ dependency in Equation 3.5 can no longer be assumed to be zero. Whether or not a model is the best solution can be discussed since other

options for obtaining the necessary information also might exist, such as direct measurements of the radial dipoles.

Conclusion 7

The general framework for this project is to improve the quality of measurements of solenoid magnets for electron coolers.
The rising requirements of electron cooling for low-energy particle beams create a demand for better and more sophisticated means of measurement and correction. These requirements can possibly be met by introducing fluxmeter measurements which are already a very used tool in in magnetic measurements for accelerator physics.
The translating fluxmeter is a known tool for measurements, but it has mostly been used for high-field magnets (tesla range), which automatically generate a large induction voltage. In the electron cooler project, the magnets are low-field per design to minimise the effect on the beam from the magnets. The low field gives a smaller signal and worsens the signal-to-noise ratio of the measurement. Using a Kalman filter combined with the fluxmeter can alleviate some of the noise and reduce the drift of the measurement. Estimating the drift instead of using a linear Kalman filter has also proven to be more efficient at tracking the low frequent noise of the fluxmeter measurement.
One necessary precaution when using the drift tracking Kalman filter is that the measurement and the filter should measure similar effects. Knowledge from the experiment with the Q520 and the Q522 coil shows that the difference in the surface integrals over the disc results in the bias-removing signal from the Q522 that might contain information about the magnet. Experiments also show that while the Kalman filter performs well on the well defined ramp signal a better model of the solenoid field is needed to extrapolate information inside the magnet using the filter.
While the effect of Kalman filtering for certain types of measurements has proven effective in this report the role of filtering in the measurement campaign of the solenoid magnet is still undetermined. The selection of filtering techniques will rely on the approaches to extract the necessary information from the fluxmeter in the final solution.

Bibliography

[1] J. Gillies. *CERN and the Higgs Boson: The Global Quest for the Building Blocks of Reality*. Hot Science. Icon Books, 2018.

[2] S. van der Meer. An introduction to stochastic cooling. *AIP Conference Proceedings*, 153(2):1628–1649, 02 1987.

[3] H Poth. Electron cooling: theory, experiment, application. *Physics reports*, 196(3-4):135–297, 1990.

[4] D Gamba, A Rossi, G Russo, and P Kruyt. Specifications for a new electron cooler of the antiproton decelerator at CERN. *JACoW*, IPAC2023:TUPM027, 2023.

[5] A Shemyakin, SS Nagaitsev, ES McCrory, A Bubley, AC Crawford, V Tupikov, VN Bocharov, S Seletsky, and VV Parkhomchuk. Fermilab electron cooling project: field measurements in the cooling section solenoid. 2001.

[6] A. Rossi on behalf of the AD E-Cooler team. Ad-cons electron cooler. In *IEFC Committee - 335th meeting*, 2023.

[7] I Shreyber. Introduction to electromagnetism, 2021.

[8] COMSOL Multiphysics. Introduction to comsol multiphysics®. *COMSOL Multiphysics, Burlington, MA, accessed Feb*, 9(2018):32, 1998.

[9] S Russenschuck. *Field Computation for Accelerator Magnets: Analytical and Numerical Methods for Electromagnetic Design and Optimization*. John Wiley & Sons, Ltd, 2010.

[10] C Petrone, S Sorti, E Dalane, B Mehl, and S Russenschuck. An induction-coil measurement system for normal- and superconducting solenoids. *IEEE Transactions on Applied Superconductivity*, 32:1–1, 09 2022.

[11] P. Arpaia et al. Proof-of-principle demonstration of a translating coils-based method for measuring the magnetic field of axially-symmetric magnets. *Journal of Instrumentation*, 2015.

[12] P Arpaia, B Celano, L De Vito, Antonio Esposito, Alessandro Parrella, and Alessandro Vannozzi. Measuring the magnetic axis alignment during solenoids working. *Scientific Reports*, 8, 2018.

[13] C Petrone, B Bordini, M Buzio, and S Russenschuck. A transducer for measuring the field quality in superconducting solenoids. *IEEE Transactions on Applied Superconductivity*, 30:1–5, 2020.

[14] M Pentella, V Mattsson Kjellqvist, C Petrone, S Russenschuck, and L. von Freeden. Alignment of a solenoid system by means of a translating-coil magnetometer. *IEEE Transactions on Applied Superconductivity*, 34(5):1–4, 2024.

[15] Internal fluxmeter design documents.

[16] P. Arpaia, L. Bottura, L. Fiscarelli, and L. Walckiers. Performance of a fast digital integrator in on-field magnetic measurements for particle accelerators. *Review of Scientific Instruments*, 83(2):024702, 02 2012.

[17] Hexagon Manufacturing Intelligence. Leica absolute tracker at930. 2022.

[18] VN Bocharov, AV Bublei, SG Konstantinov, VM Panasyuk, and VV Parkhomchuk. Precision measurements and compensation for the transverse components of the solenoids' magnetic field. *Instruments and Experimental Techniques*, 48:772–779, 2005.

[19] C. Germain. Bibliographical review of the methods of measuring magnetic fields. *Nuclear Instruments and Methods*, 21:17–46, 1963.

[20] L Markley. Attitude error representations for kalman filtering. *Journal of Guidance Control and Dynamics - J GUID CONTROL DYNAM*, 26:311–317, 03 2003.

[21] J Timmer and M Koenig. On generating power law noise. *Astronomy and Astrophysics*, 300:707, 1995.

[22] Melvin Liebsch. *Inference of Boundary Data from Magnetic Measurements of Accelerator Magnets*. PhD thesis, Technische Universität Darmstadt, Darmstadt, 2022.

[23] R.S. Popovic. *Hall Effect Devices*. ISSN. CRC Press, 2003.

[24] P Arpaia, M Buzio, V Di Capua, S Grassini, M Parvis, and M Pentella. Drift-free integration in inductive magnetic field measurements achieved by kalman filtering. *Sensors (Basel, Switzerland)*, 22, 2021.

Ellectron cooler technical specification A

EDMS NO.	REV.	VALIDITY
2772724	**1.0**	**RELEASED**

REFERENCE : AD-LNT-ES-0001

SPECIFICATION

Functional specifications for the new AD e-cooler

Abstract

This document provides the functional specifications for the new AD e-cooler on the basis of known effects and operation experience.

TRACEABILITY

Prepared by: D. Gamba, C. Carli, L. Ponce, A. Rossi, G. Tranquille, L. Varming Joergensen	**Date: 2022-09-26**
Verified by: W. Bartmann, M. Calviani, S. Doebert, M. Karppinen, D. Nisbet, J. Vollaire, M. Steck (GSI), L. Von Freeden, A. Frassier, J. Cenede, G. Khatri, C. Machado, J. Storey, Y. Thurel, F. Wenander, M. Wendt, O. Marqversen	**Date: 2023-02-08**
Approved by: F. Butin, B. Goddard, T. Lefevre, Y. Papaphilippou, R. Steerenberg	**Date: 2023-10-06**

Distribution: AD-CONS

Rev. No.	***Date***	***Description of Changes*** *(major changes only, minor changes in EDMS)*
0.1	2022-08-01	First draft for internal discussion
0.2	2022-09-01	Internal feedback received
0.3	2022-09-26	After discussion with TE-MSC colleagues
0.4	2023-02-08	After first iteration of EDMS comments on V0.3
1.0	2023-10-06	Minor corrections collected during final approval

Table of Contents

1 INTRODUCTION

The present AD electron cooler (e-cooler in the following) main components were originally built for the ICE e-cooler in the 1970's, then later used for the LEAR e-coolers and finally reassembled in a shorter version at AD. The magnetic system was built at Thrige Titan in Odense, Denmark in 1978, and the company ceased to exist in 2000. The consolidation of the AD e-cooler has been under discussion since 2015 as part of the AD CONSolidation (ADCONS) project. Major breakdowns of the electron collector during the 2018 run and the difficulties in retrieving spare parts, called for a review of the consolidation plans in 2019 [1], where the review panel recommended building a new and reliable e-cooler system to ensure the shortest downtime possible. During the review, it was agreed to profit from this consolidation and improve the cooling performance, getting closer to the initial AD design specifications [2] for which the cooling time was expected to take six seconds at 300 MeV/c and one second at 100 MeV/c.

Another important aspect to be tackled with the new e-cooler, as underlined also in the recent review of the AD e-cooler project [3], was to improve the accessibility to vacuum components to allow for faster intervention time and bake-out time.

This document summarises the leading aspects of the physics of e-cooling, provides an overview of the present performance of AD with emphasis on e-cooling, and finally gives the minimum and desired specifications for the new AD e-cooler. Constraints will also be given to ensure the compatibility of any new e-cooler with the present ring layout.

2 E-COOLING IN THEORY

The performance of any cooling system is typically measured by the cooling time and by the final equilibrium emittances that such a system can provide. The whole concept of e-cooling is based on merging a *cold* electron beam to the *hot* ion beam circulating in a ring for a portion of the latter. The electrons keep being refreshed, while the ions are cooled turn by turn, i.e. their beam emittances are progressively reduced. The actual dynamics of electron cooling depend on many parameters both of the e-cooler device and of ion optics and characteristics. In principle, neglecting any additional heating source affecting the circulating beam (e.g. Intra Beam Scattering (IBS), and Space Charge (SC)), one would expect that equilibrium is reached when the equivalent temperatures of the electron (T_e) and ion (T_i) beams equalise:

$$\frac{1}{2}k_B T_i \rightarrow \frac{1}{2}k_B T_e \tag{1}$$

where k_B is the Boltzmann constant ($8.62 \times 10^{-5}\,\mathrm{eVK}^{-1}$), T_i and T_e the ion and electron temperatures, respectively. In kinetic energy terms, eq. 1 can be rewritten:

$$\frac{1}{2}m_i\sigma_{V_i}^2 \rightarrow \frac{1}{2}m_e\sigma_{V_e}^2 \tag{2}$$

$$\sigma_{V_i} \rightarrow \sigma_{V_e}\sqrt{m_e/m_i} \tag{3}$$

where σ_{V_i} and σ_{V_e} are the r.m.s. velocity spreads, and m_i and m_e the ion and electron mass, respectively. The longitudinal and transverse ion velocity spreads can be related to typical beam quantities [4]:

$$\sigma_{V_{i_s}} \approx \beta c\sigma_p/p_0 \tag{4}$$

$$\sigma_{V_{i_{x/y}}} = \beta c\gamma\sqrt{\epsilon_{x/y}\gamma_{x/y}} = \beta c\gamma\sqrt{\frac{\epsilon_{x/y}}{\beta_{x/y}}} \tag{5}$$

where:

- β and γ are the relativistic factors, and c is the speed of light;
- $\epsilon_{x/y}$ are the geometric emittances of the ion beam, $\gamma_{x/y}$ and $\beta_{x/y}$ the Twiss function values in the cooling section, which is assumed to be in a waist of the optic functions;
- σ_p/p_0 is the ion beam relative momentum spread.

The temperature of the electrons ($k_B T_e$) in the interaction region is difficult to assess. For an ideal gun and following accelerating section, the transverse temperature of electrons is expected to remain equal to the cathode temperature (typically $0.1\,\mathrm{eV}$ assuming a thermionic cathode with $T_{\mathrm{cath}} = 1100\,\mathrm{K}$). In recent e-coolers, e.g. in LEIR [5], magnetic adiabatic expansion [6, 7] has been employed to reduce this temperature in the cooling section by reducing the cathode radius and increasing the magnetic field in the gun section to maintain the same e^- current density in the cooling section:

$$r_{\mathrm{drift}} \approx r_{\mathrm{cath}} \sqrt{\frac{B_{\mathrm{cath}}}{B_{\mathrm{drift}}}} \tag{6}$$

while reducing transverse e^- temperature:

$$k_B T_{\perp} \approx k_B T_{\mathrm{cath}} \frac{B_{\mathrm{drift}}}{B_{\mathrm{cath}}} \tag{7}$$

In practice, the effective transverse temperature is also strongly dependent on the optics of the gun design [7], and this can only be estimated with complex simulations, e.g. see [8].

The longitudinal temperature is considerably reduced by the acceleration process and final longitudinal temperature scales with the e^- kinetic energy (E_k) as [4]:

$$k_B T_{e\|} \approx \frac{\left(k_B T_{\mathrm{cath}}\right)^2}{4 E_k}. \tag{8}$$

From Eq. 8 one would expect temperatures below a few µeV for $E_k > 2.5\,\mathrm{keV}$, which is in practice not reached due to imperfections and other effects [4, 7], and typical values are instead of $k_B T_{e\|} \approx 1\,\mathrm{meV}$.

Due to the asymmetry between transverse and longitudinal temperatures after acceleration, it might be questionable how to compute the effective transverse and longitudinal electron velocity spreads, but here we will assume:

$$\sigma_{V_{e_\perp}} \approx \sqrt{\frac{k_B T_{\perp}}{m_e}} \tag{9}$$

$$\sigma_{V_{e_\|}} \approx \sqrt{\frac{k_B T_{\|}}{m_e}}. \tag{10}$$

From the considerations above one would conclude that:

$$\beta c \sigma_p/p_0 \to \sigma_{V_{e\|}} \sqrt{m_e/m_i} \qquad \text{i.e.:} \quad \sigma_p/p_0 \to \frac{\sqrt{k_B T_{e\|}/m_i}}{\beta c} \tag{11}$$

$$\beta c \gamma \sqrt{\frac{\epsilon_{x/y}}{\beta_{x/y}}} \to \sqrt{k_B T_{\perp}/m_i} \qquad \text{i.e.:} \quad \epsilon_{x/y} \to \frac{\beta_{x/y} k_B T_{\mathrm{cath}}}{m_i \beta^2 c^2 \gamma^2} \frac{B_{\mathrm{drift}}}{B_{\mathrm{cath}}} \tag{12}$$

which for AD at 100 MeV/c with $\beta_x/y \approx 10\,\mathrm{m}$ would correspond to an equilibrium momentum spread of about 1×10^{-5} and emittance of about $0.1\,\mu\mathrm{m}$.

Unfortunately, system imperfections and the strength of beam heating effects such as space-charge (SC), intra-beam scattering (IBS), and scattering with the rest gas, make this extremely low equilibrium emittance estimate far from being realistic. To obtain more realistic numbers, detailed simulation studies are needed, and this is part of the long-term effort being put in place [9].

The typically accepted [5, 7, 10] scaling law for the cooling time in the laboratory frame is given by:

$$\tau \approx 4 \times 10^{12} [\mathrm{A\,s\,m^{-2}}] \frac{L_{\text{ring}}}{L_{\text{cooler}}} \frac{A}{q^2} \frac{r^2_{\text{e-beam}}}{I_{\text{e-beam}}} \beta^4 \gamma^2 [\gamma^2(\Theta_x^2 + \Theta_y^2) + \Theta_s^2]^{3/2} \tag{13}$$

where:

- L_{ring} and L_{cooler} are the lengths of ring and e-cooler active section, respectively. In the case of AD they are $L_{\text{ring}} = 182.43\,\mathrm{m}$ and $L_{\text{cooler}} \approx 1.5\,\mathrm{m}$.
- A and q are the ion mass number and charge state, respectively. For antiproton beams, both are clearly equal to 1.
- $r_{\text{e-beam}}$ is the radius of the electron beam in the cooling section, which, together with electron current, $I_{\text{e-beam}}$, defines the electron current density available for cooling.
- $\Theta_{x/y}$ and Θ_s are the r.m.s. angular and momentum difference between the ion and the electron beams, i.e.:

$$\Theta_{x/y} \approx \sqrt{\epsilon_{x/y}/\beta_{x/y} + (\sigma_{V_{e\perp}}/(\gamma\beta c))^2} \tag{14}$$

$$\Theta_s \approx \sqrt{(\sigma_p/p_0)^2 + (\sigma_{V_{e\parallel}}/(\beta c))^2} \tag{15}$$

  where $\sigma_{V_{e\perp}}$ and $\sigma_{V_{e\parallel}}$ are the transverse and longitudinal electron velocity spreads introduced in Eq. 9 and 10, respectively.

In practice, Eq. 13 gives only an indicative value for the expected cooling time, and important parameters such as electron beam magnetisation (quality and intensity of the e-cooler magnetic field), other properties of the electron beam (e.g. actual shape of the transverse profile, and velocities distribution), alignment between electron and ion beams, and optic dispersion function at the e-cooler, for example, are not explicitly considered. For example, in case of magnetised cooling, the dependencies on $\sigma_{V_{e\perp}}$ and $\sigma_{V_{e\parallel}}$ in Eq. 14 and Eq. 15 should rather be replaced by an effective electron velocity spread [11] mainly driven by the longitudinal electron temperature and the magnetic field straightness. Those dependencies are expressed in different models of the e-cooling force in a non-trivial way, see for example [7, 9, 11, 12, 13], but often one relies on empirical observations to extrapolate scaling laws for a given parameter, e.g. in [10] for the dependence of cooling on ring optics parameters.

Despite the difficulty in obtaining a solid and accurate prediction of cooling time and final emittances, one can still use the previous relations as guidelines when designing a new e-cooler to identify key parameters and desired orders of magnitude. From those guidelines and past experience, we can make the following observations:

- Cooling time is inversely proportional to the electron current ($\tau \propto 1/I_{\text{e-beam}}$), neglecting that higher currents could affect the electron temperatures and/or velocity distribution. This is compatible with previous experimental observations, e.g. [10].
- Cooling time quickly increases with operating energy ($\tau \propto \beta^4\gamma^5$).
- Equations 13 and 14 call for large beta functions at the e-cooler ($\tau \propto \beta_{x/y}^{-3/2}$) for faster cooling time, while Eq. 12 suggests low beta functions ($\epsilon_{x/y}^{\text{eq.}} \propto \beta_{x/y}$) for lower final emittances. An optimum value

might be expected for low beta function values. This behaviour was observed on the cooling time measured as a function of beta function in LEAR e-cooler [10], where an optimum for $\beta_x \approx 5m$ was observed, even though this result is unclear as the measurement was convoluted with a change of the dispersion function at the e-cooler, which might have had a dominant effect.

Additionally, one should consider that the beam size, including tails or at least up to three sigma, at the e-cooler (i.e. $3\sqrt{\epsilon^{\text{init.}}_{x/y}\beta_{x/y}}$) must remain within the electron beam radius, i.e.

$$\beta_{x/y} < \frac{r^2_{\text{e-beam}}}{9\epsilon^{\text{init.}}_{x/y}} \tag{16}$$

which, assuming the present AD e-cooler e-beam $r_{\text{e-beam}} = 25\,\text{mm}$ and initial pbar-beam $\epsilon^{\text{init.}}_{x/y} \approx 10\,\mu\text{m}$ would give $\beta_{x/y} < 7\,\text{m}$. Vice versa, assuming a $\beta_{x/y} \approx 10\,\text{m}$, and $\epsilon^{\text{init.}}_{x/y} \approx 10\,\mu\text{m}$, then a radius of $r_{\text{e-beam}} \approx 30\,\text{mm}$ is required to fit a three-sigma beam profile inside the e-beam.

- The values of $\Theta_{x/y}$ in Eq. 14 are strongly affected by the electron temperature: assuming typical AD values of $\beta_{x/y} \approx 10\,\text{m}$, and $\epsilon^{\text{init.}}_{x/y} \approx 10\,\mu\text{m}$, then $\sqrt{\epsilon_{x/y}/\beta_{x/y}} \approx 1\,\text{mrad}$, to be compared to $\sigma_{V_{e\perp}}/(\gamma\beta c) \approx 4\,\text{mrad}$ assuming $T_\perp = 0.1\,\text{eV}$ at $100\,\text{MeV/c}$.
  In the longitudinal plane, i.e. Θ_s from Eq. 15, the electrons have a smaller impact due to their lower temperature, typically $T_\parallel = 1\,\text{meV}$. In this case, typical values are $(\sigma_p/p_0)_{\text{init.}} \approx 10^{-3}$ and $\sigma_{V_{e\parallel}}/(\beta c) \approx 4 \times 10^{-4}$ at $100\,\text{MeV/c}$.
- The electron longitudinal velocities inside the electron beam vary with the distance from the beam centre as a result of space-charge effects. For a uniform e^- transverse distribution this is expected to be [4]:

$$\frac{\Delta E(r)}{E} \approx 1.2 \times 10^{-4} \frac{I_{\text{e-beam}}[\text{A}]}{\beta^3} \left(\frac{r}{r_{\text{e-beam}}}\right)^2 \tag{17}$$

  Taking as an example the present AD e-cooler at $100\,\text{MeV/c}$ with $I_{\text{e-beam}} = 100\,\text{mA}$, $\beta \approx 0.1$, $E \approx 3\,\text{keV}$, and $r_{\text{e-beam}} = 25\,\text{mm}$, the energy excess at the edge of the electron beam is as high as $36\,\text{eV}$. However, rest-gas ions trapped in the magnetic field of the e-cooler can partially or completely suppress this energy spread, a phenomenon also called neutralisation and indicated with the scaling η [14]. This effect plays an important role in the cooling process when associated with ion beam dispersion in the cooling section, which couples longitudinal and transverse cooling [4, 9, 14]. Previous experience [10] suggests that non-zero dispersion ($|D| \approx 1m$) gives the shortest cooling time. Note that neutralisation can lead to instabilities, as in [15], therefore the recommendation of [16] is that "modern coolers should be designed to avoid natural neutralisation", hence care has to be taken in the vacuum chamber design and to avoid trapping of ions.
- For a given geometric configuration of a diode electron gun (cathode radius r_0 and cathode-anode distance, d), the maximum beam current typically follows the Child's law [4]:

$$I_{gun} = P(V_{\text{cathode}} - V_{\text{anode}})^{3/2} \tag{18}$$

$$P = \text{Gun perveance} \tag{19}$$

$$\approx 7.3 \times 10^{-6}(r_0/d)^2[\text{AV}^{-3/2}]. \tag{20}$$

  The actual e-beam current (and eventually transverse profile) can be controlled by installing additional electrodes in the gun. For example, the gun design considered for the new e-cooler is based on a diode gun with an accelerating gap [17] which allows to control independently beam current and energy.

- The longitudinal magnetic field is necessary in the first place to confine the electron beam, counteracting space charge, and guide it from the gun to the collector of the e-cooler. A high magnetic field makes it easier to transport the electron and to avoid instabilities, while it might have detrimental effects on the circulating beam. The minimum necessary magnetic field strength for ensuring a stable transport of the beam could be assessed with detailed simulations similar to what was done in [18]. However, the present working hypothesis is to keep the current AD e-cooler field strength ($600\,\mathrm{G}$) also for the new e-cooler, at least in the interaction region.
- The longitudinal magnetic field is also a necessary ingredient for enhancing the cooling force, at least for small electron-ion transverse and/or longitudinal velocity differences. The magnetisation condition [7, 13] is obtained when the Larmor radius (r_L) of the electrons spinning around the magnetic field lines is smaller than the typical distance between electrons (d_{ee}) and the Debye length (λ_D):

$$r_L = \frac{m_e \sigma_{V_{e\perp}}}{Be} < \max\left\{ d_{ee} = \left(\frac{3}{n_e}\right)^{\frac{1}{3}} ; \lambda_D = \sqrt{\frac{\epsilon_0 k_B T_{\parallel}}{n_e e^2}} \right\} \tag{21}$$

where:

$$n_e = \frac{I_{\text{e-beam}}}{\beta c e \pi r_{\text{e-beam}}^2} \tag{22}$$

and in more convenient units is typically fulfilled for:

$$B[\mathrm{T}] > 3.1 \times 10^{-3} \sqrt{T_{\perp}[\mathrm{eV}]} \left(\frac{I_{\text{e-beam}}[\mathrm{A}]}{\beta r_{\text{e-beam}}^2 [\mathrm{m}^2]} \right)^{\frac{1}{3}} \tag{23}$$

For the present AD e-cooler at $p = 300\,\mathrm{MeV/c}$ ($\beta = 0.3$) and assuming $T_{\perp} = 0.1\,\mathrm{eV}$, $I_{\text{e-beam}} = 2.4\,\mathrm{A}$, and $r_{\text{e-beam}} = 25\,\mathrm{mm}$ one obtains:

$$B > 230\,\mathrm{Gauss} \tag{24}$$

This condition is amply met by the $600\,\mathrm{Gauss}$ used in the present AD e-cooler, for which one obtains:

$$r_L \approx 12\,[\mu\mathrm{m}] \tag{25}$$
$$n_e \approx 8.48 \times 10^{13} [1/\mathrm{m}^3] \tag{26}$$
$$\lambda_D \approx 25.5\,[\mu\mathrm{m}] \tag{27}$$
$$d_{ee} \approx (3/n_e)^{\frac{1}{3}} \approx 32.8\,[\mu\mathrm{m}] \tag{28}$$

- Strong variations of the guiding magnetic field along the electron trajectory can also increase electron temperatures. A typical requirement to avoid heating is that the change of magnetic field strength must be much longer than the spiral length of the cyclotron motion, which can be translated in the adiabatic condition [19]:

$$\chi = \frac{\lambda_c}{B} \left| \frac{\mathrm{d}\vec{B}}{\mathrm{d}z} \right| \ll 1 \tag{29}$$

where λ_c is the spiral length of the cyclotron motion:

$$\lambda_c[\mathrm{m}] = \frac{2\pi m_e}{eB} \gamma\beta c \approx 1.07 \times 10^{-2} \frac{\gamma\beta}{B[\mathrm{T}]} \tag{30}$$

which for the present AD e-cooler at $p = 300\,\mathrm{MeV/c}$ ($\beta = 0.3$) and $B = 600\,\mathrm{Gauss}$ is $\lambda_c \approx 54\,\mathrm{mm}$, which therefore imposes:

$$\left|\frac{\mathrm{d}\vec{B}}{\mathrm{d}z}\right| \ll 11\,[\mathrm{Gauss/mm}] \tag{31}$$

- Each electron inside the electron beam also experiences space-charge force induced by the self-induced electric and magnetic field. For a round and transversely uniform electron beam distribution such a force is expressed as [20, 21]:

$$F_r(r) = \frac{eI_{\text{e-beam}}r}{2\pi\epsilon_0\beta c r_{\text{e-beam}}^2\gamma^2} \tag{32}$$

where r is the radial position of the electron under consideration. This force is counteracted by the presence of the e-cooler magnetic field which makes electrons rotate around the field lines. At the same time, the electrons will rotate around the beam axis with angular velocity

$$\omega[\mathrm{s}^{-1}] = \frac{\vec{F}\times\vec{B}}{er|B|^2} = \frac{I_{\text{e-beam}}}{2\pi\epsilon_0 c r_{\text{e-beam}}^2\beta\gamma^2 B_\parallel} \approx 60\frac{I_{\text{e-beam}}[\mathrm{A}]}{r_{\text{e-beam}}^2[\mathrm{m}^2]\beta\gamma^2 B_\parallel[\mathrm{T}]} \tag{33}$$

This effect can induce turbulent motion, hence temperature increase as shown in [18], and is reduced for high magnetic fields ($1/B_\parallel$) and high energy beams ($1/(\beta\gamma^2)$). In order to avoid the development of instabilities a general criterion [18] is to impose a revolution period ($2\pi/\omega$) longer than the time for the electron beam to go from gun to collector ($L_{\text{e-cooler}}/(\beta c)$). For the AD e-cooler typical parameters at $p = 300\,\mathrm{MeV/c}$, the electrons travel from gun to collector in less than $0.1\,\mu\mathrm{s}$, while one full rotation along its axis takes more than $0.5\,\mu\mathrm{s}$, hence the stability criterion is met. On the other hand, the tangential velocity for electrons ($V(r) = \omega r$) can be comparable to the transverse velocity spread of the electrons ($\sigma_{V_{e\perp}}$, Eq. 9) in the outer layers of the beam. For AD e-cooler parameters at $p = 300\,\mathrm{MeV/c}$, one should compare $\sim 1.3\times10^6\,\mathrm{m/s}$ transverse thermal velocities, assuming $T_\perp = 0.1\,\mathrm{eV}$, and $\sim 2.8\times10^6\,\mathrm{m/s}$ tangential velocity at the edge of the electron beam, i.e. at $r = r_{\text{e-beam}} = 25\,\mathrm{mm}$, and $B = 600\,\mathrm{Gauss}$. This might be a limiting factor for cooling of tails, and it could be an argument to go to as high magnetic fields as possible.

- If the transverse temperature of the electrons tends to average out for magnetised beams, the straightness of the magnetic field in the cooling section can become comparable or dominant in defining the effective transverse temperature. In particular, the apparent electron transverse velocity due to the magnetic field imperfection should be smaller than the transverse velocity associated with the transverse [4] as well as longitudinal [22] electron temperatures along the interaction region:

$$c\gamma\beta B_\perp/B_\parallel \ll \sqrt{\frac{k_B T_{e\parallel}}{m_e}} < \sqrt{\frac{k_B T_{e\perp}}{m_e}} \tag{34}$$

i.e. assuming a longitudinal temperature $k_B T_{e\parallel} \approx 1\,\mathrm{meV}$ and for $\beta\gamma \approx 0.3$, then one would need $\mathrm{rms}(B_\perp/B_\parallel) \ll 1.5\times10^{-4}$. This requirement is compatible with the typical value of $\mathrm{rms}(B_\perp/B_\parallel) \lesssim 1\times10^{-5}$ for other e-cooler devices, e.g. [23, 24, 25, 26, 27], as well as values obtained in similar recent e-coolers [28], and it seems in reach of the measurement capabilities developed for LEIR [29].

- The alignment between the ion beam and the electron beam has also to be comparable or better than the desired final divergence of the beam $\approx \sqrt{\epsilon_{x/y_{\text{final}}}/\beta_{x/y}}$. For $\beta_{x/y} \approx 10\,\mathrm{m}$ and $\epsilon_{x/y} \approx 1\,\mu\mathrm{m}$,

one would therefore require an alignment better than $300\,\mu\mathrm{rad}$. This requirement calls for precise beam instrumentation, e.g. Beam Position Monitors (BPMs) with a resolution and precision better than $100\,\mu\mathrm{m}$, and an overall alignment of the average magnetic field along the interaction region with respect to the ring reference system of similar tolerance. Larger misalignment, say of the order of $1\,\mathrm{mm}$ and/or $1\,\mathrm{mrad}$, can be tolerated provided the strength of nearby orbit correctors will allow for implementing orbit bumps to match the original e-ion alignment tolerance.

- The stability of the high voltage should be much better than the desired final energy spread of the circulating beam. Typical values for this specification are of the order of 10^{-5} [7, 28].
- Back-scattered electrons from the collector back into the cooling section have to be minimised, since they can perturb cooling and make it unstable, or generate gas disruption and increase background pressure in the accelerator. According to the literature, in order to obtain excellent e-cooling performance, electron collection inefficiency should be kept at the order of 10^{-5} [7].
- The electron current stability is typically specified to be of the order of 10^{-4} [28].

2.1 Electron Dynamics in the Toroids

Toroids are used to bend the electron beam into the cooling section where they are merged with the circulating beam. The smoothness of the magnetic field in this region deserves particular care to ensure that the electrons' temperature is not increased.

Additionally, due to the curved magnetic field lines, the electrons experience a centrifugal force generating a lateral velocity drift, v_d:

$$v_d = \frac{\gamma m_e (\beta c)^2}{e r_{\mathrm{tor}} B_{\mathrm{tor}}} \tag{35}$$

which, integrated over the length of the toroid arc, induces a lateral drift of the electron beam trajectory of approximately:

$$\Delta X[\mathrm{m}] = -1.7 \times 10^{-3} \beta\gamma \frac{\phi_{\mathrm{tor}}[\mathrm{rad}]}{B_{\mathrm{tor}}[\mathrm{T}]} \tag{36}$$

For typical AD values at $300\,\mathrm{MeV/c}$ of $\beta\gamma = 0.3$, $B_{\mathrm{tor}} = 0.06\,\mathrm{T}$, and $\phi_{\mathrm{tor}} = 0.629\,\mathrm{rad}$ this corresponds to a drift of $-5.4\,\mathrm{mm}$. To be noted that for higher momenta or lower B field this value can quickly increase.

At a first order, this effect is usually compensated by introducing an additional lateral magnetic field:

$$\int B_x \mathrm{d}s = -\Delta X B_{\mathrm{tor}} = 1.7 \times 10^{-3} \beta\gamma\phi_{\mathrm{tor}} \tag{37}$$

which for typical AD values at $300\,\mathrm{MeV/c}$ is about $3\,\mathrm{Gm}$.

Alternatively, this drift can be compensated by adding a radial electric field pointing toward the centre of the toroid curvature:

$$E_y = v_d B_{\mathrm{tor}} = \frac{\gamma m_e (\beta c)^2}{e r_{\mathrm{tor}}} \approx 5.1 \times 10^5 \frac{\gamma\beta^2}{r_{\mathrm{tor}}} \tag{38}$$

For the present AD values at $300\,\mathrm{MeV/c}$, i.e. $\gamma = 1$, $\beta = 0.3$, and $r_{\mathrm{tor}} = 1.133\,\mathrm{m}$, E_y is about $40\,\mathrm{kV/m}$. This configuration, also called "electrostatic bend", was chosen for the LEIR e-cooler [11], and it also appeared to reduce electron losses and therefore improve the vacuum level inside the e-cooler.

Note that e-cooling is used in AD at least at two different momenta (today, $300\,\mathrm{MeV/c}$ and $100\,\mathrm{MeV/c}$) along the same cycle, hence the compensation of the lateral electron beam trajectory should be adjusted for the two energies.

The toroid has also the most complex vacuum chamber. Care has to be taken in this region to avoid the undesired accumulation of trapped charged ions that can have detrimental effects on electron transport and cooling stability. This can be cured by adding clearing electrodes that trap charged ions on their surfaces. The use of an electrostatic bend for compensating the lateral electron drift mentioned above could also serve as clearing electrodes. However, the clearing electric field (E_{ce}) should be larger than the electron beam maximum space charge field [30]:

$$E_{ce}[\mathrm{V/m}] > \max(E_e) = \frac{I_{\text{e-beam}}}{2\pi\epsilon_0\beta c r_{\text{e-beam}}} \approx 60\frac{I_{\text{e-beam}}[\mathrm{A}]}{\beta r_{\text{e-beam}}[\mathrm{m}]} \tag{39}$$

For typical AD values at $300\,\mathrm{MeV/c}$, i.e. $\beta = 0.3$, $I_{\text{e-beam}} = 2.4\,\mathrm{A}$ and $r_{\text{e-beam}} = 0.025\,\mathrm{m}$ the minimum field should be of about $20\,\mathrm{kV/m}$, hence an "electrostatic bend" might also serve as a clearing mechanism for DC electron beams, at least up to present current/energy. On the other hand, we did not consider the presence of the longitudinal magnetic field, and the fact that the electron beam will be on for a limited amount of time ($\approx 20\,\mathrm{s}$) with respect to the AD cycle length ($\approx 100\,\mathrm{s}$), hence the expected ionisation rates should be investigated more in detail.

2.2 Additional Impact on Circulating Beam: Coupling and Orbit Kick

For the circulating ion beam, each toroid can be seen as a solenoid and bending field which will kick the beam in the plane perpendicular to the toroid bending arc. The strength of the kick can be estimated as [4]:

$$\theta_x = \left(\cos^{-1}(\phi_{\text{tor}}) - 1\right)\frac{B_{\text{tor}} r_{\text{tor}}}{B\rho} \tag{40}$$

For the present AD e-cooler ($B_{\text{tor}} = 600\,\mathrm{Gauss}$, $\phi_{\text{tor}} = 0.629\,\mathrm{rad}$, $r_{\text{tor}} = 1.133\,\mathrm{m}$) one obtains an integrated transverse field of about $16\,\mathrm{mTm}$ which causes transverse kicks to the circulating beam up to $50\,\mathrm{mrad}$ at the lowest energy plateau of $100\,\mathrm{MeV/c}$. The obtained value is compatible with what was found in measurements on the AD e-cooler at the time of LEAR [23]. At least two orbit correctors are necessary on each side of the e-cooler to minimise the amplitude of the ion orbit bump that the toroids generate in the relevant plane. The closest orbit corrector should be as close as possible to the toroid, i.e. at a distance less than or equal to the present e-cooler one (i.e. $< 0.8\,\mathrm{m}$) such as to limit the circulating beam orbit excursion next to the e-cooler. Care should be taken to ensure that the magnetic field of these orbit correctors does not perturb the magnetic field, and hence the trajectory of the electron beam, inside the e-cooler.

The integrated longitudinal field of the toroids and of the drift solenoid introduces coupling in the circulating beam. This is usually corrected by solenoids installed in the vicinity of the e-cooler, also called compensation solenoids. Ideally, the compensation solenoids should be placed as close as possible to the e-cooler such as to keep the optics distortion as local as possible. A formalism to express coupling for machine tunes Q_x and Q_y very close to each other is given by the terms $C^{\pm}$ [31]:

$$\left|C^{\pm}\right| \approx \frac{1}{2\pi}\left|\oint ds\sqrt{\beta_x(s)\beta_y(s)}k_s(s)e^{-i(\phi_x(s)\pm\phi_y(s))}\right| \tag{41}$$

where $\beta_{x/y}(s)$ are the Twiss beta functions and $K_s(s)$ the integrated strength of the coupling sources, e.g. solenoids in our case, along the machine (s) and $\phi_{x/y}(s)$ the phase advances. The values of $C^{\pm}$ are related

to the minimum tune separation one can have in a machine, Eq. 42, and the stability condition, Eq. 43.

$$\Delta Q_{\min} = \left|C^-\right| \tag{42}$$

$$\left|C^+\right| \leq 1 - (Q_x + Q_y) \tag{43}$$

Assuming that beta functions and phase advance are not changing drastically over the cooling section (see Fig. 3), one would expect a total integrated strength for the compensating solenoids comparable to the strength of the e-cooler integrated solenoidal field.

Additionally, the field of the toroids on the outer side of the e-cooler will produce high-order magnetic field components that will also introduce coupling and other non-linear effects to the circulating beam. It is therefore important that during the design and production of the e-cooler magnetic system, those non-linear components are minimised or at least computed and measured.

Note that for tunes close to the half-integer resonance, the stability condition, Eq. 43, might become a limiting factor. Good control of coupling is therefore essential for reliable operation of a machine with e-cooling.

3 PRESENT AD PERFORMANCE

The purpose of AD is to collect pbars, cool and decelerate them from the injection momentum of $3.57\,\mathrm{GeV/c}$ to the extraction momentum of $100\,\mathrm{MeV/c}$. In order to cool the pbar beam at injection and during deceleration both stochastic cooling and electron cooling are employed, with the stochastic cooling acting over two plateaus at $3.57\,\mathrm{GeV/c}$ and $2\,\mathrm{GeV/c}$, and the electron cooling acting over two plateaus at $300\,\mathrm{MeV/c}$ and $100\,\mathrm{MeV/c}$ before extraction. The figures of merit of the AD cycle are therefore:

- Captured intensity, linked to the target pbar yield, the injection line transport efficiency and the s-cooling performance;
- Transmission along the cycle, linked to ring optics, RF control and both stochastic and electron cooling performance;
- Cycle length, mainly driven by stochastic and electron cooling performance as well as by tolerated losses along the deceleration cycle;
- Number of successful deceleration cycles for physics, mainly affected by systems reliability.

A typical cycle in AD is shown in Figure 1. The recent experience shows that most shot-to-shot intensity fluctuations are visible after deceleration from $2\,\mathrm{GeV/c}$. This might be due to poor performance of the stochastic cooling at $2\,\mathrm{GeV/c}$, and due to lower rigidity and higher sensitivity to magnetic field perturbations and systems - including the present e-cooler - reliability at lower momenta.

The present cycle is the result of more than 20 years of experience and adjustments with the aim to maximise the pbar beam intensity delivered to the users. The main limitations for the optimisation and improvement of the cycle have been the shortage of accurate beam instrumentation, due to the extremely low beam intensity, and some legacy equipment with limited control capabilities, which are progressively being consolidated [32]. The low cycle repetition rate and the need to deliver as many shots as possible to the rich and enthusiastic experiment community gives only a few opportunities for machine studies, which are often devoted to troubleshooting system faults occurring regularly. As also highlighted in the recent e-cooler reviews [1, 3], it is clear that improving the reliability of various systems, including the e-cooler, will already allow for more efficient optimisation, likely leading to faster setup, troubleshooting, and possibly shorter cycles and therefore higher physics throughput of the facility.

The layout of the electron cooling section as built today is shown in Fig. 2. The e-cooler is installed vertically

in a U shape. Due to space constraints and available hardware at the time of AD construction, the compensation solenoids were installed at the outer side of the quadrupole doublets (actually made of three quadrupoles each) that control the optics inside the e-cooler.

This setup is not ideal in terms of coupling compensation, but it allowed to have pairs of horizontal correctors on each side of the e-cooler, which is necessary to keep the orbit bump induced by the toroids under control, see Fig. 3b. The orbit corrector strength necessary in simulation to close the bump induced by the solenoids, as in Fig.3b, is reported in Table1. Note that the PXMCXABCIP-type magnets are required to run

Table 1: Magnetic strength and corresponding running current of horizontal orbit correctors installed next to the e-cooler to ensure closure of toroid-induced orbit bump.

DR.DHV2904 and DR.DHV2917 (†)	$0.018\,\mathrm{Tm}$	$9.5\,\mathrm{A}$
DR.DHZ2908 and DR.DHZ2913 (‡)	$0.033\,\mathrm{Tm}$	$4.7\,\mathrm{A}$

† Presently magnets of type PXMCCAVWAP with nominal integrated field of $0.028\,\mathrm{Tm}$.

‡ Presently magnets of type PXMCXABCIP with nominal integrated field of $0.031\,\mathrm{Tm}$.

above the design strength and close to saturation [33]. Additional orbit correction strength is necessary for both transverse planes to allow for controlling the pbar-electron trajectory overlap.

During recent measurements, it has been observed that the pbar orbit inside the e-cooler is not constant during the plateaus, as shown in Fig. 4, while the electron beam orbit is. The observed drift is certainly a threat to e-cooling performance. It might be due to field lag error in the main dipoles and will need to be investigated and hopefully corrected in the future.

The Twiss functions at the e-cooler are reported in Table 2. Note that the values reported in Table 2 have

Table 2: Optics functions in the AD ring and e-cooler.

Q_x	5.44
Q_y	5.42
$\beta_x[\mathrm{m}]$	10
$\beta_y[\mathrm{m}]$	4
$D_x[\mathrm{m}]$	0.12
$\lvert C^- \rvert$	$< 10^{-4}$

been computed according to the present MAD-X model of the machine [34], but they are not necessarily the ones used in operation, as they have not been accurately measured. The integrated solenoid strength is assumed to be equal to $0.176\,\mathrm{Tm}$ and it is compensated by powering both compensating solenoids at $0.049\,\mathrm{Tm}$ which corresponds to $218\,\mathrm{A}$ for the installed magnets of type PXML_BA_WC.

4 NEW E-COOLER SPECIFICATIONS

The purpose of the new AD e-cooler is primarily to replace the existing cooler with the aim of ensuring an availability of say 99%, which also means addressing the shortage of spare parts as for the present e-cooler. At the same time, one should try improving certain limitations present in the today e-cooler. The minimum desiderata are:

- Allow for measuring and controlling the electron and ion beam trajectories inside the cooling section better than $100\,\mu\mathrm{m}$ and $300\,\mu\mathrm{rad}$ and over a range of a few millimetres (say $\pm 5\,\mathrm{mm}$). This measurement precision could be achieved with at least two Beam Position Monitors (BPMs) installed at the

extremities of the drift solenoid in the interaction region with relative accuracy between electrons and pbars of about $100\,\mu\mathrm{m}$.

- Increase the corrector strength of the closest pbar orbit correctors to ease the compensation of the toroid-induced kicks and allow for comfortable adjustment of the pbar-electron trajectories overlap.
- Foresee electron orbit steering coils in the gun and collector transport solenoids to adjust the horizontal and vertical electron beam position before and after entering the cooling section. For a minimum electron orbit steering of $5\,\mathrm{mm}$ one needs approximately

$$B_{x/y} = 5 \times 10^{-3} B_0 \approx 3\,[\mathrm{G}\cdot\mathrm{m}] \tag{44}$$

transverse integrated magnetic fields at those locations, assuming $B_0 = 600\,\mathrm{G}$. Margins should be taken in order to compensate for unforeseen effects.

- Foresee electron orbit steering coils all along the cooling section solenoid to tune the angle on the electron beam trajectory. For a minimum angle of $5\,\mathrm{mrad}$, one needs approximately:

$$B_{x/y} = 5 \times 10^{-3} B_0 \approx 3\,[\mathrm{G}] \tag{45}$$

transverse magnetic fields all along the cooling region for the given $B_0 = 600\,\mathrm{G}$. Margins should be taken in order to compensate for unforeseen effects.

- Verify the possibility of implementing an electrostatic bend in the toroid (up to about $113\,\mathrm{kV/m}$ for a $68\,\mathrm{keV}$ electron beam, see Eq. 38) to avoid lateral drift of the electron beam and charged ions accumulation. Alternatively, add steering magnetic coils in the toroids (up to about $5\,\mathrm{Gm}$ for a $68\,\mathrm{keV}$ electron beam, see Eq. 37). In this case, however, one should check the need (or not) of clearing electrodes to suppress charged ions accumulation.
- Ensure a good electron collection efficiency and therefore minimise the expected electron losses. Ideally, one should target a relative electron beam loss rate lower than $\delta I/I_0 < 10^{-4}$.
- Ensure that pumping capabilities will guarantee a vacuum pressure in the e-cooler drift region equal to or below the levels we have today (in the order of $5 \times 10^{-11}\,\mathrm{mbar}$ H_2 equivalent pressure with pulsed electron beam operation). Note that, today, the neighbour vacuum chambers are not NEG coated and static vacuum levels in those chambers are of the order of $1 \times 10^{-10}\,\mathrm{mbar}$ H_2 equivalent. Assuming those boundary conditions, the vacuum simulations presented in [36] show that realistic target vacuum levels in the e-cooler are $< 5 \times 10^{-11}\,\mathrm{mbar}$ H_2 equivalent pressure in static conditions and $< 1 \times 10^{-10}\,\mathrm{mbar}$ H_2 equivalent with DC electron beam ($3.5\,\mathrm{A}$) dumped on the bottom collector surface at $4\,\mathrm{keV}$ after 10 days of continuous operation.
- Aim for electron temperatures, after acceleration and, if needed, transverse expansion, close or better than typical values of $k_B T_\perp = 0.1\,\mathrm{eV}$ and $k_B T_\parallel = 0.001\,\mathrm{eV}$.
- Control the electron energy better than presently $1\,\mathrm{eV}$, to say $0.1\,\mathrm{eV}$, at the lowest electron energy of $2.9\,\mathrm{keV}$. Consequently, the energy stability should be better than $0.1\,\mathrm{eV}$, such to be comparable with an electron beam temperature of $k_B T_\parallel \approx 0.001\,\mathrm{eV}$ and the ideal equilibrium energy spread of $\Delta E/E \sim 10^{-5}$. For higher energies, $300\,\mathrm{MeV/c}$ pbar momentum or $25.5\,\mathrm{keV}$ electron energy, the present electron energy control resolution of $1\,\mathrm{eV}$ is acceptable.
- There is no strict requirement on the electron beam current stability during cooling. A reasonable target is $\Delta I/I_0 \sim 10^{-4}$ as in [28].
- The AD e-cooler is used to cool the circulating pbar beam at two different energy plateaus during the same cycle, see Fig. 1. Each plateau is a few seconds long and they are separated by a few seconds

long ramps. In order to avoid that the length of the AD cycle is constrainted by the electron beam start/stop duration, it must be possible to switch the electron beam on/off at the required energy and current intensity in less than one second. Additionally, it would be beneficial to start and especially to stop the electron beam current in less than a few tens of milliseconds, to minimise the time during which the circulating beam is interacting with an unmatched electron beam, and therefore minimise emittance blow up especially after cooling.

- Aim for a magnetic field straightness in the cooling region such that $\max(B_\perp/B_\parallel) = 10^{-4}$ and/or $\mathrm{rms}(B_\perp/B_\parallel) < 10^{-4}$. This value should be computed taking the perpendicular ($B_\perp$) and parallel ($B_\parallel$) components of the e-cooler field with respect to the Cartesian coordinate system with the longitudinal axis coinciding with the ideal path of the circulating pbar beam. The cooling region is defined as a cylinder along the longitudinal axis of such a coordinate system with a radius equal to or greater than the electron beam radius. The length of the cooling region should be maximised, as this corresponds to L_{cooler} in Eq. 13, and therefore has a direct impact on the cooling time. A reasonable minimum value should be of the order of $1\,\mathrm{m}$, which seems to be comparable to what was measured for the present e-cooler in [23]. If this requirement can only be obtained over a limited length, then one should expect an inversely proportional longer cooling time following Eq. 13.

Additionally, one should aim at improving the e-cooling performance by expanding the range of obtainable electron parameters. In particular:

- increasing the achievable electron current will normally lead to faster e-cooling, however, one should be careful of possible side effects linked to the electron space charge (see Eq. 17), increased electron temperature and/or decreased magnetisation (see Eq. 23). One should be able with the new electron gun to control the electron current independently from the electron energy. Ideally, one could also aim at controlling the transverse electron profile of the generated beam (e.g. Gaussian, flat, parabolic, hollow), as done in LEIR e-cooler. This, however, has to be considered a nice-to-have feature, but likely difficult to fully exploit in AD due to the low repetition rate and beam time allocated for machine development.
- increasing the achievable electron energy will allow cooling at higher momenta and therefore reduce the adiabatic blow up during the deceleration from $2\,\mathrm{GeV/c}$ that today is the largest compared to other ramps, see Fig. 1. Such an upgrade would also make the overall design more reliable and likely to meet the desired availability and reliability at lower energy.

The vertical installation of the e-cooler has also been a concern in the past due to the difficulty of access during required interventions. A possible improvement could come from installing the new e-cooler laying horizontally. Note however that in this case, the orbit bumps induced by the toroids would be vertical. For such a configuration, and assuming to maintain the same overall geometry of the section and shape of the e-cooler, then the orbit correctors next to the e-cooler would need to be rotated by 90 degrees. Additionally, one should note that in the whole section, there would be only one horizontal corrector per side of the e-cooler, which will not be sufficient for controlling the pbar-electron orbit overlap. To overcome this limitation, one could upgrade the far-end vertical corrector into a horizontal/vertical corrector. Such an upgrade should be considered even in the case of maintaining the vertical installation of the e-coolers, as this would allow for more comfortable pbar-electron orbit overlap.

The design of a new AD e-cooler started several years ago in line with the considerations above and trying to profit from the latest and more robust concepts in e-cooling devices. The latest status of such a design has been presented at the recent e-cooler review [3]. The main parameters of this design are shown in Table 3 together with the present e-cooler ones and with new specifications based on the observations made in this document.

Based on initial discussions at the start of the project, the design aims at reaching an equivalent pbar momentum of $500\,\mathrm{MeV/c}$. This value was chosen to better equalise the emittance blow-up between the $2\,\mathrm{GeV/c}$ and $100\,\mathrm{MeV/c}$ in two jumps of $\times 4$ and $\times 5$ instead of $\times 6.6$ and $\times 3$ as presently done, see Fig. 1. Table 4 summarises the energies under consideration and the related relativistic factors. This choice was also set as a way to drive the specifications of all components to cutting-edge technology [35]. However, reaching $500\,\mathrm{MeV/m}$ has to be seen as the ultimate goal, while the baseline target momentum is the present value of $300\,\mathrm{MeV/c}$, and the design should not compromise other important parameters such as HV stability, electron beam and magnetic field quality, corrector strengths, in general beams measurement and control capabilities, and the e-cooler operation reliability.

Provided the relations highlighted in the theoretical part of this document, one can also compute a few parameters for the different design and cooling momenta, see Table 5. To be noted that the values reported have to be taken for the sake of comparison, while the actual performance of cooling (cooling time, final emittances) is likely to be only quantifiable on the actual machine. One can observe that the most critical parameters are linked to the straightness of the magnetic field and the scaling with electron current. The option to reach ultimate pbar momentum of $500\,\mathrm{MeV/c}$ might result in considerably longer cooling times (from factor 2 to 5 longer compared to the present cooling at $300\,\mathrm{MeV/c}$), but this might get partially compensated by the expected smaller initial emittances following the scaling law with momentum, better magnetic field straightness, and the possibility of reaching ultimate current of $4.8\,\mathrm{A}$.

5 CONCLUSIONS

Functional specifications for the new AD e-cooler have been provided in Table 3, with expected performance summarised in Table 5. The option for the new e-cooler to reach an equivalent pbar momentum of $500\,\mathrm{MeV}$ has to be retained as the ultimate scenario, but this has a lower priority compared to other parameters acting to ensure reliable and comfortable operation of the new e-cooler. In this respect, the consolidation and possible upgrade of the orbit correctors in the cooling section should be envisaged, as well as improved beam instrumentation as the e-cooler BPMs and control and stability of the e-cooler voltages. Provided that orbit correctors will be upgraded as appropriate, the option of installing the e-cooler horizontally is deemed compatible with the operation of AD.

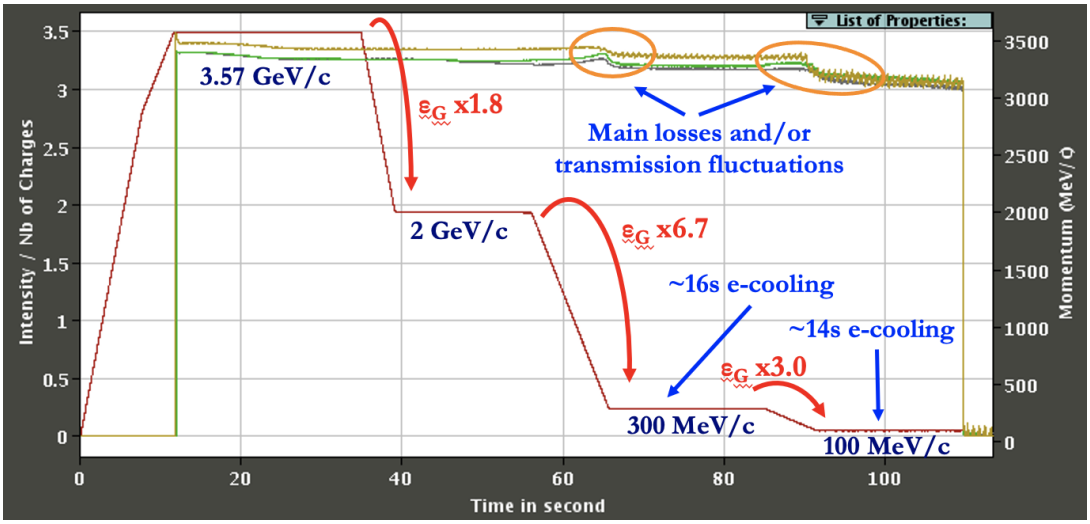

Figure 1: Typical AD cycle. The magnetic cycle is in red, while the other curves (in black, green and gold) show the estimated intensity (in units of 10^7 charges) along the cycle for three different shots.

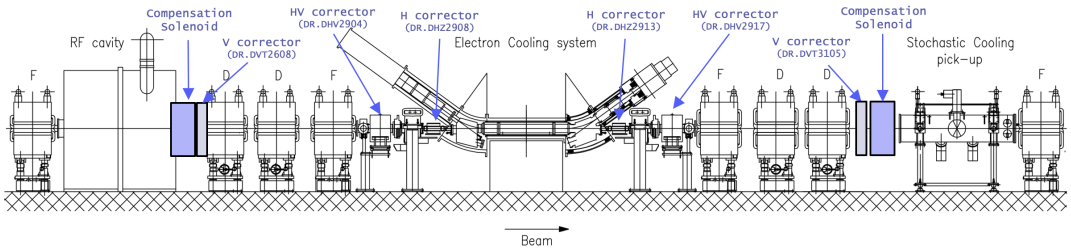

Figure 2: Present layout of the e-cooling section in AD.

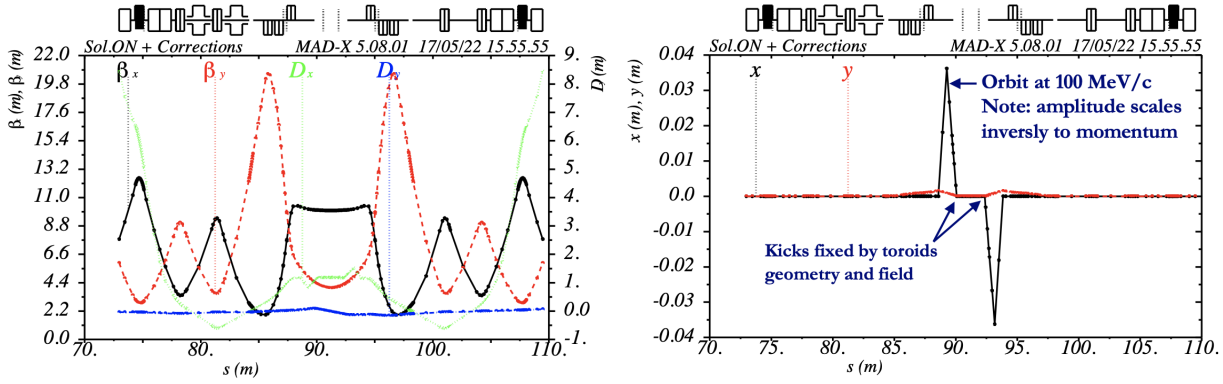

(a) **(b)**

Figure 3: Present AD optics along the e-cooling section (a) and closed orbit (b) taking into account coupling and compensation and toroid-induced kicks and their compensation.

.

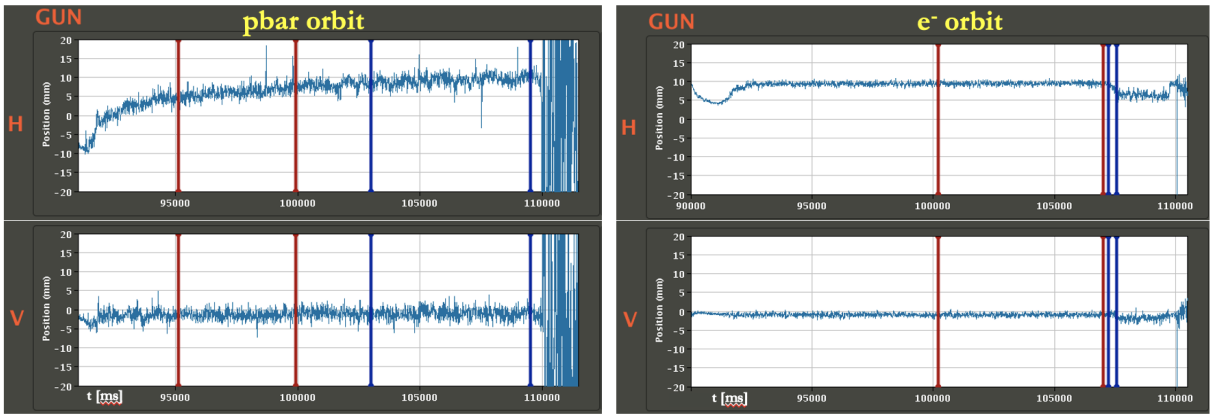

Figure 4: Measured orbit of pbar (left) and electron (right) beams along the $100\,\mathrm{MeV/c}$ plateau on the first pickup.

Table 3: Main parameters of the present e-cooler compared to the latest design values [36, 37] and general specifications from considerations in this document. Some of the main geometrical and layout parameters are assumed to remain unchanged.

	Present	Latest Design	This Spec.
AD ring length [m]	182.43	182.43	182.43
Drift magnet length [m]	~ 1.5	~ 1.5	~ 1.5
Drift magnet field [G]	600	600	$\sim 600^*$
Cooling region length [m]	~ 1	~ 0.8	≥ 1
Cooling region radius $\geq r_{\text{e-beam}}$ [mm]	25	25	≥ 25
Cooling region max$(B_\perp/B_\parallel)$	10^{-3}	5×10^{-4}	10^{-4}
Cooling region rms$(B_\perp/B_\parallel)$	n.a.	—	$< 10^{-4}$
Toroid field [G]	600	600	$\sim 600^*$
Toroid angle ϕ_0 [rad]	0.6283	0.6283	n.a.‡
Toroid radius r_{tor} [m]	1.133	1	n.a.‡
Toroid integrated transverse field [G·m]	~ 160	≈ 143	$\lesssim 160$
Gun magnetic field [G]	600	2400	n.a.‡
Gun perveance [µP]	0.58	2.6	n.a.‡†
Cathode radius [mm]	25	12.5	n.a.‡
Cooling region e^- beam $k_B T_\perp$ [meV]	100	25	$\lesssim 100$
Cooling region e^- beam $k_B T_\parallel$ [meV]	—	—	$\lesssim 1$
Cooling region e^- beam $r_{\text{e-beam}}$ [mm]	—	—	up to 25
e^- beam energy set resolution [eV]	1	—	0.1 (at 2.9 keV) 1 (at 25.5 keV)
e^- beam energy stability [eV]	—	—	< 0.1 (at 2.9 keV) < 1 (at 25.5 keV)
e^- beam intensity I_0 [A]	up to 2.4	up to 3.5	up to 2.4 (nominal) up to 4.8 (ultimate)
e^- beam intensity stability $[\Delta I/I_0]$	—	—	$\sim 10^{-4}$
e^- beam max relative losses $[\delta I/I_0]$	—	—	$< 10^{-4}$
e^- beam change of energy time [s]$^\diamond$	> 5	—	~ 1
e^- beam start/stop time [s]	—	—	$\ll 1$
BPMs e^-/pbar relative accuracy [µm]	—	—	$\lesssim 100$
Vacuum pressure in cooling region [mbar]$^+$	$\sim 10^{-10}$	$< 10^{-10}$	$< 10^{-10}$
E-cooler availability during physics	—	—	99%

* Ideally, one could allow for some margin (say 10%) for future studies and optimisations.

† Still, assuming to be able to increase by a factor 2 or more the electron current in a controlled way.

‡ This parameter depends on adopted technical choices such as to achieve other parameters.

+ H_2 equivalent pressure assuming vacuum levels of the order of 10^{-10} mbar in the neighbouring chambers, and 3.5A DC electron beam dumped on the bottom collector surface at 4 keV after conditioning. In case the neighbouring chambers will be NEG coated, one could aim for a factor of two better vacuum levels in the cooling region.

◇ This parameter can be read as the time to go from ~ 25.5 keV to ~ 2.9 keV within the energy set resolution along an operational AD cycle.

Table 4: E-cooling energies under consideration.

Ion p[MeV/c]	500†	300	100
Ion E_k[MeV]	124.9	46.8	5.3
e^- E_k[keV]	68.1	25.5	2.9
β	0.471	0.305	0.106
γ	1.133	1.050	1.006

† Considered as ultimate momentum for the new e-cooler.

Table 5: Pure calculation of a few relevant parameters for different design and cooling moments.

Parameter	Present		Latest Design			This Spec.			
Ion p[MeV/c]	300	100	500	300	100	500	300	300	100
I_e[A]	2.4	0.1	3.5‡	2.4‡	0.4‡	4.8+	4.8+	2.4	0.2+
Max $e^-\Delta E_k$[eV]	260	29	275	260	117	377	520	260	58
initial ϵ_x[µm]*	10	10	6◇	10	10	6◇	10	10	10
initial σ_p/p	1e-3	1e-3	1e-3	1e-3	1e-3	1e-3	1e-3	1e-3	1e-3
final ϵ_x[µm]	0.01	0.1	0.001	0.003	0.023	0.004	0.01	0.01	0.094
final σ_p/p	3e-6	1e-5	2e-6	3e-6	1e-5	2e-6	3e-6	3e-6	1e-5
Transverse τ[s]†	4.2	1.1	7.0	2.0	0.2	2.8	0.7	1.4	0.3
Longitudinal τ[s]	1.2	0.5	5.5	1.2	0.1	4.0	0.6	1.2	0.3

† Assuming magnetised cooling, i.e. considering only longitudinal electron temperature and magnetic field straightness.

‡ Values extrapolated from [17].

+ Assuming to be able to have a factor of 2 higher current than the present e-cooler, eventually up to ultimate current of 4.8 A.

* In [2] the initial 2-sigma emittance at $300\,\mathrm{MeV/c}$ was assumed to be $33\,\mu\mathrm{m}$, which corresponds to about $8.3\,\mu\mathrm{m}$ 1-sigma emittance, used in this report, and compatible with measurements on 15^{th} of June 2022. The value of $10\,\mu\mathrm{m}$ assumed here is meant to be a reasonable upper boundary.

◇ Assuming smaller initial emittance according to momentum scaling.

REFERENCES

[1] M. Lamont , *et al.* "AD e-cooler Consolidation strategy," 259th IEFC meeting, 2019.

[2] Baird, S. A., *et al.* "Design study of the antiproton decelerator: AD," CERN-PS-96-043-AR, Nov. 1996.

[3] Butin, F., *et al.* AD New Electron Cooler - Project Review Summary, Findings and Recommendations, CERN EDMS #2747809, July 2022.

[4] Poth H., Electron cooling: Theory, experiment, application, Physics Reports Vol. 196, Number 3, Pages 135-297, 1990.

[5] Tranquille G., Specification of a new electron cooler for the low energy ion accumulator ring, LEIR, International Workshop on Beam Cooling and Related Topics, 2004.

[6] Danared, H., Fast electron cooling with a magnetically expanded electron beam, NIMA, Vol. 335, no. 3, Nov. 1993.

[7] Meshkov I.N., Electron cooling — the first 30 years and thereafter, NIMA Vol. 391, Issue 1, Pages 1-11, 1997.

[8] Pikin, A., *et al.*, "Analysis of magnetically immersed electron guns with non-adiabatic fields", Review of Scientific Instruments 87, 113303, 2016.

[9] A.E. Borucka, *et al.*, Comparison of Available Models of Electron Cooling and Their Implementations, COOL2021, paper P1005, Novosibirsk, Russia, Nov. 2021.

[10] Bosser, J., *et al.*, Experimental Investigation of Electron Cooling and Stacking of Lead Ions in a Low Energy Accumulation Ring, CERN-PS-99-033-DI, May 1999.

[11] Parkhomchuk, V. V., Development of a New Generation of Coolers with a Hollow Electron Beam and Electrostatic Bending, COOL'05 Conference Proceedings, 2006.

[12] Parkhomchuk, V.V., New insights in the theory of electron cooling, NIMA, Vol. 441, 2000.

[13] I. Meshkov, *et al.*, Physics guide of BETACOOL code Version 1.1, 2006.

[14] Bosser, J., *et al.*, Neutralisation of the LEAR electron-cooling beam: experimental results, CERN-PS-95-17-AR, May. 1995.

[15] Bosser, J., *et al.* Neutralisation of the LEAR electron-cooling beam: experimental results, in Proceedings of Particle Accelerator Conference, pp. 2943-2945, Vol.5, 1995.

[16] Bosser, J., *et al.* Stability of cooled beams, NIMA Vol.441, Issue 1-2, Feb. 2000.

[17] Pikin, A., "Simulations of e-gun for AD e-cooler", joint BE-ABP / BE-BI meeting, `https://indico.cern.ch/event/774322/`, Jan 2019.

[18] Rossi, A. *et al.*, "Electron dynamics for high-intensity hollow electron beams," JINST, Vol. 16, number 03, 2021.

[19] Tanabe, T., *et al.*, Design of an electron cooling device for the accumulator cooler ring in MUSES project, NIMA, Vol. 441, no. 1, Feb. 2000.

[20] Brillouin, L., "A Theorem of Larmor and Its Importance for Electrons in Magnetic Fields," Phys. Rev., Vol. 67, issue 7-8, Apr 1945.

[21] Ferrario M., *et al.*, "Space Charge Effects," in CERN Yellow Report CERN-2014-009, pp.331-356, 2014.

[22] Derbenev, Yaroslav S and Skrinsky, A N, The Effect Of An Accompanying Magnetic Field On Electron Cooling, Part. Accel, Vol.8, pp 235-243, 1978.

[23] Wolf, A. *et al.*, "Magnetic field measurements in the electron cooling device for LEAR," CERN Report CERN-EP-INT-84-01, 1984.

[24] V. M. Panasyuk, *et al.*, Magnetic System of Electron Cooler for COSY, COOL2011, paper TUPS10, Alushta, Ukraine, Sep. 2011.

[25] A. Burov, *et al.*, Electron cooling for RHIC, NIMA, Vol. 441, no. 1, 2000.

[26] L. Zhao, L. *et al.*, "Magnet Design of the Electron Cooling System for HIAF," in IEEE Transactions on Applied Superconductivity, vol. 32, no. 6, pp. 1-5, Sept. 2022.

[27] Galnander, B. *et al.*, "Status of Design Work Towards an Electron Cooler for HESR," , COOL2007, paper THAP10, Bad Kreuznach, Germany, Sep. 2007.

[28] Melnikov, S.A. *et al.*, "Features of the Electron Cooling System of the NICA Booster," RuPAC21, paper TUPSB04, Alushta, Russia, Sep. 2021.

[29] Bocharov, V., *et al.*, Precise Measurements of a Magnetic Field at the Solenoids for Low Energy Coolers, COOL'05 Conference Proceedings, 2006.

[30] Poncet, A., Ion trapping and clearing, 5th Advanced Accelerator Physics Course, DOI 10.5170/CERN-1995-006.859, 1995.

[31] Calaga, R. and Tomás, R. and Franchi, A., Betatron coupling: Merging Hamiltonian and matrix approaches, PRSTAB, Vol.8, Issue 3, Mar. 2005.

[32] Eriksson, T., *et al.* AD and LEIR Consolidation, in Proceedings of LHC Performance Workshop, Chamonix, 2014.

[33] Korchevnyuk, V., PXMCXABCIP Magnetic characterisations, CERN EDMS #2519539, April 2022.

[34] Gamba, D. *et al.*, Official AD MAD-X optics model `https://gitlab.cern.ch/acc-models/acc-models-ad`, July 2022.

[35] Tranquille, J., *et al.* AD electron cooler gun and collector review `https://indico.cern.ch/event/1096814/`, Nov 2021.

[36] Tranquille, J., *et al.* New AD Electron Cooler Project Review `https://indico.cern.ch/event/1157504/`, May 2022.

[37] Von Freeden, L., Magnetic design of the new AD electron cooler (PXMLCEANWC), CERN EDMS #2731780, V.1, May 2022.

Simulation Code B

The simulation using the biot-savart equations, the different filters and other utilities used for testing and comparing signals can be found in the repository:

https://github.com/kapper24/magnetsim-main

acess will be granted upon request after a few working days